Dissertation

submitted to the

Combined Faculties of the Natural Sciences and Mathematics

of the Ruperto-Carola-University of Heidelberg. Germany

for the degree of

Doctor of Natural Sciences

Put forward by

Dipl. Phys. David Breyel

born in: Gifhorn

Oral examination: 17.12.2013

Statistical properties of interacting Rydberg gases

Referees: Prof. Dr. Andreas Komnik
Dr. Andrey Surzhykov

Kurzzusammenfassung: Gegenstand der vorliegenden Arbeit ist die Analyse der statistischen Eigenschaften von ultrakalten, wechselwirkenden Rydberggasen im Grundzustand, insbesondere im Hinblick auf den Phasenübergang zwischen ungeordneter und geordneter Phase – dem Rydbergkristall. Die typische Gitterkonstante des Rydbergkristalls ergibt sich hierbei aus der Dipolblockade, die die Anregung zweier Rydbergatome bis zu einem bestimmten Abstand unterdrückt. Zuerst wird der Vielteilchengrundzustand dieses auf ein Spin-$^1/_2$-Modell abgebildeten Systems mittels exakter Diagonalisierung eines effektiven Hamiltonoperators gefunden. Der anschließend berechnete mittlere Anteil der Rydbergatome sowie dessen Varianz weisen in Abhängigkeit der Systemparameter in den Regimen starker und schwacher Wechselwirkung das Verhalten von Potenzgesetzen auf. Ihr Schnittpunkt bestimmt den kritischen Wert der Wechselwirkungsstärke am Phasenübergang, welcher durch die zugehörige Korrelationsfunktion bestätigt wird. Mit analoger Methodik wird der Wert des kritischen Parameters im System wechselwirkender Exzitonenkodensate bestimmt, die dem Rydberggas in ihren Eigenschaften sehr ähnlich sind. Des Weiteren werden Techniken zur Korrektur der Effekte von Messeffizienz und Parameterfluktuationen in experimentellen Daten diskutiert, um den Vergleich von Theorie und Experiment zu ermöglichen. Im letzten Abschnitt werden neue Modelle für Rydberggase vorgestellt, die dynamische Effekte berücksichtigen oder die Anregung in verschiedene Rydbergzustände erlauben. Abschließend wird an einem rein statistischen Modell ein möglicher Nachweis für die Bildung von Rydbergclustern besprochen.

Abstract: The present thesis treats the interacting ultracold Rydberg gas with special emphasis on the statistical footprint of the phase transition between unordered and crystalline phase, which can be understood as a consequence of the dipole blockade effect. After mapping the system onto an effective spin-$^1/_2$-model, exact diagonalization of the effective Hamiltonian is used to obtain the many-body ground state. Repeated application of this procedure on random realizations reveals the underlying probability distribution of the number of Rydberg atoms, allowing to calculate its statistical moments. In the regimes of weak and strong interaction these observables have power law character. The critical interaction strength is estimated by extrapolating these power laws up to their intersection point. The same procedure is applied to interacting excitons in bilayer heterostructures uncovering a phase transition here as well. Furthermore, new methods are introduced to handle the effects of finite detection efficiency and parameter fluctuations to establish a better connection between experimental and theoretical results. Finally, new models are introduced to include dynamics or additional Rydberg states. The last model is of purely statistical nature and its results may be used as a tool for detecting a potential clustering of Rydberg atoms.

Contents

Chapter 1

Introduction

1.1. Preliminary remarks and historical context

In 2001 the Nobel Prize was awarded to E. Cornell, C. Wieman, and W. Ketterle (see Davis et al. [1995], Anderson et al. [1995] and Bradley et al. [1995]) for the experimental realization of a Bose-Einstein condensate (BEC), which originally was predicted by Einstein [1925] (see also Einstein [1924]) based on the work of Bose [1924]. This tremendous achievement marks the successful end of a long-lasting quest. Originating in the early days of quantum mechanics, the foundation of which was laid by the understanding of the photoelectric effect and the introduction of the famous constant h by Planck [1899], the field of quantum optics evolved continuously both theoretically and experimentally to make this accomplishment possible. Likewise, the realization of the BEC can be seen as the beginning of a new chapter in atomic and molecular physics as well as a key utility in other (new) areas of research, like e.g. quantum information theory with the quantum simulator as one of its a key ideas, introduced by Feynman [1982]. Based on this numerous proposals for the realization of a quantum computer (see Nielsen and Chuang [2000]) have been made, as e.g. done in the seminal work by Cirac and Zoller [1995], which are of particular interest since Shor [1999] presented his algorithm for the factorization of large numbers. But even today quantum computing has been demonstrated only with small numbers of Qubits (cf. Blatt and Wineland [2008]), illustrating the complexity of this subject. The rapid development of the field is driven by the ongoing effort spent in order to improve the control of quantum systems, for which the 2011 Nobel Prize was awarded to S. Haroche and D. Wineland.

Very interesting are also interacting quantum systems, such as the ultracold atomic gas which is treated in the present work. It turns out that it is possible to design the inter-atomic interactions in almost any desired way (see e.g. Büchler et al. [2007] who investigate polar molecules, or Fioretti et al. [1999] who treat both attractive and repulsive interactions). Bloch et al. [2008] state that the two main developments enlarging the range of physics associated with ultracold gases are the ability to tune interaction potentials via Feshbach resonances (see Courteille et al. [1998] and Inouye et al. [1998]) and the technique of generating deep optical lattices resulting in strong periodic potentials (see Greiner et al. [2002]). Besides these two possibilities, which in principle can be applied to any

gas of ultracold atoms, Rydberg atoms have the great advantage of a broad variety of interesting properties (see Gallagher [2005]) which can be used to alter their interaction potential. In particular the strong dependence of multiple properties on the principal quantum number of the electronic state makes this system attractive both experimentally and theoretically.

Recent experiments usually use two-photon excitation schemes to excite a mono-atomic gas which previously is trapped and laser-cooled. The advancement in cooling techniques allows to bring the ultracold cloud to a regime in which the atoms move only a few percent of the average inter-atomic distance during an experimental cycle. Certainly, the duration of a single experiment is limited by the life-time of the particular Rydberg state since a radiative decay may lead to an uncontrolled ionization avalanche. The typical life-times are of the order of several tenth of μs. Since the atoms barely move, an approximation called "frozen gas approximation" (see Anderson et al. [1998]), which is widely used in theoretical work, is justified. Within this approximation the remaining kinetic energy of the atoms is neglected assuming them to be fixed in space during the experimental procedure.

One particularly interesting feature of the Rydberg gas is the existence of the dipole blockade effect. Once an atom is brought to its Rydberg state, its induced dipole moment generates a strong field, which, in turn, shifts the energy levels of the adjacent atoms. If this field strong enough no other atoms can be excited to their Rydberg state any more in a certain area around the originally excited atom. Sometimes this feature is called "Rydberg bubble" and is best described by its lateral dimension – the blockade radius R_B. This effect has been confirmed for a single pair of atoms (see Gaëtan et al. [2009] and Urban et al. [2009]). It was suggested that this effect allows the Rydberg atoms to arrange themselves into regular structures – a Rydberg crystal. Due to its fragile nature such a crystal can hardly be evidenced by conventional spectroscopic methods as they are used in the realm of solid state physics. One way to circumvent these difficulties is to (destructively) measure the number of Rydberg atoms within the trapped cloud of atoms, recapture the atoms, and repeat the experiment to obtain the statistics of the system. The hope is that they reflect the phase transition from the disordered to the ordered Rydberg crystal phase.

The principal goal of the present thesis is the investigation of these statistical properties and their information content. First, we show a possible technique of how to estimate the critical parameters of the phase transition between the Rydberg crystal and the unordered phase. Next, we present methods to process experimental data to make them comparable to our theoretical predictions. Finally, alternative approaches are introduced to treat the system of the interacting Rydberg gas which possibly exhibit new physical effects that have not been discussed so far.

With this work we want to contribute to the understanding of strongly interacting many-particle systems. Further, we hope that our results can be used in the realm of quantum information devices based on Rydberg gases in the near future. This idea appears to be rather promising regarding the rapid advances in this area, which has its origin in the works of Jaksch et al. [2000] and Lukin et al. [2001].

1.2. Goals and open questions

As a guidance we want to list all major goals and open questions addressed in this thesis. They provide a basic structure which defines the outline of this work. Each major goal/question is divided

into several minor items:

- We want to obtain the statistics of an interacting Rydberg gas and investigate its properties. In particular we are interested in the features accompanying the phase transition, which all relate to the following questions:
  - Which observables can both be measured in experiment and calculated in theory?
  - How does the phase transition manifest itself in these observables?
  - Are we able to quantify the critical parameters of the phase transition in terms of the statistical properties of the Rydberg gas cloud?
  - The results have to be compared to other similar systems whose properties are well-known. We want to understand which features also appear in classical systems, which ones only in systems dominated by many-particle quantum effects. What methods and models are needed to compare those systems to the interacting Rydberg gas?
  - Are there any other systems sharing the same properties and phase transitions? Can the models and techniques used to treat the interacting Rydberg gas be adapted such that they are applicable in these systems?
- To be able to compare the results to experiment the data needs to be post-processed. The goal is to find tools making this comparison possible.
  - How do noise and finite detection efficiency affect measured values of important observables?
  - What are the error margins of the experimental results?
  - Is there a possibility to reduce the statistical error to obtain more significant results?
- Various techniques have been applied to the interacting Rydberg gas. We want to refine these methods or the underlying model to observe new features that were out of reach of existing calculations.
  - What are effects that cannot be treated within the existing model? Are there difficulties that have not been encountered so far?
  - Under which experimental conditions is a new approach necessary?

Whether these goals have been reached and the questions have been answered will be discussed in Chapter 7.

1.3. Organization of this work

Starting with this introduction, this thesis is divided into seven chapters. The second chapter still has introductory character as it presents the basic concepts of both experiment and theory of the gas of interacting Rydberg atoms. Important features like the blockade radius are discussed to connect some of the latest and most influential works and the present manuscript. At some points additional information is included which might not only facilitate the understanding of this work but could also help establishing a connection to neighboring areas of research.

In the third chapter the model of the system of interacting Rydberg atoms is introduced via its Hamiltonian. Subsequently the properties of this model, such as the cumulants in dependence on the model parameters and the correlation function, are analyzed by using an exact diagonalization technique on a truncated Hilbert space. The main results, which include the pair correlation function and a part of the phase diagram, are compared to other systems as well as the predictions of other works. The same technique as before then is applied in the fourth chapter to the system of interacting excitons in electronic bilayer systems, which share a lot of common properties with the aforementioned interacting Rydberg gases. Again basic statistical properties are obtained and compared to recent literature. All of the results presented in these two chapters are obtained in a purely numerical way.

The fifth chapter can be understood as independent on the preceding two chapters since it is devoted to presentation of the techniques developed for the analysis of experimental data. One focus of this chapter is the treatment of the finite detection efficiency and its effect on the cumulants of the underlying probability distribution. Furthermore, bootstrapping is introduced for error estimation, which is of particular interest for the treatment of unstable experimental conditions, the second main topic of this chapter. A new method is introduced to merge sets of data corresponding to equal (or very similar) experimental conditions to increase the amount of data available for statistical analysis.

The sixth chapter is devoted to introduce modifications of the model presented in the third chapter. In addition to the numerical procedure used in the previous chapters a mean field calculation is performed. The results of this chapter leave room for discussion and include no claim of completeness. The extension of one of the models discussed here can be understood as a possible outlook on further research directions.

Finally, the last chapter summarizes the most important results. In a compact form their interpretations and consequences are recapitulated. Further, possible continuations and extensions are listed as a forecast on future research.

Chapter 2

Background

We begin by introducing the basic concepts. These include the properties of single Rydberg atoms as well as their interaction. Furthermore, a typical experiment, as e.g. performed by van Bijnen et al. [2011] or Deiglmayr et al. [2006], is described. This leads us to the concept of the phase transition, which is discussed briefly as well. The results on the phase transitions of interacting Rydberg atoms and excitons in bilayer structures are presented in particular.

2.1. Rydberg atoms and their properties

In the comprehensive work by Gallagher [2005] Rydberg atoms are defined as atoms in which at least one of the electronic states has a high principal quantum number n. For our purposes "high" refers to states with $n \geq 10$ and we assume only a single electron of the respective atom to be excited. Alkali atoms, which are favored by experimentalists, are of special interest due to their single valence electron. The particular properties of these Rydberg atoms arise from the fact that the loosely bound electron results in a low ionization threshold and high sensitivity to external fields.

Even though this work mostly concentrates on the many-particle effects, some basic facts on single particles have to be described to motivate the models of our systems. The work of Weimer [2010] serves as a guide for the structure of the following. We start by stating that it is sufficient to consider Rydberg atoms as hydrogenic in the most cases. Certainly, this is one of the reasons why alkali atoms are preferred. The fact that the inner electrons do not completely shield the charge of the nucleus demands for a correction of the well-known formula

$$E_n = -\frac{mZ^2e^4}{2\hbar^2 n^2} \tag{2.1}$$

	δ_0	δ_2	δ_4	δ_6	δ_8
$ns_{1/2}$	3.13	0.20	-1.8		
$np_{1/2}$	2.65	0.39	-7.90	116.44	-405.90
$np_{3/2}$	2.64	0.33	-0.97	14.60	-44.73
$nd_{3/2,5/2}$	1.35	-0.60	-1.51	-2.42	19.736
$nf_{5/2,7/2}$	0.02	-0.06	-0.36	3.24	

Table 2.1: Quantum defects for Rubidium (as a representative for other alkali atoms). The values are rounded and errors are negligible. Since the quantum defect is only slightly n dependent the first two terms are sufficient for most applications at high n. Whenever no value is given, it is assumed to be negligibly small. Table taken from Lorenzen and Niemax [1983].

for the energies of the bound states of the hydrogen-like atom[1] (derived in any textbook on this topic, see e.g. Schwabl [2002]). This correction is done via the introduction of quantum defects $\delta_{n,l,j}$ which shift the principal quantum number as $n^* = n - \delta_{n,l,j}$ (for details see the textbook by Sakurai [2006]). The bound state energies are then given by

$$E_n = -\frac{Ry}{2n^{*2}} = -\frac{Ry}{2(n-\delta_{n,l,j})^2}, \tag{2.2}$$

where $Ry = 13.61\text{eV}$ is the Rydberg energy defined by the ionization energy of hydrogen. According to Gallagher [2005] these quantum defects are usually measured with high precision and are afterwards parametrized (as e.g. done by Lorenzen and Niemax [1983]) with the extended Rydberg-Ritz formula

$$\delta_{n,l,j} = \delta_0 + \frac{\delta_2}{(n-\delta_0)^2} + \frac{\delta_4}{(n-\delta_0)^4} + \frac{\delta_6}{(n-\delta_0)^6} + \frac{\delta_8}{(n-\delta_0)^8} + \cdots . \tag{2.3}$$

Table 2.1 shows the quantum defect of Rubidium as an example of the above.

The wave functions corresponding to these energies can be obtained similarly to the case of the hydrogen atom. This is done by introducing an effective potential that differs from the Coulomb potential at small distances, as it is shown by Gallagher [2005]. The wave functions, which then are finally found numerically from the differential equation of the preceding calculation by the Numerov method (see Blatt [1967]), are used to calculate the dependence of various properties of Rydberg atoms on the principal quantum number. In most cases it is sufficient to consider the semi-classical Bohr model to derive these dependencies, as it is argued e.g. by Amthor et al. [2009b]. In Table 2.2 some of the most important properties, namely binding energy, orbital radius, ionizing field, radiative life-time, and polarizability are given for two different Rydberg states. Also, the dependence of these properties on the principal quantum number is shown. Representatively for all the quantities shown in Table 2.2 we repeat the argumentation for the polarizability as it is presented by Amthor et al. [2009b]. The polarizability is given as the quotient of the squares of the dipole matrix elements to neighboring states over the respective energy difference. From Equation (2.1) we know that the energy levels scale as n^{-2} leading to a n^{-3} dependence for their

[1] From now on we will use atomic units, in which $m_e = 1$, $e = 1$, $\hbar = 1$ and $1/4\pi\epsilon_0 = 1$.

Quantity	n dependence	^{87}Rb @ 60D	^{87}Rb @ 43S
Binding energy	n^{-2}	3.96 meV	8.56 meV
Orbital radius	n^2	5156 a_0	2384.2 a_0
Ionizing field	n^{-4}	$\approx$ 44V/cm	
Radiative life-time	n^3	215 μs	90 μs
Polarizability	n^7	191 MHz/(V/cm)^2	8.06 MHz/(V/cm)^2

Table 2.2: Properties of Rydberg atoms in dependence on n together with values for ^{87}Rb. One has to replace the principal quantum number by n^* in the case of alkali atoms. Table taken from Amthor et al. [2009b] and extended by data (last column) from Heidemann [2008] (no value for ionizing field given).

differences. The dipole matrix elements scale as the orbital radius proportional to n^2. This results in a $(n^2)^2/n^{-3} \propto n^7$ dependence for the polarizability.

The system of a single atom interacting with (laser) light has been investigated in great detail. By now, a good overview over a large amount of quantities, which have been calculated using various techniques, is given in different textbooks, see e.g. Cohen-Tannoudji et al. [1992]. One of these quantities is the finite life-time of an atomic state. Its knowledge is important for any experimental realization to ensure that the Rydberg atoms do not decay to their ground states before the measurement. It is caused by two different effects. The first effect is black body induced transitions, which Gallagher [2005] shows to cause a life-time of

$$\tau^{\mathrm{bb}} = \frac{3n^{*2}}{4\alpha^3 kT}, \tag{2.4}$$

where $\alpha \approx 1/137$ is the fine structure constant, T is the temperature and k the Boltzmann constant. We notice that τ^{bb} has no dependence on the angular quantum number l and that $\tau^{\mathrm{bb}} \propto n^2$.

The other effect giving a finite life-time to a Rydberg atom is the spontaneous decay. The corresponding decay rate can be calculated in Wigner-Weisskopf approximation and is given by (see e.g. Scully and Zubairy [1997])

$$\gamma_{ab}^{\mathrm{sp}} = \frac{1}{4\pi\epsilon_0}\frac{4\omega^3\rho_{ab}^2}{3\hbar c^3}, \tag{2.5}$$

where a and b label the atomic states and ρ_{ab} the dipole matrix element between them. In their review article Delone and Goreslavsky [1994] (see also Delone and Krainov [2012]) give the dependence of the dipole matrix element to be

$$\rho_{ab} \propto (n_a n_b)^{-3/2}, \tag{2.6}$$

where the indices refer to the respective atomic level. Inserting this dependence into Equation (2.5) yields the result

$$\tau^{\mathrm{sp}} = 1/\gamma_{ab}^{\mathrm{sp}} \propto n^3. \tag{2.7}$$

The life-time due to both effects is now found to be

$$\frac{1}{\tau} = \frac{1}{\tau^{\mathrm{sp}}} + \frac{1}{\tau^{\mathrm{bb}}}. \tag{2.8}$$

Gallagher [2005] emphasizes that the different dependencies on the principal quantum number lead to a domination of the black body contribution for high n. Additionally, the black body decay rate dominates for large angular momentum states, which will be of minor importance for the work presented here.

2.1.1. Interactions between Rydberg atoms

The unique properties of Rydberg atoms lead to an interesting type of interaction between them. Great effort has been made by e.g. Singer et al. [2005b], Reinhard et al. [2007] and Marinescu [1997] to (perturbatively) describe the details of the interaction. Instead of reproducing their complex work we follow the lines of Amthor et al. [2009b] with their semi-classical approach, which is similarly presented by Comparat and Pillet [2010] in greater detail.

The interaction energy of two interacting classical dipoles is given by (see textbook on electrodynamics, e.g. Jackson [1975])

$$E = \frac{\boldsymbol{\mu}_1 \boldsymbol{\mu}_2}{r^3} - 3\frac{(\boldsymbol{\mu}_1 \mathbf{r})(\boldsymbol{\mu}_2 \mathbf{r})}{r^5}, \tag{2.9}$$

where r is the modulus of $\mathbf{r}$, which is the distance vector between the dipoles, and $\boldsymbol{\mu}_i$ are the dipole moments. It resembles the leading term of the large r expansion of the electrostatic interaction Hamiltonian of two atoms, as stated by Comparat and Pillet [2010]. Singer et al. [2005b] express the LeRoy radius R_{LR}, defined by LeRoy [1974], as $R_{\mathrm{LR}} = 2\left(\langle n_1 l_1 | r_e^2 | n_1 l_1 \rangle^{1/2} + \langle n_2 l_2 | r_e^2 | n_2 l_2 \rangle^{1/2}\right)$, where $\langle n_i l_i | r_e^2 | n_i l_i \rangle$ represents the expectation value of r_e^2 of the electronic wave functions for the respective atom. As long as the atoms are separated by more than R_{LR} the overlap of the atomic wave functions of the Rydberg atoms can be neglected, justifying the semi-classical approach of treating the Rydberg atoms as dipoles. Assuming that the distribution of the direction of the dipole moments in a large cloud of Rydberg atoms is uniform, the spatial alignment of the dipoles can be ignored. This makes the second term of Equation (2.9) vanish[2]. Now the classical dipole moment is replaced by its quantum mechanical counterpart, the dipole matrix element $\boldsymbol{\mu} = \langle \varphi_1 | e\mathbf{r}_e | \varphi_2 \rangle$ between the states $|\varphi_1\rangle$ and $|\varphi_2\rangle$. This is allowed for the cases treated here in which the atoms have a distance much larger than the typical distance of each atom's core to its respective electron. Otherwise the electrons would be indistinguishable. Now the interaction between two atoms in the states $|\varphi_1\rangle$ and $|\varphi_2\rangle$ can be calculated by taking the sum over all possible electronic states. As shown by Hernández and Robicheaux [2006] the interaction can therefore be expressed as

[2] In the case of higher angular momenta this approximation is not valid anymore. A more rigorous treatment is presented by Carroll et al. [2004].

$$V \propto \sum_{\langle\varphi_1'\varphi_2'|} \langle\varphi_1'\varphi_2'|\frac{\boldsymbol{\mu}_1\boldsymbol{\mu}_2}{r^3}|\varphi_1\varphi_2\rangle. \tag{2.10}$$

Since the dipole matrix elements are largest for states energetically close to the original states, the system is now reduced to the situation of three-level atoms. A sketch of this is shown in Figure 2.1. While the Rydberg states have large energy differences, a pair of states in the coupled system is almost degenerate. Of the already reduced system only the subspace of these almost degenerate states will be considered. Denoting the dipole matrix element of the transition $|p\rangle \to |s\rangle$ by μ_1 and of the transition of $|p\rangle \to |s'\rangle$ by μ_2, the Hamiltonian of the subsystem is given by

$$\mathcal{H}_{\text{sub}} = \begin{pmatrix} 0 & \frac{\mu_1\mu_2}{r^3} \\ \frac{\mu_1\mu_2}{r^3} & \delta \end{pmatrix}, \tag{2.11}$$

where $\delta = (E_p + E_p) - (E_s + E_{s'})$ is the energy difference between the basis states. The eigenenergies are obtained by simple diagnonalization of this Hamiltonian and are given by

$$E_\pm = \frac{\delta}{2} \pm \sqrt{\left(\frac{\delta}{2}\right)^2 + \left(\frac{\mu_1\mu_2}{r^3}\right)^2}. \tag{2.12}$$

These eigenenergies can be understood as the interaction potential between Rydberg atoms. The dominant character of the interaction in two regimes can now be found by Taylor-expanding the expression (2.12). Less important to this work is the case of vanishing δ. It can be reached by application of an electric field, which Stark-detunes the atomic states for any r or can be understood as the small r behavior in the field free case. Equation (2.12) then reduces to

$$E_\pm \approx \pm\frac{\mu_1\mu_2}{r^3} = \pm\frac{C_3}{r^3}. \tag{2.13}$$

We introduced $C_3 = \mu_1\mu_2$ as the coefficient of this dipole-dipole interaction. In literature this type of interaction is also called a Förster resonance (introduced by Förster [1948] for radiationless energy transport in biological systems).

The second case is the regime where $\frac{\mu_1\mu_2}{r^3} \ll \delta$. Here one finds

$$\Delta E_{|pp\rangle} = -\frac{(\boldsymbol{\mu}_1\boldsymbol{\mu}_2)^2/\delta}{r^6} = -\frac{C_6}{r^6} \tag{2.14}$$

for the energy shift of the $|pp\rangle$ level. This corresponds to the well-known van der Waals interaction (see e.g. Johnson et al. [2008]). From Section 2.1 the dependencies of the dipole matrix element and the energy difference of neighboring levels on the principal quantum number are known. They are given by

$$\mu \propto n^2 \qquad \text{and} \qquad \delta \propto n^{-3}. \tag{2.15}$$

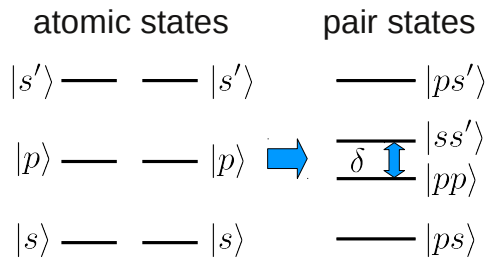

Figure 2.1: Interaction of Rydberg atoms. On the left the levels of two separate Rydberg atoms are shown, while on the right the pair states of the system are shown. For the interaction between the Rydberg atoms only the subsystem of $|ss'\rangle$ and $|pp\rangle$ is considered. The prime indicates that the corresponding angular momentum state belongs to a different principal quantum number. The figure is adapted from Amthor et al. [2009b].

With this the interaction coefficient can be written as

$$C_6 = \frac{(\boldsymbol{\mu}_1 \boldsymbol{\mu}_2)^2}{\delta} \propto n^{11}. \tag{2.16}$$

Since this is the only case treated throughout this work we can safely omit the index on the C_6 coefficient and label it by C from now on. Whenever a different type of interaction is utilized it will be noted explicitly. In Equation (2.16) one can see that by addressing different Rydberg states the interaction strength can be changed by orders of magnitude. This, besides the fact of the long-ranged potential, makes the system of interacting Rydberg atoms particularly interesting.

The crossover radius R_c, at which the character of the interaction changes from dipole-dipole to van der Waals interaction, is in the range from $\approx 3\mu$m up to $\approx 10\mu$m in experiments. It is defined by Saffman et al. [2010] via the equation $\delta = C_3/R_c^3$, where again δ is the energy defect between the neighboring levels of the coupled system of two atoms. A typical plot of the interaction energy in dependence on inter-particle distance is also shown there.

In experiments the strong dependence of the interaction coefficient on the principal quantum number allows a wide range of interaction strength to be addressed. Typical values are given by Amthor et al. [2007] who find $C \approx -7.0 \cdot 10^{18}$au, $C \approx -1.0 \cdot 10^{21}$au and $C \approx -3.9 \cdot 10^{2}$au for the cases $n = 40$, $n = 60$, and $n = 82$, respectively.

2.1.2. Rydberg blockade

Among other properties, the blockade radius R_B makes the system of interacting Rydberg atoms interesting in particular. It is defined as the distance around a Rydberg atom within no further excitation is possible. The reason for the existence of such a radius can be understood in two different pictures: in the model used later in this thesis, in which each atom is modeled as a two-level subsystem, the increase of potential energy for two Rydberg atoms close to each other exceeds the energy "loss" for each atom being in the Rydberg state individually. Therefore, it is energetically not favorable to excite Rydberg atoms within a certain distance, which then is called blockade radius.

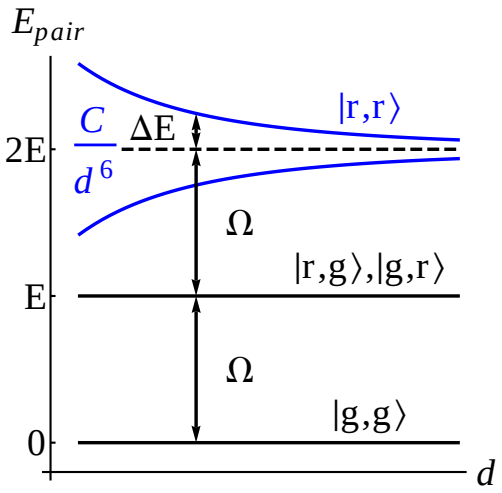

Figure 2.2: Energy level scheme of a system consisting of two two-level atoms which interact via van der Waals interaction in their Rydberg state. The distance between atoms is labeled by d to avoid confusion with the Rydberg state $|r\rangle$. The excitation of the double Rydberg state $|r, r\rangle$ is strongly suppressed due to the large detuning ΔE. The figure is adapted from Gaëtan et al. [2009].

In the other point of view a Rydberg excitation leads to a shift of the Rydberg energy level for all surrounding atoms depending on their distance to the Rydberg excitation. This shift causes the excitation laser to be highly non-resonant with the transition frequency for all surrounding atoms, making the excitation probability very small.

The effect explained above is illustrated in Figure 2.2 for the situation of a pair of atoms. The system can either have one, two, or no excitations, whereas the case of two excitations is suppressed at small distances. In the limit of large distances the laser becomes resonant with transition frequency so that the doubly excited state is accessible.

The blockade phenomenon has been investigated in great detail. While e.g. Gaëtan et al. [2009] and Urban et al. [2009] trap two atoms individually in the distance of a few micrometers, other approaches observe the blockade effect in a cloud of ultracold atoms, e.g. done by Heidemann et al. [2007] and Schempp et al. [2010]. In the latter experiment the blockade is evidenced via a saturation of the Rydberg signal in the limit of large densities for high Rydberg states, which cannot be observed in the case of low Rydberg states.

If the blockade radius is large, meaning that there is a large number of other atoms within this radius, the concept of the "superatom" often is used. A superatom is considered to be a group of atoms sharing a single excitation. For such a superatom the collective Rabi frequency has to be introduced. This can most easily be done in the extreme case where the full experimental volume is blocked by a single excitation and thus all atoms are collected to a single superatom. Here, both theory and experiment agree, as for example shown by Dudin et al. [2012], that the Rabi frequency corresponding to the shared excitation is given by $\sqrt{N}\Omega$, where Ω is the single particle Rabi frequency and N is the number of atoms within the blockaded volume.

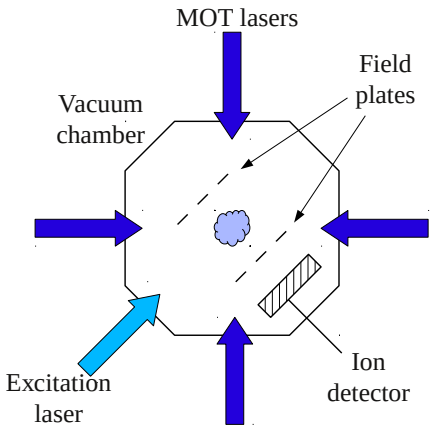

Figure 2.3: Schematic experimental setup of a typical experiment. The cloud of Rydberg atoms (light blue) is trapped and cooled by the MOT lasers (dark blue) and subsequently excited by the excitation laser (bright blue). The Rydberg atoms are ionized via the field plates and detected with a MCP. Further details are given in the text. The figure is adapted from Amthor et al. [2009b].

2.2. Experimental setup

Throughout this work we always have the same experimental setup in mind when talking about Rydberg atoms. A sketch of the setup is given by Amthor et al. [2009b]. Real experiments, as performed by van Bijnen et al. [2011], Deiglmayr et al. [2006] and Singer et al. [2005a], rely on the same principle but are technically more sophisticated. Here we restrict ourselves to the underlying principles and leave out details that may be found in any of the three publications mentioned above.

2.2.1. Experiments to obtain the probability distribution

The typical setup for an experiment concerning the statistics of interacting Rydberg atoms is shown in Figure 2.3. Once the vacuum chamber is evacuated, atoms can be inserted via a dispenser (not shown). Typically Rubidium atoms are used, but other choices are possible, as e.g. done by Robinson et al. [2000] who also use Cesium atoms. These atoms are trapped and cooled via a magneto-optical trap (MOT), the functionality of which is well-known and explained in various textbooks (see e.g. Demtröder [2005]). To justify the "frozen gas approximation", which is used later, the atoms have to be cooled further by more elaborate methods, as e.g. the Sisyphus cooling (see e.g. Metcalf and Van Der Straten [1999]; also not shown in Figure 2.3). When the atoms are cooled to the desired temperature the (pulsed) excitation laser is switched on. The Rydberg atoms in the resulting state then are ionized by ramping up the voltage of the field plates. The ions are accelerated by the electric field and counted once they hit the detector. The result of the measurement therefore is the number of Rydberg atoms present in the particular run of the experiment. This experiment is repeated numerous times to obtain a sample of the underlying

probability distribution.

The Rydberg atoms are ionized using state-selective field ionization. This is done by a linear electrical field ramp as done by Walz-Flannigan et al. [2004], who reach a maximal value of $\approx$ 220V/cm. This field then accelerates the ions towards the detector, which typically is a micro channel plate (MCP). Its functionality is explained in great detail by Wiza [1979]. As in every experiment, the measured results are subject of a finite detection efficiency η. In this case, the finite detection efficiency is generated by a finite dead time of the MCP. During the dead time more than one particle can hit the detector, leading to a single count only. Also, ions may be absorbed by the field plates or ions simply do not hit the MCP within the measuring time interval. Additional factors, as e.g. caused by post processing of the measured signal, will be addressed later in this work. Typical values of the detection efficiency are given by Wiza [1979] and Cubel Liebisch et al. [2005] and are within a range of $\eta \approx 0.5 - 0.85$.

Typical densities of the atomic cloud are in the range from 10^9cm^{-3} (Li et al. [2005]) to 10^{11}cm^{-3} (Tong et al. [2004]). It is possible to superpose the lasers in such a way that the resulting volume available for excitation becomes quasi one- or two-dimensional, as e.g. done by Dudin and Kuzmich [2012]. In this case "quasi" refers to the situation in which one or two spatial dimensions of the excitation volume are comparable or even slightly smaller than the blockade radius of a Rydberg atom. Therefore, the excitation of only one single Rydberg atom is possible in the respective direction.

The temperature of the gas cloud is of the order of 300μK or even lower. The atoms move approximately 0.3μm, which is roughly 3% of the inter-atomic spacing in a cloud of density 10^9cm^{-3}, during the experimental relevant time of 1μs (see e.g. Li et al. [2005]). Similar experimental conditions are reported in Anderson et al. [1998], and Mourachko et al. [1998]. This leads to the "frozen gas approximation", which treats the atoms as fixed in space during the experimental cycle. It is the foundation of numerous works done in the field of Rydberg physics (see e.g. Frasier et al. [1999], Mourachko et al. [2004]).

Boisseau et al. [2002] note that if the distance between Rydberg atoms is larger than R_{LR}, defined in the previous section, there is only very little overlap of the electronic clouds. This leads to a small the auto-ionization probability and thus the Rydberg atoms interact via their electric dipoles. The auto-ionization process of ultracold Rydberg atoms was thoroughly analyzed by Robinson et al. [2000] yielding typical time scales of the order of μs. The ionization probability within 30μs is found to be of the order of 10^{-10} by Amthor et al. [2009a], which is not observable experimentally. This information allows to perform the experimental cycle without having to take into account the probability of an uncontrolled ionization within the measurement.

Usually the excitation process is done by a two-photon excitation. There are three main reasons why the two-photon excitation is preferred over a single-photon excitation. First, the transition energy between ground and Rydberg state is of the order of several eV. For a long time lasers with these frequencies were not available at all and even today they are far more expensive than a set of two lasers operating within the visible part of the spectrum. The second reason for two-photon excitation is the possibility of addressing S ($l = 0$) angular momentum states, which are of particular interest since the electronic wave function is spherically symmetric and therefore no angular dependence of the interaction potential has to be taken into account. For a single-photon excitation the dipole transition from a $l = 0$ ground state to a $l = 0$ excited state is forbidden by selection rules. The third reason to prefer a two-photon excitation will be discussed in more detail in the next section. The two transitions allow to use one of the lasers as a pumping laser while the

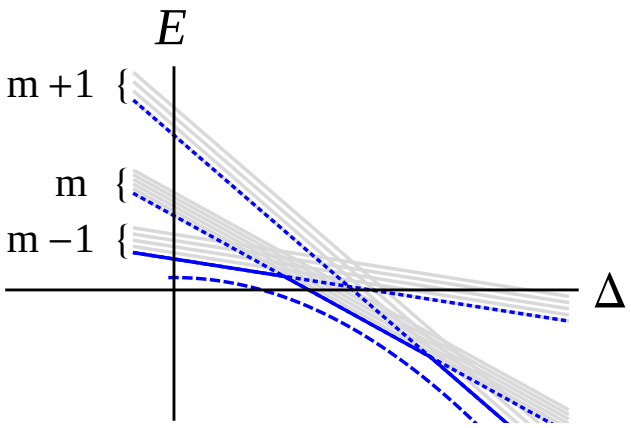

Figure 2.4: Adiabatic formation of the ground state. The diagram shows the (schematic) energy (in arbitrary units) of a fixed realization of atoms. The gray lines correspond to the energies of specific states in which a certain number of atoms is excited. The slope of each gray line is determined by the number of excitations, and the different lines within each bunch represent the different configurations of excitations. The configuration of lowest energy in each bunch is marked by a dotted blue line and the over all lowest energy by a solid blue line. The ground state, which is a superposition of the above mentioned states, is always lower in energy than these states and represented by a dashed blue line. Increasing the detuning Δ adiabatically ensures that one remains in the ground state for finite Δ. The figure is inspired by Figure 2 in the work by van Bijnen et al. [2011].

other one is used as a probe. In this fashion electromagnetically induced transparency can be used to observe spatial correlations in the cloud of ultracold atoms.

For Rubidium the two-photon excitation typically is performed via the transitions $5S_{1/2} \rightarrow 5P_{3/2}$ and $5P_{3/2} \rightarrow nl$, as e.g. done by Amthor et al. [2007]. For the respective excitation two laser systems at 780nm and ≈480nm[3] are used. For pulsed excitation the pulse duration is of the order of 100ns as given by Cubel Liebisch et al. [2005]. Both lasers can be detuned from the transition frequency between the respective atomic states. By applying a large detuning to the lower transition, the effect of the intermediate level becomes negligible resulting in an effective two-level description of the system. Once the atom can be treated as a two-level system, it is possible to detune the second laser to be not in resonance with the desired Rydberg level. This detuning is an important parameter of the model we will use throughout this work. The excitation process will be discussed in more detail in Section 2.2.3.

Later in this work we are interested in ground state properties of the system. Therefore, we have to ensure that the many-particle ground state of the full system is accessible in experiment. It may be realized by the use of chirped laser pulses which mimic an adiabatic switching of the detuning Δ. The graph shown in Figure 2.4 explains how the ground state can be reached for any reasonable set of parameters, as done by van Bijnen et al. [2011]. It can be understood in the following way: at the beginning the laser frequency of the excitation laser is in resonance with the transition frequency from ground to the desired Rydberg state. This corresponds to $\Delta = 0$. Here the system is in its ground state and now Δ is increased (adiabatically) slowly. As shown in Figure 2.4 the ground state (dashed blue line) is always below the energetically lowest "configuration state", which results

[3]The wavelength of the second excitation laser is only given approximately to indicate that this laser has to be detuned to address different Rydberg states.

from the ground state being a linear combination of the "configuration states". While increasing Δ the configuration being closest to the ground state changes because there is a different number of excitations in each group of states. Therefore, we expect the linear combination which represents the ground state to vary in such a way that the coefficients of the lowest lying states increase. That means that there is a higher probability to measure a larger number of excitations for a larger detuning.

We briefly summarize this section by itemizing all experimentally relevant parameters which will be used to motivate the theoretical model utilized in this work. Under the assumption of the frozen gas approximation the relevant parameters are the density of ground state atoms n, the detuning Δ of the excitation laser from the transition frequency, the intensity of the laser that is closely related to the Rabi frequency Ω of the transition and the interaction strength C introduced in Section 2.1.1. A set of these parameters uniquely defines the properties of this system so that the same result may be reproduced any time under the same conditions.

2.2.2. Experiments with spatial resolution

For this work the spatial distribution of Rydberg atoms in a cold atomic cloud is a particular point of interest. Different proposals of how to image it have been introduced in experiment, as e.g. done by van Bijnen et al. [2011], who use a particle accelerator, or Gericke et al. [2008], Weitenberg et al. [2011], and Bakr et al. [2009] whose methods apply to the case of a cold atomic gas in an optical lattice. It is possible to use field ion microscopy, too, as done by Schwarzkopf et al. [2011], or high-resolution fluorescence imaging, as done by Schausz et al. [2012], to obtain spatially resolved observables such as the correlation function, which will be addressed in this work as well. Müller et al. [2009] suggest to use a single Rydberg atom as a control quantity over an ensemble of atoms which can be used for detection as explained by Olmos et al. [2011]. This work is already closely related to the approach brought forward by Ates et al. [2011], Petrosyan and Fleischhauer [2012], and Günter et al. [2012], who all propose to use electromagnetically induced transparency (EIT) as a tool to depict the atomic gas cloud. The latter work will serve us as a guide in this section as far as the application to Rydberg atoms is concerned.

The concept of EIT is well-known and covered in most textbooks on quantum optics (see e.g. Walls and Milburn [2008] or Scully and Zubairy [1997]). For imaging of a cloud of interacting Rydberg atoms the optical susceptibility is calculated. This is e.g. done by Sevinçli et al. [2011] up to third order. For the purposes of EIT measurements the atom is treated as a three-level system (most commonly in the Λ-configuration, but also applicable to the cascade configuration in the situation of the Rydberg atoms). One is interested in the absorption of a probe laser which couples two of the states while a second transition in the system is driven with a pump laser. The equations of motion for the density matrix elements of this system, the Bloch equations, may be written down and solved for the component corresponding to the probe transition. One arrives at the expression (see Günter et al. [2012])

$$\chi = \frac{i\Gamma_p}{(\Gamma_p - 2i\Delta_p) + \Omega_c^2(\Gamma_c - 2i\Delta)^{-1}} \tag{2.17}$$

for the susceptibility in the limit $\Omega_p \ll \Omega_c, \Gamma_p$. Here, Ω_p and Ω_c are the Rabi frequencies of probe and pump laser, respectively, and Γ_p and Γ_c are the spontaneous decay rates of the intermediate

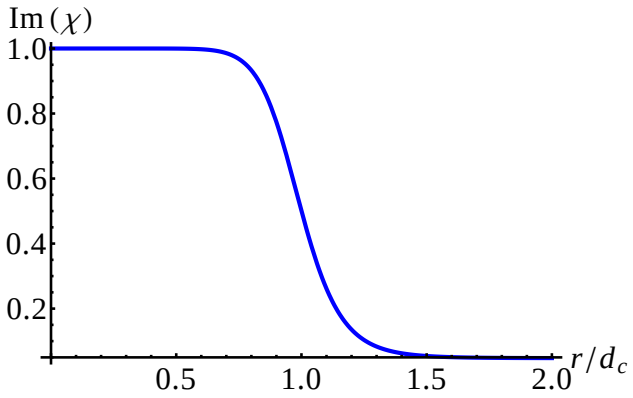

Figure 2.5: Imaginary part of χ in dependence on distance. EIT causes the atoms close to a Rydberg atom to absorb light while atoms far away from Rydberg atoms appear to be transparent. That means that Rydberg atoms manifest themselves as dark spots in an otherwise bright absorption image. The parameters are $\Omega_c = 1$, $\Gamma_c = 1$, $\Delta_p = 0$ and $\Delta_c = 0$ (measured in units of Γ_p). The figure is adapted from Günter et al. [2012].

and the Rydberg atomic level. In the experimental realization the intermediate level usually is the level used for the first transition of the two-photon excitation process introduced in Section 2.2.1. Δ_p is the detuning of the pump laser with respect to the atomic transition frequency and Δ_c the detuning of the probe laser. The interaction of the Rydberg atoms is included via the introduction of $\Delta = \Delta_c + \Delta_p + C/r^6$, where r is the distance between the interacting Rydberg atoms. This equation states that the detuning of the probe laser depends on the distance to any other Rydberg atom. Therefore the probe absorption, which is proportional to the imaginary part of the susceptibility, depends on r as well. This dependence is shown in Figure 2.5. The distance r is measured in units of $d_c = (2C\Gamma_p/\Omega_c^2)^{1/6}$, defining the point at which the imaginary part of χ reduces to half of its original value. One can see that the absorption is high in the vicinity of a Rydberg atom and low for large distances. That means that the absorption image of a two-dimensional cloud of atoms would be dark at the places where Rydberg atoms were placed since the atoms surrounding the Rydberg atom would absorb the light. In contrast, those atoms far from any Rydberg atom would appear transparent to the laser,leading to bright spots in the absorption image. In this way the spatial correlations of the Rydberg atoms in the gas cloud can be measured.

Besides the correlations of the atoms it is also possible to measure the correlation between the photons propagating through the cloud of atoms (see e.g. Gorshkov et al. [2011]). In this case one considers the collective state of atom and photon: the polariton. Hofmann et al. [2013b] show in detail that the blockade of the Rydberg atoms lead both to different statistics for Rydberg atoms as well as for photons. As stated by Peyronel et al. [2012] the blockade of Rydberg atoms leads to a blockade of photons in the sense that it is not permissible to transmit two photons simultaneously. The photon correlations also are discussed by Dudin and Kuzmich [2012], where the blockade effect serves the concept of creating a single photon source.

2.2.3. Excitation process and mapping to spin system

In the following we will treat the system of interacting Rydberg atoms as an ensemble of spin-$^1/_2$-particles, as e.g. done by Robicheaux and Hernández [2005]. The following assumption – made in

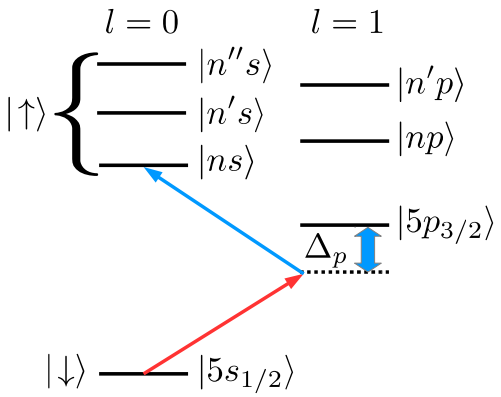

Figure 2.6: Energy level scheme for Rb atoms. The lasers are far detuned from the intermediate level, it therefore can be eliminated adiabatically. The curly bracket indicates that whichever state the laser is tuned to will be labeled by $|\uparrow\rangle$. The figure is adapted from Weimer [2010].

most works on the topic, see e.g. Weimer [2010] – justifies the mapping. Here it is stated that the intermediate atomic level, which is of great importance for EIT experiments as explained in Section 2.2.2, can be adiabatically eliminated by detuning the excitation laser far from this level. Of the remaining levels of the atom only two levels, the ground state and one particular Rydberg state, are of interest. The Rydberg states are separated from each other by energies much larger than the detuning, which allows to neglect all but the one Rydberg state one is interested in. The resulting two-level system can be mapped onto the desired spin-1/2 system by $|g\rangle \to |\downarrow\rangle$ and $|e\rangle \to |\uparrow\rangle$. A sketch of this is shown in Figure 2.6.

As already mentioned before, the two-photon excitation scheme allows for addressing the $l = 0$ angular momentum states. It would be also possible to address $l = 2$ states (which are not shown in Figure 2.6) for which an angular dependence of the interaction would have to be included. Throughout this work we will assume the latter not being the case and the interaction therefore only is distance dependent.

2.3. Phase transitions

Phase transitions, present in almost any sub-discipline of physics, are one of the key concepts of modern physics. The properties of macroscopic many-particle systems are described by using only few thermodynamic observables which depend on a set of parameters defining the system's phase. The properties of the same system may strongly vary in different phases, resulting in very different values of the observables. Therefore, parameter regimes can be found in which the properties of the system remain the same, defining the term phases. A great advantage in the investigation of a phase transition in a particular system is the universality, which allows to predict the systems behavior based on the knowledge of a system of the same universality class. No complete overview over the subject of the phase transition can be given at this point due to the large extent of work done in this field. The most important features will be covered in the following sections, where we will mostly follow the comprehensive work done by Vojta [2003] (cf. Vojta [2000]).

2.3.1. The concept of the phase transition

In modern physics one distinguishes between first order, where two phases can co-exist because latent heat is involved, and continuous phase transitions, where no co-existence is possible. This classification, as e.g. shown by Goldenfeld [1992], defines

- a first order transition as phase transition at which $\partial F/\partial K_i$ is discontinuous. Here F is the free energy and K_i are generalized couplings.
- a continuous phase transition as a phase transition at which all $\partial F/\partial K_i$ are continuous. Higher order derivatives may but do not have to be discontinuous. Sometimes these phase transitions are called n-th order phase transition, where n is the lowest order in which a discontinuity appears.

Both types of phase transition can appear as a classical phase transition as well as a quantum phase transition. Whereas the former relies on thermal fluctuations, the latter can be observed at $T = 0$ where no thermal fluctuations are present. In the case of the classical system the free energy $F = E - TS$ has to be considered. In equilibrium the system is assumed to be in a minimum of the free energy. Increasing the degree of order of a system (in most cases) results in a smaller internal energy E, as for example in the Ising system where a ferromagnetic coupling benefits the parallel alignment of spins. The entropy S in contrast is increased for a higher degree of order in the system. That means that a phase transition from an ordered phase occurs once the temperature T is large enough to allow the thermal fluctuations to overcome the energy costs of destroying the order. Of course, the reverse process also is possible in which the thermal fluctuations do not suffice to remain in the unordered phase and therefore an ordered phase is formed.

Besides the discontinuities in the higher order derivatives continuous phase transitions can be described using the concept of the order parameter. This order parameter is a physical quantity that is finite in the ordered phase and zero on average in the unordered one (e.g. the magnetization in the case of the ferromagnet-paramagnet transition). Additionally, one defines the correlation length ξ, which is a measure of how much two particles separated by a certain distance "feel" each other. It is introduced via the correlation function, as e.g. done by Nolting [2005],

$$g(i,j) = \langle n_i n_j \rangle - \langle n_i \rangle \langle n_j \rangle, \tag{2.18}$$

where the n_i are the density operators corresponding to the "objects" whose correlation one is interested in, e.g. the spins in an Ising system. In Ornstein-Zernike theory (see Ornstein and Zernike [1914]) it is found that in the critical region the correlation function behaves as

$$g(\mathbf{r},\mathbf{r})' \propto \frac{e^{-|\mathbf{r}-\mathbf{r}'|/\xi}}{|\mathbf{r}-\mathbf{r}'|^{d-2+\eta}}. \tag{2.19}$$

Here, d is the dimension and η a system specific constant. From this point on Vojta [2003] reasons that close to the critical point the spatial correlations of the order parameter fluctuations become long-ranged, meaning that the correlation length diverges. One finds that

$$\xi \propto |t|^{-\nu}, \tag{2.20}$$

where ν is a critical exponent and $t = |T - T_c|/T_c$ in the case of a finite transition temperature and a different dimensionless quantity otherwise. Also, the time scale for correlations diverges algebraically according to

$$\tau_c \propto \xi^z = |t|^{-\nu z}, \tag{2.21}$$

where τ_c is the correlation time scale and z is the dynamic critical exponent. This leads to the well-known critical phenomena. They emerge from the fact that at the critical point correlation length ξ and correlation time scale τ_c are infinite. Already Widom [1965] recognized that this causes fluctuations on any time and length scale, making the system scale invariant. Mathematically the scale invariance of a function $f(x)$ leads to the equation

$$f(\alpha x) = c(\alpha) f(x). \tag{2.22}$$

In the case of a physical system this formula can be derived from first principles by renormalization group techniques (see Wilson [1971a] and Wilson [1971b]), which emerged from the work done by Kadanoff [1966]. As done by Weimer [2010], the left hand side of Equation (2.22) can be expanded in a Taylor series around $\alpha = 1$, yielding the result that the functions c and f have to be of the form

$$c(\alpha) = \alpha^{\kappa} \qquad \text{and} \qquad f \propto x^{\kappa}, \tag{2.23}$$

where κ is a real number. Equation (2.23) states that any observables will show a power law behavior in the vicinity of the critical point. These are the above-mentioned critical phenomena. The exponents of these power laws are referred to as critical exponents. Their values may be calculated within different theories for various systems. A broad variety of them is given in most textbooks (see e.g. Fließbach [2010]).

The concept of the critical exponents directly leads to the notion of universality classes of phase transitions. These universality classes are defined as groups of systems which have the same critical exponents. The fact that they are not just the collection of systems having the same critical exponents by coincidence can be deduced from the above in the following way: once a system is close to the critical point the correlation length diverges and the fluctuations take place on any length scale. Therefore, the microscopic structure of the system becomes unimportant. Fisher [1998] states that one of the early successes of renormalization group theory was to realize that the universality class of a system solely depends on "the vectorial or tensorial character of the relevant order parameter". In other words this means that the universality class of a system is determined by its dimension and the symmetry of the order parameter, as stated by Vojta [2003].

In case of a quantum phase transition no thermal fluctuations are present since $T = 0$. That means that the ground state energy of the system under consideration has to be non-analytic as a function of one or more of its parameters. A quantum phase transition therefore corresponds

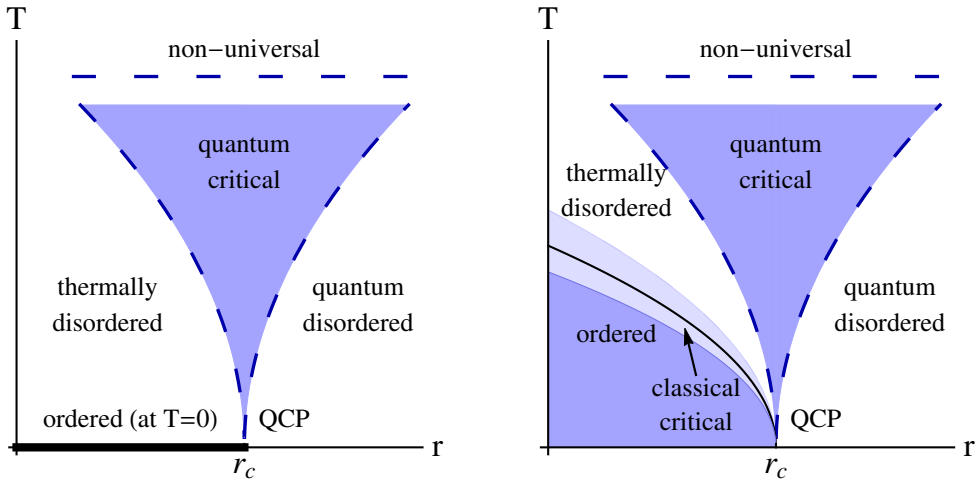

Figure 2.7: Schematic phase diagrams. The phase diagrams in vicinity of a quantum critical point (QCP; located at ($T = 0$,$r = r_c$)) are plotted in dependence on temperature T and control parameter r. While on the left order is only present at zero temperature, on the right order exists also at finite temperature. The boundaries of the quantum critical phase, in which leading critical singularities can be observed, are indicated by dashed lines. On the right a classical phase transition is indicated by the solid line around which classical critical behavior is found. The figure is adapted from Vojta [2003].

to the case where a change in the microscopic couplings of the Hamiltonian results in different properties of the ground state. To see whether quantum mechanics are important at a certain phase transition Vojta [2003] gives the following reasoning: two energy scales, namely $\hbar\omega_c$ and k_BT have to be compared, whereupon the former corresponds to the typical energy of long-distance order parameter fluctuations and the latter to the thermal energy. As discussed above, the typical time scale τ_c diverges in vicinity of a phase transition leading to

$$\hbar\omega_c \propto |t|^{\nu z} \propto |r - r_c|^{\nu z}, \tag{2.24}$$

where r is the parameter driving the phase transition. That means that the typical energy of long-distance order parameter fluctuations $\hbar\omega_c$ vanishes at the phase transition. At any finite temperature quantum mechanical effects will be suppressed by thermal effects once the thermal energy dominates over $\hbar\omega_c$. Consequently, any phase transition at finite temperature may be treated classically, giving rise to the notion "classical phase transitions". In contrast, a phase transition at $T = 0$, where the phase transition is a function of a non-thermal parameter, is always dominated by quantum mechanical effects leading to the term "quantum phase transition". Figure 2.7 shows two typical phase diagrams corresponding to the cases in which an ordered phase is only present at zero temperature and in which an ordered phase is present also at finite temperature, leading to a classical phase transition. Both phase diagrams include a "quantum disordered" region in which quantum fluctuations dominate and a "thermally disordered" region in which thermal fluctuations dominate. For $t > 0$ they are separated from the "quantum critical" region by crossovers in which both types of fluctuations are important and the boundaries are determined by $k_BT > \hbar\omega_c$, where $\hbar\omega_c$ is a function of r as shown in Equation (2.24). We note that the quantum critical point marks the end of the classical phase transition if there is any.

2.3.2. Phase transitions in Rydberg gases and exciton bilayer systems

One of the earliest works on the topic of phase transitions in ultracold Rydberg gases done by Lukin et al. [2001] suggested to use Rydberg atoms for quantum information processing. The idea used here is based on the blockade effect (see e.g. Altshuler et al. [1991]) which forbids two nearby atoms to be in the Rydberg state simultaneously. The blockade effect is introduced in Section 2.1.2. Reviews on this topic are e.g. written by Weidemüller [2009], and Singer et al. [2004], who observe a density dependent suppression of excitation as an onset of the blockade effect. Based on this knowledge practical proposals of how to use this blockade for quantum information purposes such as quantum gates were made, as e.g. done by Jaksch et al. [2000]. With the discovery of the blockade effect the idea of the Rydberg crystal arose, in which the excited Rydberg atoms form a regular pattern corresponding to a lattice (see e.g. Schausz et al. [2012]).

The concept of the Rydberg crystal has been subject to various investigations. Pohl et al. [2010], for example, describe a method to control many-body states of an ensemble of interacting Rydberg atoms in an optical lattice enabling them to create Rydberg crystals with different lattice spacings depending on the choice of parameters. Accordingly, Zeller et al. [2012] rely on the concept of the chirped laser pulse, which was introduced in Section 2.2.1, to demonstrate the spatial ordering of the many-body ground state of one and two-dimensional arrays of Rydberg atoms. Also Cinti et al. [2010] simulate a novel phase by using Monte Carlo techniques, which has crystalline structure with super solid character, meaning that dissipationless flow is possible in the phase. They argue that the resulting crystal is of triangular form. This is justified by the shape of the correlation function, which has equidistant maxima and minima. This idea was previously treated e.g. by Büchler et al. [2007], who use polar molecules instead of atoms and arrive at a qualitatively similar correlation function. Honer et al. [2010] discuss the crossover from a phase that is dominated by two-particle interaction to a phase of collective interaction.

In a certain regime electronic bilayer systems, which will be introduced later, behave in the same way as the Rydberg atoms with the only difference being their $1/r^3$ interaction potential. Here also different phases have been considered, as e.g. done by Astrakharchik et al. [2007] by means of quantum Monte Carlo techniques. The phase transition is discussed by Lozovik and Berman [1997], too. At this point we would like to skip the details and return to them in Chapter 4.

A great advance in the field on phase transitions of interacting Rydberg gases has been made by Weimer et al. [2008]. Here a mean field calculation is used to predict quantum critical behavior for zero detuning of the excitation laser, namely a universal scaling behavior which is experimentally confirmed (up to finite size effects potentially resulting from a mixture one- and three-dimensional character of the system; see Heidemann et al. [2007]) as shown by Löw et al. [2009]. This universal scaling behavior manifests itself in a power law dependence of the excited fraction of Rydberg atoms on the dimensionless parameter $\alpha = \hbar\Omega/Cn^2$, where n is the density of ground state atoms and all other parameters as above. The existence of the quantum critical point detected this way leads to the prediction of a hypothetical phase diagram as shown in Figure 2.8. It should only be understood as a rough estimation and therefore neither the axes are scaled nor is the functional dependence of the phase boundaries known. The phase diagram is divided into the para-magnet, the critical region and the crystalline phase. As stated by Sela et al. [2011], who analyze the melting of one-dimensional crystals, there in fact exist various crystalline and liquid-like (para-magnetic) phases.

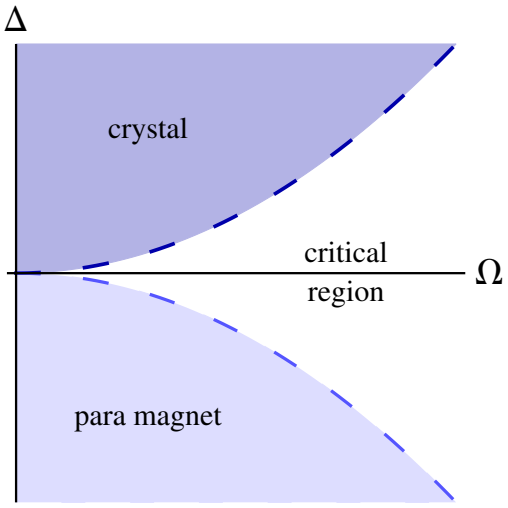

Figure 2.8: Sketch of the hypothetical phase diagram of interacting Rydberg atoms. The diagram shows three phases: the para-magnet which corresponds to the unordered phase, the critical region, and the crystalline phase. The figure is adapted from Weimer et al. [2008].

2.4. Statistics

The major goal of this thesis is to analyze and predict the statistical properties of interacting many-particle systems. The basic statistical tools needed will be introduced in this section. Being already mentioned in Section 2.3 the correlation function will be introduced in greater detail in Chapter 3, where it is directly discussed with the corresponding results of the simulations.

2.4.1. Probability distribution and full counting statistics

The definition of a probability distribution was first given by Kolmogorov [1933]. For a non-empty set Ω and $\mathcal{A} \subset \mathcal{P}(\Omega)$ a σ-algebra, where $\mathcal{P}(\Omega)$ is the power set of Ω, a mapping $P : \mathcal{A} \to [0, 1]$ is called a probability distribution on $(\Omega, \mathcal{A})$ if the following three requirements are met:

- $P(\Omega) = 1$,
- $P(A) \geq 0$ for all $A \in \mathcal{A}$, and
- $P(\bigcap_{i=1}^{\infty} A_i) = \sum_{i=1}^{\infty} P(A_i)$ for all pairwise disjoint sets $A_i \in \mathcal{A}$.

Instead of following the rigorous mathematical approach we would like to proceed in a less formal way. In the cases treated in this thesis the probability distribution $P(Q)$ is the probability to find Q excitations in a cloud of N particles. For this case all of the above criteria are obviously fulfilled. Once $P(Q)$ is known the n-th moment

$$\langle Q^n \rangle = \sum_{Q=0}^{N} Q^n P(Q) \tag{2.25}$$

of the distribution can be calculated. The knowledge of all moments $\langle Q^n \rangle$ is of course equivalent to the knowledge of the probability distribution. In practice it is more convenient to use cumulants instead of moments, even though the contained information is the same. The cumulants $\langle\langle Q^n \rangle\rangle$ are directly related to the moments. For the first three orders

$$\begin{aligned} \langle\langle Q \rangle\rangle &= \langle Q \rangle, \\ \langle\langle Q^2 \rangle\rangle &= \langle Q^2 \rangle - \langle Q \rangle^2, \qquad \text{and} \\ \langle\langle Q^3 \rangle\rangle &= \langle Q^3 \rangle - 3\langle Q^2 \rangle \langle Q \rangle + 2\langle Q^3 \rangle. \end{aligned} \tag{2.26}$$

Equations for higher order cumulants and moments are easy to obtain from the cumulant generating function as described below, but not shown here since the third cumulant will be the highest one treated throughout this thesis. Besides using the definition given above the moments can be obtained using the moment generation function, which is given by

$$M_Q(\lambda) = \langle e^{\lambda Q} \rangle = \sum_{Q=0}^{N} e^{\lambda Q} P(Q). \tag{2.27}$$

From this expression the moments can be obtained simply by

$$\langle Q^n \rangle = \partial_\lambda^n M_Q(\lambda)|_{\lambda \to 0}, \tag{2.28}$$

where ∂_λ represents the derivative with respect to the "counting field" λ. Analogously the cumulant generating function (CGF) $\chi(\lambda)$ is defined as

$$\chi(\lambda) = \ln(\langle e^{\lambda Q} \rangle), \tag{2.29}$$

which is often also referred to as "full counting statistics" in the context of transport phenomena (in mesoscopic systems). From it the cumulants can be obtained via

$$\langle\langle Q^n \rangle\rangle = \partial_\lambda^n \chi(\lambda)|_{\lambda \to 0}. \tag{2.30}$$

Once the first three cumulants have been calculated or measured in experiment, the Mandel parameter M (introduced by Mandel [1979]) and its analog for the third cumulant M_3, which are defined by

$$M = \frac{\langle\langle Q^2 \rangle\rangle}{\langle\langle Q \rangle\rangle} - 1 \qquad \text{and} \qquad M_3 = \frac{\langle\langle Q^3 \rangle\rangle}{\langle\langle Q \rangle\rangle} - 1, \tag{2.31}$$

can be derived. These expressions, which are closely related to the Fano factor used in mesoscopic transport theory, can be taken as a measure of similarity to the Poisson distribution. In the case of the Poisson distribution, which is given by

$$P_{\mu,\text{Poisson}}(Q) = \frac{\mu^Q e^{-\mu}}{Q!}, \tag{2.32}$$

one finds that all cumulants are given by $\langle\langle Q^n \rangle\rangle = \mu$. That means that M and M_3 vanish in the case of the Poisson distribution. A distribution for which $M > 0$, which corresponds to a distribution that is wider than the Poisson distribution, is called super-Poissonian while a distribution with $M < 0$ is called sub-Poissonian. Although they are often connected to photon counting statistics, one has to pay close attention when relating bunching or anti-bunching of photons with the character of the underlying statistics, as it is shown by Zou and Mandel [1990]. This in particular applies to the concept of the polariton introduced in Section 2.2.2, where spatial correlation are inferred from the photon counting statistics.

Chapter 3

Statistical properties of Rydberg gases from exact diagonalization

3.1. The Hamiltonian

As explained in Chapter 2 the system of interacting Rydberg atoms can be treated as an ensemble of two-level subsystems, each of which consists of a ground state $|g\rangle$ and a Rydberg state $|r\rangle$ which are coupled via a laser field with Rabi frequency Ω. The laser field frequency ω_L is detuned by Δ from the transition frequency of these two states, where we primarily treat the case $\Delta > 0$. Within the frozen gas approximation the atoms are fixed in space for the duration of an experimental cycle. The interactions of a two-level atom with a laser field may be treated within rotating wave approximation, as e.g. done by Walls and Milburn [2008] or Scully and Zubairy [1997] in the framework of quantum optics. The interaction between the atoms is of van der Waals type and explained in Section 2.1.1. The Hamiltonian, which is given as the sum of two terms which correspond to the atom-laser interaction and the term arising from the interactions between the atoms, is given by

$$\mathcal{H} = -\frac{\Delta}{2}\sum_{i=1}^{N}\sigma_z^i + \frac{\Omega}{2}\sum_{i=1}^{N}\sigma_x^i + \frac{C}{4}\sum_{i=1}^{N}\sum_{j\neq i}^{N}\frac{\sigma_z^i\sigma_z^j}{r_{ij}^6}, \tag{3.1}$$

as it is also presented by Robicheaux and Hernández [2005] and Pohl et al. [2010]. Here N is the total number of atoms and r_{ij} the distance between atoms i and j. In general other types of interactions, e.g. dipole-dipole interactions which also can be found in Rydberg systems as explained in Section 2.1.1, can be treated simply by replacing the power at r_{ij} and changing the interaction coefficient correspondingly. As mentioned before this system can directly be mapped onto a (pseudo) spin-$1/2$ system in which the "spin up" state corresponds to the Rydberg state and "spin down" to the atomic ground state. From this point of view the detuning Δ and the Rabi frequency Ω correspond to magnetic fields in z- and x-direction, respectively. The Hamiltonian (3.1) then represents an Ising model with random couplings in transverse field. Throughout this work the nomenclature of Rydberg gas and spin-$1/2$ system will be used interchangeably.

3.1.1. Dimensionless parameters

As discussed above the Hamiltonian (3.1) can both be interpreted as the representation of an ultracold Rydberg gas as well as a spin-1/2 system in a magnetic field. To emphasize this equivalence and also (even more important) to make the results presented here comparable to experimental ones it is essential to express all quantities in terms of dimensionless parameters. To do so Weimer [2010] defines two dimensionless parameters

$$\alpha_{\mathrm{W}} = \frac{\Omega}{C_p n^{p/d}} \qquad \text{and} \qquad \eta_W = \frac{\Delta}{C_p n^{p/d}}, \tag{3.2}$$

where the index p relates to the type of interaction and the index d to the dimension of the regarded system. Also we have set $\hbar = 1$ in this equation. In this work we would like to introduce new parameters which of course are equivalent to the ones shown in Equation (3.2) since there is a bijective mapping between them. By introducing these new parameters we hope to accentuate the origin of different effects, e.g. which effects are caused by interactions and which ones are not. They are given by

$$\zeta_C = \frac{1}{\eta_W} = \frac{C_p N^{p/d}}{\Delta L^{p/d}} \qquad \text{and} \qquad \kappa_\Omega = \frac{\alpha_{\mathrm{W}}}{\eta_W} = \frac{\Omega}{\Delta}. \tag{3.3}$$

Instead of using the abbreviations ζ_C and κ_Ω we will display the fractions by which they are defined. The simple reason for this is that the dimension of the system and the distance dependence are "hidden" within these parameters. Thus, confusion can be avoided by showing the exponent p/d. As previously mentioned in Section 3.1 the case $p = 6$ will be treated throughout this chapter and most other parts of this work. The dimension of the system will be given explicitly for every result in the text, but can also be deduced from axes labels in this convention.

3.2. The non-interacting case

The system consisting of N non-interacting two-level systems is going to be our first approximation to the full problem. In this regime the Hamiltonian can be written as the sum of single particle Hamiltonians

$$\mathcal{H} = \sum_{i=1}^{N} \mathcal{H}_i, \qquad \text{where} \qquad \mathcal{H}_i = -\frac{\Delta}{2}\sigma_z^i + \frac{\Omega}{2}\sigma_x^i \tag{3.4}$$

as can be seen from Equation (3.1) by setting $C = 0$. The Hamiltonian separating into N two-level subsystems allows to treat only one thereof. Since the analytical calculation yields the same result for each atom, the expectation value $\langle Q \rangle$ of the total number of excitations Q can be computed. It is simply given by the product of the single particle excitation probability and the number of particles N. Here the fact that a repeated (nondestructive) measurement of the spin state of a

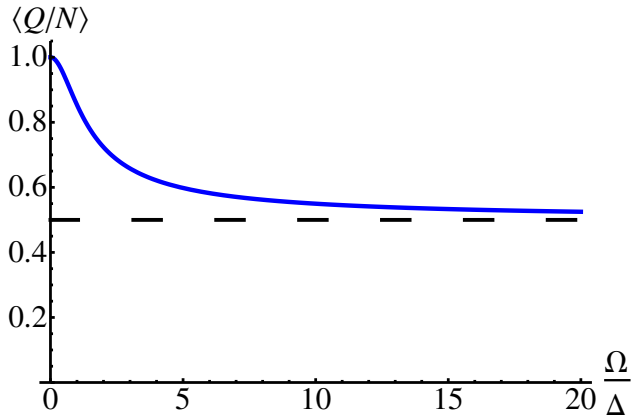

Figure 3.1: Excited fraction in the non-interacting case. The excited fraction of atoms, which corresponds to the mean magnetization of a single spin, is shown in dependence on the ratio of Ω and Δ. In the limit of this ratio being small unity is approached. This happens because the major contribution to the ground state is the state in which the spin is (almost) aligned in z-direction, which is the quantization axis of this system. In the limit of the ratio being large both orientations of the spin are equally probable, leading to an equal probability of measuring "spin up" or "spin down".

single atom is equivalent to the simultaneous measurement of the state of numerous atoms is used. The expectation value of the excited fraction then again is obtained by dividing the number of excitations by N. That means that the excited fraction is simply given by the single particle excitation probability. The same argumentation may be used for any higher cumulant which can be obtained in a similar way. This reasoning is based upon the fact that the distribution of the number of excitations is binomial, ergo

$$P(M) = \left(\begin{array}{c} N \\ M \end{array} \right) f_R^M (1 - f_R)^M, \tag{3.5}$$

where f_R is the probability of every single atom to be excited (independent of all other atoms). Following the above reasoning f_R is equal to the excited fraction of atoms, which is given by Q/N. Therefore, our primary interest lies in the calculation of f_R and its expectation value.

As stated in Equation (3.4) the Hamiltonian is given as the sum over single particle Hamiltonians (the index is dropped here) and writes as

$$\mathcal{H} = -\frac{\Delta}{2}\sigma_z + \frac{\Omega}{2}\sigma_x = \frac{1}{2}\left(\begin{array}{cc} -\Delta & \Omega \\ \Omega & \Delta \end{array} \right) \tag{3.6}$$

in matrix form. This matrix is diagonalized yielding the eigenvalues $\lambda_{1,2} = \pm\sqrt{\Delta^2 + \Omega^2}$ with corresponding eigenstates

$$|e_{1,2}\rangle = \frac{1}{N_{1,2}} \left(\begin{array}{c} 1 \\ \frac{\lambda_{1,2}-\Delta}{\Omega} \end{array} \right) \qquad \text{with normalization} \quad N_{1,2} = \sqrt{1 + \left(\frac{\lambda_{1,2} - \Delta}{\Omega} \right)^2}. \tag{3.7}$$

From this the expectation value of the single atom excitation probability f_R is immediately found to be

$$\langle f_R \rangle = \langle Q/N \rangle = \frac{1}{2}\left(1 + \frac{1}{\sqrt{1+\Omega^2/\Delta^2}}\right) \tag{3.8}$$

by using the definition of the expectation value for a system in given state $|\mathrm{GS}\rangle$

$$\langle Q/N \rangle = \langle \mathrm{GS}| \frac{1}{2}\left(\sigma_z + \mathbb{1}\right)| \mathrm{GS}\rangle. \tag{3.9}$$

This result is shown in dependence on the ratio of Ω/Δ in Figure 3.1. The limits of $\Omega/\Delta \to 0$ and $\Omega/\Delta \to \infty$ can be well understood in the language of the spin model: if Ω/Δ is very small the magnetic field has a much larger component in z- than in x-direction, aligning all spins with the z-direction. In the case of very large Ω/Δ the magnetic field vector points almost in x-direction, leading to equal probabilities of measuring "spin up" and "spin down" in the z-direction. Equation (3.8) should be kept in mind for later comparison with results of the interacting system.

3.3. Statistics of excitations in Rydberg gases

In this section the excitation statistics, meaning the distribution of the number of excited atoms, will be introduced. Later, the cumulants of this distribution will be used for the estimation of the magnitude of the critical parameter at the phase transition. We start with a preliminary remark concerning observables and expectation values thereof before we introduce the algorithm and approximations. Finally, the results for the statistics will be presented. At this point we would like to emphasize that we are interested in ground state properties of the system only.

3.3.1. Expectation values versus measurements

A remark that has to be made before we start to discuss the actual algorithm is the fact that we will deal with expectation values rather than "measurements". By this we mean that if we have found a state $|\mathrm{GS}\rangle$ to be the ground state of our system we call a generally non-integer quantity

$$Q = \langle \mathrm{GS}|\hat{Q}|\mathrm{GS}\rangle \tag{3.10}$$

the number of excitations by abuse of notation. Whenever $\langle Q \rangle$ is mentioned it refers to the expectation value obtained from the full statistics, ergo the mean. This means that the quantum mechanical expectation value is always taken for any observable and therefore it is not indicated. The "$\langle\rangle$"-brackets always refer to the statistical average taken over multiple arrangements of atoms.

A real measurement in contrast, as it was explained in Section 2.2.1, always yields integer numbers as a result. This follows from the fact that a measurement always corresponds to a projection which

in this case is the projection on a state in which every atom is either excited or in its ground state but never in a superposition of both. Therefore, this set of states is the most natural candidate for a basis to start our calculations with.

We want to note that it is of minor importance whether one considers the measurements or the expectation values for the effects we want to discuss in the following. This follows from the fact that the means of the distribution generated both ways coincide, while the variances do not match but show qualitatively very much the same behavior. This is discussed in Appendix A.1. We are aware that the examples shown there are no proof but only serve the aim of making the above statement more feasible.

3.3.2. The algorithm

Now we will introduce the algorithm which is used to obtain the ground state of the system. We start by generating N random uniformly distributed positions in the volume V. As noted above we chose the basis of states in which an atom is either excited or in its ground state. Every single basis state can now be represented by a vector consisting of "↑" for excited and "↓" for ground state atoms. These symbols can be mapped to "1" and "0", respectively. The resulting vector can be understood as a binary number and thus can be rewritten in the decimal system. In this way every state is uniquely linked to an integer number. To clarify this the following state in the case of $N = 5$ is given as an example:

$$|\downarrow\downarrow\uparrow\downarrow\uparrow\rangle = |00101\rangle = |5\rangle. \tag{3.11}$$

We now can express the Hamiltonian as a matrix with respect to this basis. It is given as a $2^N \times 2^N$-matrix. The diagonal elements of this matrix depend on $Cn^{6/d}/\Delta$, while the off-diagonal elements depend on Ω/Δ. A simple calculation shows that only

$$T = N2^N \tag{3.12}$$

entries of the $2^N \times 2^N$-matrix are non-zero, which states that the matrix is sparsely occupied. Even though this reduces the space required to store the complete matrix, it is only possible to treat small numbers of atoms N (up to ≈ 10). To circumvent this obstacle two types of approximation are introduced in the next section, which both rely on the truncation of the Hilbert space. Having applied the approximation, the size of the Hamiltonian matrix is reduced, which in principle allows for the treatment of arbitrarily large numbers of particles regarding the storage. Still the number of particles is kept $N \leq 30$ throughout this thesis for two reasons: for large numbers of atoms N both types of approximation lose their validity since physically relevant states might be truncated from the Hilbert space. In our case this limit was not reached and all of the results presented were checked to be independent of the approximation. The second reason the number of atoms N is limited is the computation time that is required to chose the states which remain after the truncation procedure. This time grows as 2^N in the limit of large N, which means that each additional atom will double the computation time.

Once the Hamiltonian matrix is computed it is diagonalized using the Lancosz algorithm, which is explained in Appendix A.3, to obtain the eigenvalues and eigenstates. The ground state, which is the eigenstate corresponding to the smallest eigenvalue, is written as a linear combination of the basis states introduced above

$$|\mathrm{GS}\rangle = \sum_{i=0}^{2^N-1}{}' \alpha_i |i\rangle, \tag{3.13}$$

where $\sum'$ runs over the subset of basis states that remained after truncation. The coefficients α_i squared give the probability to measure a certain basis state in the ground state (cf. remark about expectation value versus measurement in Section 3.3.1). Now we are able to compute any observable of the ground state as it is given as a linear combination of the basis states.

We can now repeat the above procedure numerous times leaving us with a histogram for each observable that we calculated for every realization. Obviously, a prominent quantity which is of major interest is the number of excited particles. A thorough analysis of its distribution will be presented in the following. A typical distribution for both cases of approximation is discussed in Section 3.3.4.

A simple version of the source code of the above routine can be found in Appendix A.2. In this version only the most elementary steps are included to give a general idea of the functionality of the program.

3.3.3. Two types of approximation

We briefly want to introduce the two types of approximations which are used throughout this chapter. They both rely on a truncation of the Hilbert space in order to obtain an effective Hamiltonian which is the original Hamiltonian in the respective subspace. This can be understood as a projection on a previously chosen subspace. The approximation either relies on

- considering only states with a limited number of excitations $M^* < N$ that contribute to the ground state

or

- chosing the set of k basis states with the lowest energy.

Both approximations obviously result in a smaller number of basis states but have different advantages and drawbacks. While in the first case only small numbers for the limit of excitations can be chosen, since otherwise too many basis states remain, the number of states in the second case is fixed a priori and basis states with an arbitrary number of excitations can contribute. In the first case all relevant off-diagonal elements of the Hamiltonian remain in the effective Hamiltonian, while in the second case some of them are lost. Therefore, it seems reasonable to claim that the error of the approximation in the second case increases with Ω even though no estimation can be made about the error size. In the first case we have to ensure that no physically relevant state is

lost during the procedure. This requires a good a priori guess of what the result is going to be. Consequently, it is only valid in the case of large interaction strength since only then the number of excitations in the system is small enough.

We find that the first case is mainly useful to get a first insight to the problem but fails in the regime of larger number of excitations. Therefore, results for this approximation are very sparsely shown and it is indicated whenever this approximation is used. Every result for which it is not explicitly stated which approximation is used has been obtained by approximation number two. In any case we checked for all the data presented here that no effect is generated by the choice of the cut-off either in the number of excitations or in the number of contributing basis states.

3.3.4. Histograms of the number of excited atoms

From the histogram in principle all statistical information such as the cumulants can be obtained. In the limit of a large number of samples it converges towards the probability distribution of the observed process. As already discussed in Section 3.3.1 in our routine expectation values are calculated rather than probabilities to measure a certain result. This makes a comparison to experimental data, such as the ones shown by Viteau et al. [2012], impossible. Also, we may not directly extract the information of whether the underlying probability distribution has sub- or super-Poissonian character. In Section 3.3.5 we will show why the information obtained by taking the expectation value still is very valuable.

Figure 3.2 shows two histograms corresponding to a situation of small and large Rabi frequency Ω while all other parameters are kept constant. Two different bin sizes are used in each of the histograms to display the same set of data to demonstrate the differences of the distributions. While in the case of a small Ω most values are close to an integer number of Rydberg atoms, the distribution is smeared out in the case of a large Ω, which can only be seen in the case of the small bin size. This effect can be explained as follows: in the basis chosen in Section 3.3.2 the off-diagonal elements of the Hamiltonian matrix depend on Ω only. That means that if Ω is very small the off-diagonal elements become negligible resulting in an (almost) diagonal matrix. The eigenvectors of a diagonal matrix are the corresponding basis vectors and therefore the ground state is the basis state with the smallest diagonal element. A small but finite value of Ω results only in slight admixing of other basis states. Since the basis states have integer numbers of excitations the ground state will have an (almost) integer number of excitations as well. The situation changes in the case of a Rabi frequency Ω which is not negligible compared to the other energy scales in the system. The off-diagonal elements lead to a mixing of basis states corresponding to different numbers of Rydberg atoms leading to non-integer numbers.

As mentioned above, the comparison to experimental data is not possible due to the fact that expectation values are used instead of probabilities for certain numbers of Rydberg atoms to be measured. This also does not allow to decide whether a given distribution has sub- or super-Poissonian character, as has been investigated e.g. by Cubel Liebisch et al. [2005] (see also Cubel Liebisch et al. [2007]).

In the description of the system in terms of interacting spins in magnetic fields the reasoning is completely analogous. In case of a weak magnetic field in x-direction the linear combination representing the ground state has only few (or possibly even only one) major contributions. That means that in the case of small Ω the truncation of the Hilbert space could safely be taken to the

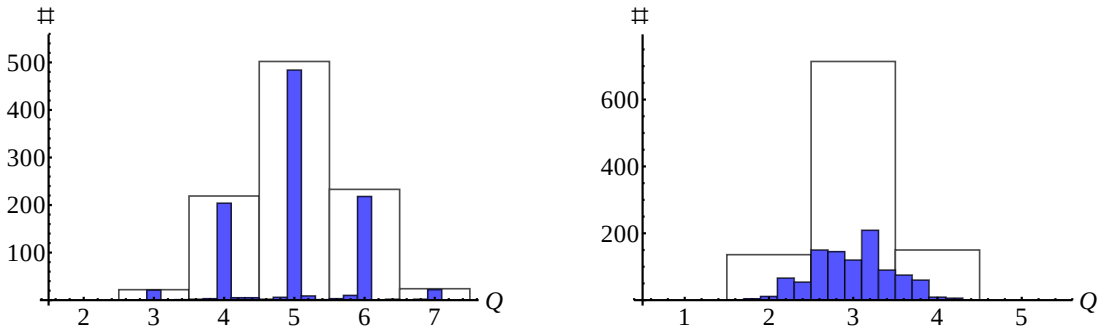

Figure 3.2: Histograms of the number of Rydberg atoms. Both bright blue and white bins correspond to the same data, only the bin size has been changed from 0.2 to 1. In the case of low Ω (left panel) mostly values close to integers are obtained, while in the case of large Ω (right panel) the peaks merge to form a continuous distribution. The data sets correspond to $Cn^6/\Delta = 2.62$ and $\Omega/\Delta = 0.05$ (left panel) and $\Omega/\Delta = 10$ (right panel).

limit of taking into account only very few basis states.

3.3.5. Cumulants as functions of external parameters

For any histogram as the ones shown in Section 3.3.4 all cumulants may be calculated from the measured or simulated data. Of course, this can only be done within certain error margins which depend on the number of samples used to generate the histogram. Additionally, the error margin increases with the order of the cumulant. Even though it is possible to generate an arbitrarily large amount of data in our simulation to reduce possible statistical errors below any previously defined threshold only the first (mean) and second (variance) cumulant are treated in this section. As explained in Section 2.4.1 they suffice to calculate the Mandel parameter M which allows one to classify the distribution as being super- or sub-Poissonian. Since we always treat the expectation value instead of the probability of measurement results the absolute values of the variances (and consequently of the Mandel parameter as well) may not be compared to experiment.

Instead of comparing the absolute values to experiment we proceed by analyzing the dependence of mean and variance on the interaction strength. Based on the prediction of the phase diagram by Weimer et al. [2008] we expect two phases when tuning the interaction strength over a sufficiently extended range. Also, we expect the behavior of the cumulants to be very different in these phases. Whereas in the unordered phase in the regime of small interaction strength a large fraction of atoms should be excited to the Rydberg state, in the regime of strong interactions the excitation is blockaded for a fraction of atoms. This results in a change of the functional dependence of the mean on the interaction strength. For the variance, in principle, the same is expected since in the case of a small blockade radius[1] arrangements of ground state atoms can either lead to a small number of excitations (when there are tightly packed clusters) or to a large number of excitations (when there are no clusters present). In the case of a large blockade radius the inhomogeneities would have to be much larger to cause the same fluctuation of the number of Rydberg atoms.

[1] "Small" in this case is defined via a comparison to the typical particle distance which is directly related to the density. We assume to compare situations of equal density here.

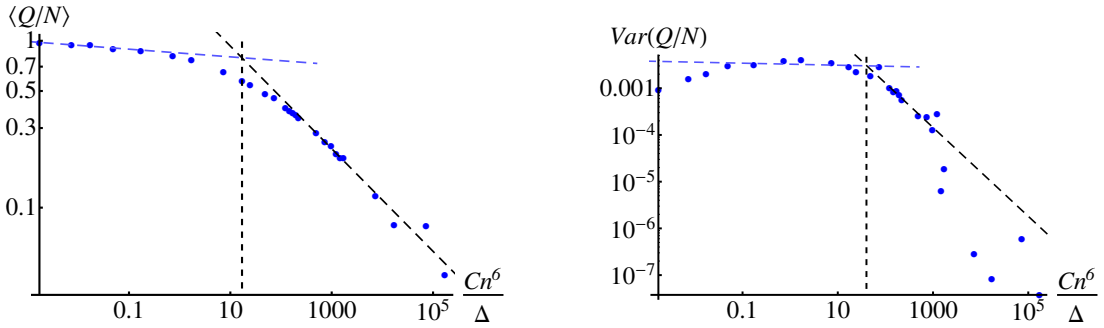

Figure 3.3: Mean (left panel) and variance (right panel) as functions of interaction strength. Power laws are fitted to the regime of low (light blue) and high (black) interaction strength. The point of intersection between the two power laws is indicated by a vertical, black dashed line. The data corresponds to $\Omega/\Delta = 0.1$.

In Figure 3.3 we show typical double logarithmic plots of excited fraction and normalized variance. These are obtained from the raw data by dividing every number of excitations by the total number of particles $N(=25$ for the data shown) and then taking mean and variance of this scaled data set. As predicted above both curves show two different regimes corresponding to the phases discussed before. Due to the finite size of our simulation the phase transition cannot manifest as a sharp kink. Instead the different regimes are fitted by power laws and extrapolated. Their intersection is the estimated critical interaction strength. We have to note that also other effects of finite size are present. We believe them to be of minor importance and discuss them in Appendix A.8.

From the data shown in Figure 3.3 the critical interaction strength can be estimated as indicated by the vertical, black dashed line. This line is defined as the intersection of the power laws which are fitted to the low and high interaction strength regime. From the mean one obtains $Cn^6/\Delta \approx 17$ and from variance $Cn^6/\Delta \approx 40$. The fit of the high interaction strength power law for the variance looks surprising at first glance since it does not seem to match the data points, but taking into account the logarithmic scale it becomes apparent that the deviation of the data points at the highest interaction strength is of the order of or even smaller then the deviation of the remaining data points for the fit.

The method presented here supplies us with an estimate of the critical interaction strength. At this point we would like to emphasize that it is only an estimate and no exact value. This becomes clear simply by noticing that the set of data points for fitting of a certain regime may be varied to obtain slightly different results. Also, the data points themselves are subject to statistical fluctuations even though a large amount of them was used to obtain Figure 3.3. Besides, the aforementioned finite size effects have to be taken into account. As a consequence of these points we thus summarize that from the numerical data it follows that at a certain interaction strength the properties of the given system change significantly, which we attribute to a phase transition. The interaction parameter can only be given up to the order of magnitude.

3.4. The correlation function

In the next step we would like to find out whether we indeed observe a significant change in the arrangement of excitations at the critical point. A sensible way to assess the internal structure of our Rydberg excitation cloud is the measurement of the relevant correlation function. In this section we are going to introduce the correlation function and afterwards present the results obtained for the interacting gas of Rydberg atoms. Even though dynamics of the correlations already have been treated (see Wüster et al. [2010]) we restrict ourselves to the static quantity. We start by following the lines of Malijevský et al. [2008] where a general pair correlation function is introduced by[2]

$$g^{(2)}(\mathbf{r}_1, \boldsymbol{\omega}_1, \mathbf{r}_2, \boldsymbol{\omega}_2) = \frac{V^2}{z}\frac{N-1}{N}\int \exp\left[-\beta U_N(\mathbf{r}^N, \boldsymbol{\omega}^N)\right] \mathrm{d}\mathbf{r}_3 \cdots \mathrm{d}\mathbf{r}_N \mathrm{d}\boldsymbol{\omega}_3 \cdots \mathrm{d}\boldsymbol{\omega}_N, \tag{3.14}$$

where V is the volume, N is the number of particles, $\beta = 1/k_B T$, $U_N(\mathbf{r}^N, \boldsymbol{\omega}^N)$ is the interaction potential, $\boldsymbol{\omega}$ is the vector of angles defining the mutual orientation of particles (e.g. molecules) and

$$z = \int \exp\left[-\beta U_N(\mathbf{r}^N, \boldsymbol{\omega}^N)\right] \mathrm{d}\mathbf{r}_1 \cdots \mathrm{d}\mathbf{r}_N \mathrm{d}\boldsymbol{\omega}_1 \cdots \mathrm{d}\boldsymbol{\omega}_N. \tag{3.15}$$

When dealing with non-spherical objects, e.g. molecules, $\boldsymbol{\omega}_i$ are used to calculate the contribution to the interaction energy which depends on the relative orientation of these objects. By assuming spherical Rydberg blockade regions and also spherical objects for any toy model thereof the interaction potential is a function of positions only. Consequently, the integration over the $\boldsymbol{\omega}_i$ can be neglected simplifying the expression considerably. Further, the Hamiltonian only contains two-particle interactions which means that the interaction potential is expressed as

$$U_N(\mathbf{r}^N, \boldsymbol{\omega}^N) = \sum_{i<j} u_{ij}(\mathbf{r}_i, \mathbf{r}_j). \tag{3.16}$$

In the case of the pair correlation function $g^{(2)}(\mathbf{r}_1, \mathbf{r}_2)$, on which we are going to omit the index in the following, this fact together with the assumption of translational invariance of the system leads to a dependence only on the distance $r = |\mathbf{r}_1 - \mathbf{r_2}|$ between the two particles. Thus, the correlation function $g(r)$ may be interpreted as a measure of probability to find a(n excited) particle (Rydberg atom) in distance r to a reference (excited) particle. In this interpretation probability is measured as the "number" of possible realizations with two particles having distance r containing N particles (Rydberg atoms) in total divided by the total "number" of valid realizations.

Now, considering for simplicity the case of N hard spheres in a volume V, one might think that this integral can simply be calculated solving the problem once and for all – which in principle is true. But for every of the N particles $d = \dim V$ integrations have to be performed. Even for moderate N the evaluation becomes very demanding and can only reasonably be done for very small N. Further

[2] Any correlation function of higher order is introduced as $g^{(i)}(\mathbf{r}_1, \boldsymbol{\omega}_1, \ldots, \mathbf{r}_i, \boldsymbol{\omega}_i) = \frac{V^i}{z}\frac{1}{N^{i-1}}\prod_{j=1}^{j=i-1}(N-j)\int \exp\left[-\beta U_N(\mathbf{r}^N, \boldsymbol{\omega}^N)\right] \mathrm{d}\mathbf{r}_{i+1} \cdots \; textd\mathbf{r}_N \mathrm{d}\boldsymbol{\omega}_{i+1} \cdots \mathrm{d}\boldsymbol{\omega}_N$.

information about how to proceed in a general case can again be found in Malijevský et al. [2008], where also the above information is extracted from.

Instead of treating the general case any further we would like to turn to the case of the interacting Rydberg atoms again. In addition to the difficulties discussed above we are now facing the problem that – depending on the spacial distribution of ground state atoms – the number of Rydberg atoms can also vary according to the probability distribution $P(Q)$ introduced in Section 2.4.1. Therefore, we proceed by employing a procedure in style of a Monte Carlo integration. Schausz et al. [2012] give

$$g(r) = \frac{\sum\limits_{i \neq j} \delta_{r,r_{ij}} \langle P_{ee}^{(i)} P_{ee}^{(j)} \rangle}{\sum\limits_{i \neq j} \delta_{r,r_{ij}} \langle P_{ee}^{(i)} \rangle \langle P_{ee}^{(j)} \rangle}. \tag{3.17}$$

as an expression equivalent to Equation (3.14) for the correlation function. In order to apply this formula to our problem we have to make certain adjustments. To be able to evaluate the above expression we have to "soften" the Kronecker-δ by dividing the maximum possible distance between two particles into k equidistant bins (see also Gärttner et al. [2012a] and Gärttner et al. [2012b] which both rely on Bellac et al. [2004]). The Kronecker-δ then can be replaced by a function that gives one if the distance of two particles matches the distance r within bin size. Initializing each bin with zero now allows to compute the correlation function cumulatively as the sum over multiple configurations of particle positions. This is done in the following routine: identically to the procedure of computing the probability distribution $P(Q)$, we start by randomly generating the positions of the N ground state atoms in the volume V. After truncation of the Hilbert space the ground state

$$|\mathrm{GS}\rangle = \sum_{i=1}^{N^*} \alpha_k |k\rangle \tag{3.18}$$

is obtained by "exact" diagonalization of the Hamiltonian. Here $|\alpha_k^2|$ defines the probability to measure the state $|k\rangle$ if the system is prepared in the ground state. We measure the distance between every two particles and assign each pair to the bin corresponding to this distance. Then we evaluate

$$\left(\sum_k^* |\alpha_k^2| \right)_{ij}, \tag{3.19}$$

where the sum runs over all states $|k\rangle$ in which the members of the present pair are excited (indicated by the star) and add this quantity to the value already present in the bin. The indices i and j in expression (3.19) stand for the particles considered and the sum has to be evaluated for every pair of particles in the present realization separately. This procedure is repeated numerous times for randomly generated realizations of ground state atom positions. Each of these realizations can now be understood as a Monte Carlo sample, just as mentioned above. In this sense the expectation

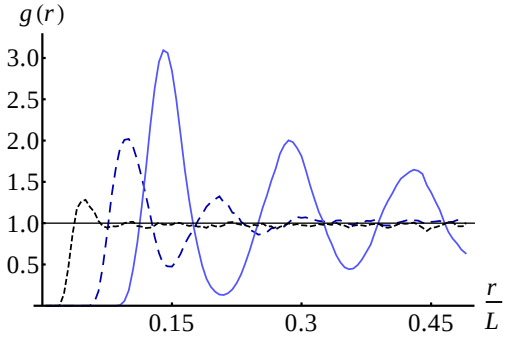

Figure 3.4: Correlation functions for different values of interaction strength in the one-dimensional case. The curves correspond to $Cn^6/\Delta = 977$ (light blue, solid line), $Cn^6/\Delta = 97.7$ (dark blue, long dashed line), and $Cn^6/\Delta = 0.98$ (black, short dashed line). While the black curve resembles a liquid, the dark blue curve already shows an onset of ordering having a second and a third order peak. The light blue curve clearly shows distinct maxima that are separated by minima which almost reach zero; this corresponds to the crystalline phase. The data sets are taken for $\Omega/\Delta = 0.4$.

values of Equation (3.17) are evaluated as the average over multiple arrangements of the ground state atoms.

The results obtained for various sets of parameters are presented in the following. Figure 3.4 shows three correlation functions corresponding to different interaction strength. The values are chosen such that for the lowest interaction strength the system is in the unordered phase while for the large interaction strength features of a crystal can be observed. For the intermediate interaction strength we suspect the system to be close to the transition between the two phases. As done by Pupillo et al. [2010] (see also Pupillo et al. [2009]), who also use the correlation function (among other quantities) to distinguish different phases, the following features are used to characterize these three curves: in the unordered phase liquid-like behavior is observed since there exists a blockade radius in which the probability to find two Rydberg atoms is strongly suppressed. For larger distances than the blockade radius the correlation function saturates rapidly meaning that the system does not exhibit long-range order. Increasing the interaction strength leads to the formation of peaks at which the probability of finding Rydberg atoms is increased. Also, the correlations extend over a wider range in the system. Once these correlations can be observed over the full range of the system we assume a phase transition to take place. This appears to be roughly the case for the intermediate interaction strength in Figure 3.4. At even higher interaction strength all peaks become more pronounced leading to a distinct regular ordering of the excitations. As stated by Bellac et al. [2004] the correlation function of liquid or gas cannot vanish beyond the first maximum since it is not possible to have "a fluid full of gaps". Therefore, the system has to be in a crystalline phase once the correlation function vanishes in between the maxima, which is the case when the interaction strength is increased even further.

Lesanovsky [2011] presents the correlation function for a similar system by solving for the ground state in a particular regime of parameters. One can only approve qualitative agreement – the existence of a blockade radius and the oscillatory character – between the results shown there and the ones presented here since a lattice gas is used in the former case. Interestingly, these features arise only if Δ has the correct sign. This confirms us in our choice to use Δ as a unit of energy (see Section 3.1.1).

Also, the results shown in Figure 3.4 can only compared qualitatively to correlation function obtained by different methods, as e.g. the one used by Sun and Robicheaux [2008]. Their pseudo-atom approach only allows for the correlation function to be calculated with a low number of sample distances. Additionally, perfect blockade is assumed within the blockade radius. The only common feature of the correlation function presented there and the ones in Figure 3.4 is the oscillatory character. Also, an only qualitative comparison to the correlation function shown by Heeg et al. [2012] is possible. Here correlation functions are shown which were obtained by cluster expansion and a hybrid model which treats the system as if it is composed of pairs and single atoms. In contrast to the results shown here a three-level description is used for the atoms and instead of the many-body ground state a stationary state is considered. The correlation functions display the feature of the blockade radius and the existence of a second order maximum for a certain range of parameters, but no conclusions about the existence of different phases are made.

We would like to end this section with a short remark on normalization and dimensionality of the correlation function. The correlation function can be interpreted with the help of the formula

$$n(r) = g(r)n_0, \tag{3.20}$$

where $n(r)$ is the particle density in distance r to a reference particle and n_0 is the average density of the full system. For systems which are not in the crystalline phase the normalization of the correlation function therefore is obtained by setting $n(r) = n_0$ in the limit of large r, where no correlations are observed. This gives $g(r) = 1$ in the limit of large r. Also, Equation (3.20) shows that $g(r)$ is a dimensionless quantity and therefore has no unit. All plots of the correlation function in this work use this normalization and no units are given.

3.4.1. Small distances

In Section 2.1.2 we introduced the blockade radius R_B as the distance around a Rydberg atom in which no further excitation is possible. This definition holds for the case of hard objects as will be shown in Section 3.5.2. In the case of the Rydberg gas this definition is not fully applicable as can be seen in Figure 3.5, where the correlation function is shown for small distances. It is clearly non-zero for all distances and therefore we redefine the blockade radius as the position of the first maximum of the correlation function. As we will see in the following section this definition coincides with the one made earlier in the case of hard objects. Besides the first few data points, which supposedly are affected by numerical effects, the data show power law behavior,

$$f(r; \{\alpha, \beta\}) = \alpha r^{\beta}, \tag{3.21}$$

in a wide range. The exponent is determined by fitting and found to be $\beta \approx 12$. This result appears to be reasonable since the correlation function can be expressed as a two particle expectation value and the interaction between the Rydberg atoms depends on distance as $1/r^6$. This effect may be related to the quantum nature of the system, namely the property of the ground state being a superposition of basis states. While these basis states, in which each atom distinctively is in its ground state or the Rydberg state, can be compared to classical states, the quantum mechanical many-particle ground state in contrast assigns a probability to be measured as a Rydberg atom

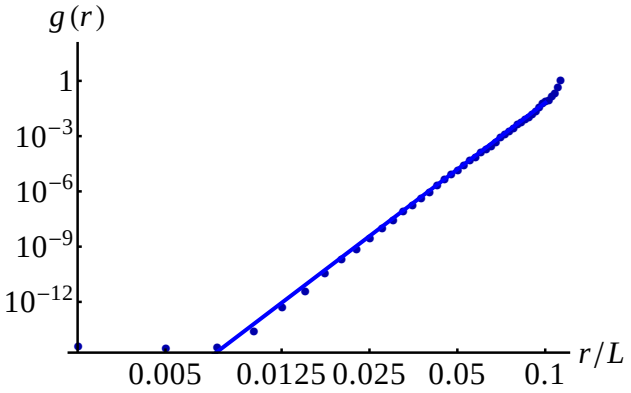

Figure 3.5: Correlation function for small distances. Both axes are plotted logarithmically. A power law is fitted to the data points revealing an exponent $\beta \approx 12.03$. At the smallest distances numerical errors cause the correlation function to deviate from this power law. The parameters are $\Omega/\Delta = 0.1$ and $Cn^6/\Delta = 2.62$.

to each single atom. In general any basis state has a finite contribution to the ground state and therefore even states in which two Rydberg atoms are close together have a finite (but very small) probability to be measured. In the average of multiple realizations then the aforementioned power law becomes observable.

3.5. Comparison to other systems

In this section we compare the correlation functions shown in Section 3.4 to the ones of other systems, namely a free electron gas and classical hard rods and spheres. The former one, being a very elementary problem, is solved in many textbooks. Mahan [2000] derives the desired formula for the two particle correlation function in a "first quantization" notation. We will briefly execute this calculation again in "second quantization". Also we show the result of the random phase approximation applied to the interacting electron gas. The correlation function of classical hard objects is the topic of numerous works which use different methods. A density expansion will be presented for the low density regime which we will come back to later and an analytical result for the one-dimensional system will be shown as well.

3.5.1. The electron gas

In a field theoretical notation the pair correlation function has to be expressed in terms of fermionic creation c and annihilation $c^\dagger$ operators. Thus, it is given by

$$g(\mathbf{x}-\mathbf{y}) = \langle \rho(\mathbf{x})\rho(\mathbf{y})\rangle / V_F^2 = \langle c_{\mathbf{x}}^\dagger c_{\mathbf{x}} c_{\mathbf{y}}^\dagger c_{\mathbf{y}}\rangle / V_F^2, \tag{3.22}$$

where $\mathbf{x}$ and $\mathbf{y}$ are real space coordinates and correspond to simple numbers in the one-dimensional case and to vectors in higher dimensions and V_F is the volume of the Fermi sphere in the respective

dimension. The expectation value can be evaluated analytically for non-interacting free electrons (only the fermionic character of the electrons plays a role) or by using different approximations. In the following we will discuss the results of the non-interacting situation and the random phase approximation.

The non-interacting electron gas

We will treat the three-dimensional case from now on and use the convention $|\mathbf{x}| = x$. The result for one and two dimensions will be given at the end only since the calculation is completely analogous and does not offer any further insight. First, we express every creation and annihilation operator via its Fourier components using

$$c_{\mathbf{x}} = \int \mathrm{d}^3 q e^{-i\mathbf{q}\mathbf{x}} \tilde{c}_q. \tag{3.23}$$

With this we rewrite Equation 3.22 to obtain

$$\langle c^\dagger_{\mathbf{x}} c_{\mathbf{x}} c^\dagger_{\mathbf{y}} c_{\mathbf{y}} \rangle = \int \mathrm{d}^3 p \int \mathrm{d}^3 q \int \mathrm{d}^3 k \int \mathrm{d}^3 l e^{-i\mathbf{x}(\mathbf{p}-\mathbf{q})} e^{i\mathbf{y}(\mathbf{k}-\mathbf{l})} \langle \tilde{c}^\dagger_{\mathbf{p}} \tilde{c}_{\mathbf{q}} \tilde{c}^\dagger_{\mathbf{k}} \tilde{c}_{\mathbf{l}} \rangle. \tag{3.24}$$

In this expression we can apply the Wick theorem to the expectation value, yielding

$$\begin{aligned} \langle \tilde{c}^\dagger_{\mathbf{p}} \tilde{c}_{\mathbf{q}} \tilde{c}^\dagger_{\mathbf{k}} \tilde{c}_{\mathbf{l}} \rangle &= \langle \tilde{c}^\dagger_{\mathbf{p}} \tilde{c}_{\mathbf{q}} \rangle \langle \tilde{c}^\dagger_{\mathbf{k}} \tilde{c}_{\mathbf{l}} \rangle - \langle \tilde{c}^\dagger_{\mathbf{p}} \tilde{c}_{\mathbf{l}} \rangle \langle \tilde{c}^\dagger_{\mathbf{k}} \tilde{c}_{\mathbf{q}} \rangle & (3.25) \\ &= \delta(\mathbf{p}-\mathbf{q}) \delta(\mathbf{k}-\mathbf{l}) n_F(\mathbf{p}) n_F(\mathbf{k}) - \delta(\mathbf{p}-\mathbf{l}) \delta(\mathbf{k}-\mathbf{q}) n_F(\mathbf{p}) n_F(\mathbf{k}), & (3.26) \end{aligned}$$

where n_F labels the well-known Fermi function, which at zero temperature is just a Heaviside-θ-function $n_F(\mathbf{p}) = \theta(\mathbf{p}_F - \mathbf{p})$. Inserting Equation (3.26) into Equation (3.24) two of the integrals can be executed immediately in each term by using the Fourier transform of the δ-distribution. The evaluation of the remaining integrals is straightforward and can be done most conveniently in spherical coordinates. The result then is given by

$$\langle c^\dagger_{\mathbf{x}} c_{\mathbf{x}} c^\dagger_{\mathbf{y}} c_{\mathbf{y}} \rangle = \left(\frac{4\pi}{3} p_F^3 \right)^2 - \left\{ \frac{4\pi}{|\mathbf{x}-\mathbf{y}|^3} \left[\sin(p_F|\mathbf{x}-\mathbf{y}|) - p_F|\mathbf{x}-\mathbf{y}| \cos(p_F|\mathbf{x}-\mathbf{y}|) \right] \right\}^2. \tag{3.27}$$

As already mentioned above the calculations for the one- and two-dimensional case are almost identical and yield the results

$$\langle c^\dagger_{\mathbf{x}} c_{\mathbf{x}} c^\dagger_{\mathbf{y}} c_{\mathbf{y}} \rangle_{1\mathrm{D}} = p_F^2 - \frac{2}{(\mathbf{x}-\mathbf{y})^2} \left[1 - \cos(p_F(\mathbf{x}-\mathbf{y})) \right] \tag{3.28}$$

and

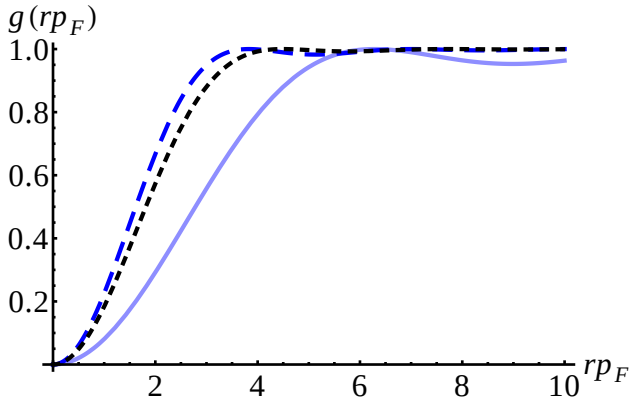

Figure 3.6: Correlation functions of free electrons. The curves correspond to one- (light blue, solid line), two- (blue, long dashed line), and three- (black, short dashed line) dimensional systems. Distances are measured in units of inverse Fermi momenta. The correlation functions of different dimensions may safely be plotted in one diagram since they are normalized by the respective volume of the Fermi sphere V_F^2 (cf. Equation (3.22)).

$$\langle c_{\mathbf{x}}^\dagger c_{\mathbf{x}} c_{\mathbf{y}}^\dagger c_{\mathbf{y}} \rangle_{2\mathrm{D}} = \pi^2 p_F^4 - \left[\frac{2\pi p_F}{|\mathbf{x}-\mathbf{y}|} j_1(p_F|\mathbf{x}-\mathbf{y}|) \right]^2 , \tag{3.29}$$

where $j_1(x)$ labels the Bessel function of first order. We would like to stress the fact that no interaction was involved in this calculation but only the bare fact that electrons are fermions and therefore obey the Pauli exclusion principle. If a spin index was introduced in Equation (3.22) one could compute a correlation function of electrons in the same or in opposite spin state. What we have calculated above corresponds to the equal spin state situation. In the other situation the result is simply given by a constant as also shown by Mahan [2000].

The results of the above calculation are shown in Figure 3.6. To make the curves corresponding to different dimensions comparable we plotted them as functions of a dimensionless parameter. While all three curves qualitatively look the same, the behavior for small arguments of one dimension compared to two and three dimensions is different. The region in which a neighboring electron is less favored extends farther in the one than in the two and three-dimensional case since in one dimension there is no additional degree of freedom (besides the bare distance) to arrange atoms in a volume. This also manifests in the slightly more pronounced maxima and minima of higher order. In the next section we want to show the results for a classical gas of hard rods and afterwards compare both free electrons and hard rods to the Rydberg atoms.

Random phase approximation

The random phase approximation (RPA) is one of the most common approximations used to treat the homogeneous electron gas. Instead of repeating the calculation at this point, which can be found e.g. in Mahan [2000], we will just present the result. The pair correlation function turns out to be related to the electric susceptibility of the electron gas. The real and imaginary parts of the electric susceptibility are presented by Giuliani and Vignale [2005] in a very comprehensive and

clearly arranged way. They are shown to be

$$\frac{\mathrm{Re}\chi_\sigma(\omega,q)}{N_\sigma} = -\begin{cases} \frac{1}{2} - \frac{1-\nu_{-\sigma}^2}{4\bar{q}_\sigma}\ln\left|\frac{\nu_{-\sigma}+1}{\nu_{-\sigma}-1}\right| + \frac{1-\nu_{+\sigma}^2}{4\bar{q}_\sigma}\ln\left|\frac{\nu_{+\sigma}+1}{\nu_{+\sigma}-1}\right| & \text{3D} \\ 1 + \frac{1}{\bar{q}_\sigma}\left[\mathrm{sign}(\nu_{-\sigma})\Theta(\nu_{-\sigma}^2-1)\sqrt{\nu_{-\sigma}^2-1} - \mathrm{sign}(\nu_{+\sigma})\Theta(\nu_{+\sigma}^2-1)\sqrt{\nu_{+\sigma}^2-1}\right] & \text{2D} \\ \frac{1}{2\bar{q}_\sigma}\ln\left|\frac{\nu_{-\sigma}-1}{\nu_{-\sigma}+1}\right| - \frac{1}{2\bar{q}_\sigma}\ln\left|\frac{\nu_{+\sigma}-1}{\nu_{+\sigma}+1}\right| & \text{1D} \end{cases} \tag{3.30}$$

and

$$\frac{\mathrm{Im}\chi_\sigma(\omega,q)}{N_\sigma} = -\begin{cases} \frac{\pi}{4\bar{q}_\sigma}\left[\Theta(1-\nu_{-\sigma}^2)(1-\nu_{-\sigma}^2) - \Theta(1-\nu_{+\sigma}^2)(1-\nu_{+\sigma}^2)\right] & \text{3D} \\ \frac{1}{\bar{q}_\sigma}\left[\Theta(1-\nu_{-\sigma}^2)\sqrt{1-\nu_{-\sigma}^2} - \Theta(1-\nu_{+\sigma}^2)\sqrt{1-\nu_{+\sigma}^2}\right] & \text{2D} \\ \frac{\pi}{2\bar{q}_\sigma}\left[\Theta(1-\nu_{-\sigma}^2) - \Theta(1-\nu_{+\sigma}^2)\right] & \text{1D.} \end{cases} \tag{3.31}$$

Here ω labels energy and q momentum. Further, the dimensionless quantities $\bar{q}_\sigma = q/k_{F\sigma}$ and $\nu_\pm = \omega/2qv_{F\sigma} \pm q/2k_{F\sigma}$ are defined, where σ is the spin index. N_σ is a dimension dependent normalization given by the density of states at the Fermi edge, thus

$$N_\sigma = \begin{cases} \frac{mp_{F\sigma}}{2\pi^2\hbar^2} & \text{3D} \\ \frac{m}{2\pi\hbar^2} & \text{2D} \\ \frac{m}{\pi\hbar^2 p_{F\sigma}} & \text{1D.} \end{cases} \tag{3.32}$$

These expressions now can be used to calculate the static ($t = 0$) structure factor

$$S(\mathbf{q}) = \int_0^\infty \mathrm{d}\omega \mathrm{Im}\frac{1}{\epsilon(\omega,\mathbf{q})}, \tag{3.33}$$

where $\epsilon(\omega,\mathbf{q}) = \chi(\omega,\mathbf{q}) - 1$ is the dielectric function. The structure factor then can be inserted into the relation

$$g(r) = 1 + \frac{1}{n}\int_{V_q} \mathrm{d}\mathbf{q}e^{i\mathbf{qr}}(S(q) - S(\infty)), \tag{3.34}$$

for the correlation function as it can be found (slightly adapted) in Mahan [2000]. In general the integrations for the Fourier transforms above have to be executed numerically. The result for the correlation function in one dimension is shown in Figure 3.7. The negative correlation function for small distances shows the deficits of the RPA in which the exact polarization diagram is replaced by the first term of its diagrammatic expansion.

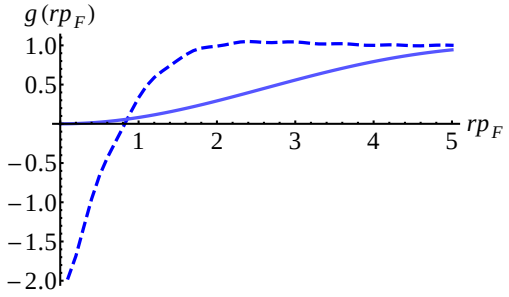

Figure 3.7: Correlation function of the one-dimensional electron gas. The correlation function resulting from the RPA at $n = 5$ (blue dashed line) is plotted as a function of distance together with the non-interacting case of the previous section (solid blue line). The RPA correlation function being negative for small distances indicates that the approximation is questionable for small distances.

3.5.2. Correlation function of classical hard spheres and rods

During the last century great progress has been made in the field of correlation functions of classical fluids. A common simple model to describe these fluids are hard spheres (or disks (2D) or rods (1D)). Various methods to obtain the correlation functions thereof have been created. We are going to present two of the most simple ones here to compare them to the correlation function of the ultracold Rydberg gas. Even though it might not appear meaningful at first glance, a modeling of Rydberg atoms by hard objects can give new insights into the underlying physics. Ates and Lesanovsky [2012] use this analogy to compute the pair correlation function by using Monte Carlo techniques.

In the regime of low density n often an expansion in powers of n is used, as explained e.g. by Malijevský et al. [2008]. Here the coefficients of the expansion

$$g(x) = \Theta(x-1)\left(1 + y_1(x)n + y_2(x)n^2 + \ldots\right), \tag{3.35}$$

in which $x = r/R_0$ with the hard sphere radius R_0 is used as a dimensionless measure of distance, are given up to second order. Instead of replicating their exact expressions we only present the resulting correlation functions in Figure 3.8. The general behavior of the curves does not change qualitatively for different (low) densities. After a sharp peak for distances slightly larger than the hard sphere radius R_0 all curves drop and for moderate densities even reach a local minimum. At some point between two and three R_0 the curves are not distinguishable from their long distance limit.

For larger densities the expansion in n is not valid anymore. In the one-dimensional case, which is the only one which will be treated here, the exact density functional can be computed. This is a big advantage over approximate calculations in higher dimensions. The original results (see Zernike and Prins [1927] for the radial distribution function[3] and Percus' work shown in the miscellany by Frisch and Lebowitz [1964] for the direct correlation) are comprehensively collected by Torquato

[3]The radial distribution function is the term for what is called pair correlation function in this work.

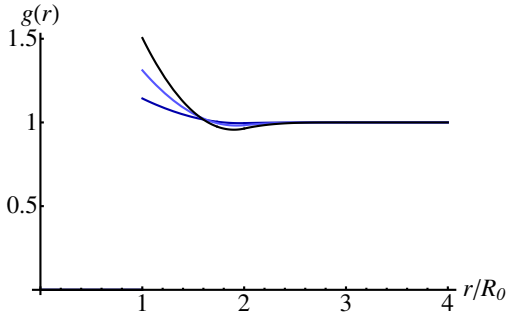

Figure 3.8: Correlation function for hard spheres in the low density regime. The curves correspond to densities $n = 0.1$ (dark blue), $n = 0.2$ (light blue) and $n = 0.3$ (black). Distances are measured in units of the hard sphere radius R_0.

[2002] and Malijevský et al. [2008]. The pair correlation function for the hard rods (which are one-dimensional analogons of three-dimensional spheres) is given by

$$g(x;n) = \sum_{k=0}^{\infty} \Theta(|x| - (k+1)) \frac{n^k (|x| - (k+1))^k}{k!(1-n)^{k+1}} e^{-\frac{n(|x|-(k+1))}{1-n}}, \tag{3.36}$$

where again x is distance measured in units of R_0, which in the one-dimensional case corresponds to half the length of a rod. The single terms of the sum corresponds to the contribution of the k^{th} nearest neighbor to the reference particle. For our purposes it is sufficient to truncate the sum at rather low k and since evaluation of Equation 3.36 is not demanding we set $k_{\max} = 10$ for the data shown here. The correlation functions corresponding to different densities are shown in Figure 3.9. While the two curves corresponding to lower density clearly display the character of a liquid the situation is somewhat difficult in the highest density case. It is not possible to apply our criterion of whether the correlations extend of the full system length because no finite volume is defined in this calculation but only the density. But another feature may be taken as an indicator of an ordered phase. In contrast to the two lower density correlation functions the correlation function for the highest density drops to zero for the first minima. Therefore, distinct orders for the neighbors of a reference particle can be given. This appears to define an ordering which one can relate to a periodic structure which one may as well entitle crystal.

3.5.3. Common features and differences

In the above Sections 3.5.1 and 3.5.2 we showed the correlation functions of the homogeneous electron gas as well as the one of classical hard spheres. Now we would like to briefly list their similarities and differences. We consider the following points:

- The feature of the blockade radius as we have defined it previously is only shared by the Rydberg gas and the classical hard rods and spheres. While in the case of the hard objects the correlation function is identically zero within the length of a rod (this is as well the case for correlation function shown by Ates and Lesanovsky [2012]), which can be taken as the definition of a hard object, and has the first maximum directly at this distance, the excitation

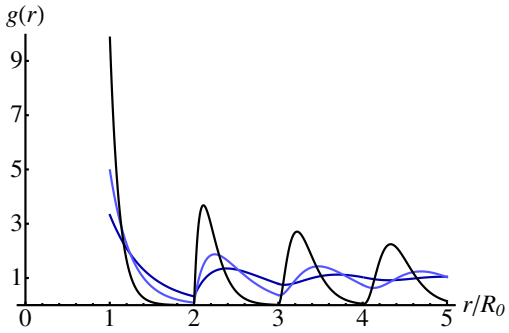

Figure 3.9: Correlation function for hard spheres in the high density regime. While the curves corresponding to $n = 0.7$ (dark blue) and $n = 0.8$ (light blue) show properties characteristic of a liquid, the $n = 0.9$ curve (black) drops to zero at least for the first few minima, which is characteristic for solids. The positions of the maxima do not coincide already for the second order maximum.

of a Rydberg atom is only strongly suppressed within the blockade radius. In the case of the electron gas neither the interacting nor the non-interacting situation display this behavior. At small distances the correlation function is strongly affected by the Pauli principle which forbids to particles to be at the same place but does not cause a maximum in the correlation function.

- In the case of the interacting Rydberg atoms a phase transition occurs at the point where correlations arise over the full length of the system. This clearly cannot be the case for the hard rods since no finite system volume is given. Even though the correlation function drops to zero indicating an ordered system (see Bellac et al. [2004]) there is no phase transition in a one-dimensional hard rod system; in higher dimensions a transition is found (see e.g. Corti and Debenedetti [1998]). For the case of the interacting electron gas one has to be careful as well. Wigner [1934] puts forward the idea of an electron crystal which was realized e.g. by Filinov et al. [2001]. That means that there is the possibility of a phase transition even though it does not manifest in the results we presented above.

- In the case of the Rydberg atoms an increased density sharpens the peaks of the correlation function. While the expression for the non-interacting electron gas does not depend on density at all the interacting electron gas obviously is affected by changes in density as can be seen in Equation 3.34. The high density result for the hard rods displays a behavior very similar to the one of the Rydberg gas.

- A minor observation is that the peaks of the correlation function of the Rydberg gas appear to be almost symmetric with respect to their centers while in case of the hard rods that clearly is not the case.

Based upon the above-mentioned points we conclude that the correlation function of the classical hard rods in the high density limit shares more features with the ultracold Rydberg gas than the low density expansion of classical hard spheres and the electron gas. That means that in the regime of $\Omega/\Delta < 1$ the Rydberg atoms behave similar to classical objects rather than quantum objects (e.g. electrons). Of course, the quantum nature of the Rydberg atoms is not negligible but the largest contributions to the ground state of the full system display classical character. Also, the imperfect blockade for small distances is evidence for the fact that the Rydberg atoms may not considered to

be fully classical objects.

At this point we would like to insert an additional remark on work shown in Section 6.2.1. There the pair correlation function is assumed to be a Heaviside-Θ-function. Taking into account the results of the previous sections this assumptions would best match with the situation of hard spheres in the limit $n \to 0$[4]. Clearly, this is no perfect choice given the knowledge of the features of the correlation function but since no correlation effects are investigated at that point it is sufficient to include the existence of the blockade radius.

3.6. The blockade radius

The blockade radius of the interacting Rydberg gas has already been mentioned before. Now we would like to show the dependence of the blockade radius on the external parameters. In terms of the correlation function the blockade radius is defined by the position of the first maximum. For every value of the Rabi frequency Ω the correlation function is calculated and the blockade radius R_B is read off subsequently. The result of this procedure is shown in Figure 3.10. The double logarithmic plot distinctively displays a power law behavior for $\Omega/\Delta \leq 1$, therefore a fit is performed in this domain with

$$f(x;\{\alpha,\beta\}) = \alpha \left(\frac{\Omega}{\Delta}\right)^{\beta}, \tag{3.37}$$

where α and β are fitting parameters. While the value for α is of minor importance one finds $\beta \approx -0.169$, which is close to $\beta = -1/6$. This result can be understood in the following way: in the regime $\Omega/\Delta \leq 1$ there are two energy scales in the system, one defined by Ω and one by the interaction strength (Δ is no energy scale since it is used as a unit of energy). The interaction strength depends both on the magnitude of C as well as the distance between the interacting particles. Therefore, the energy scales match at a certain distance giving a rough estimation of the blockade radius. Since the distance r enters the Hamiltonian (3.1) with a power r^{-6} equating the two energy scales at the blockade radius gives

$$R_B \propto \Omega^{-1/6}. \tag{3.38}$$

The same statement can be made about the blockade radius R_B in dependence on the interaction strength. Analogously to the above it can be related to C by

$$R_B \propto C^{1/6}, \tag{3.39}$$

where now the assumption of $\Omega/\Delta \leq 1$ is not necessary. In the situation where this assumption is not fulfilled different behavior can be observed for R_B in dependence on Ω, but relation (3.39) holds true. If $\Omega/\Delta < 1$ the first term of the Hamiltonian (3.1) dominates over the second term. Thus,

[4]This is one major reason why the result for hard spheres is displayed in the case of low density rather than hard rods.

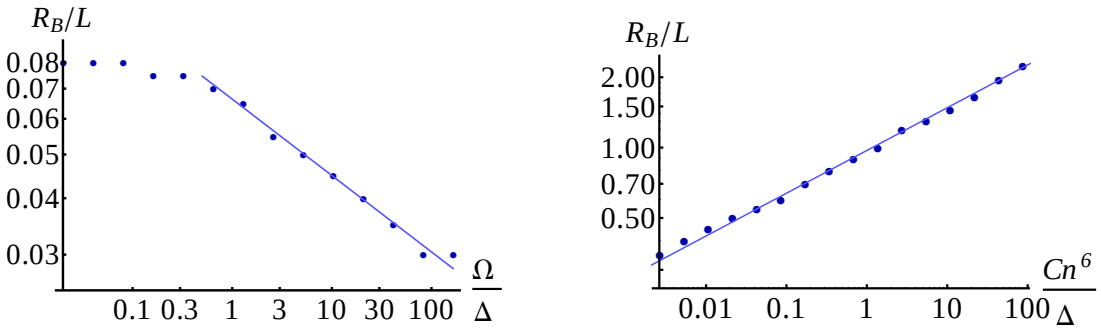

Figure 3.10: Blockade radius R_B in dependence on Rabi frequency Ω (left panel) and interaction strength (right panel). In the regime $\Omega/\Delta \geq 1$ a power law with exponent $\beta \approx 0.155$ (light blue, solid line) is found for $R_B(\Omega)$ which is explained in the text by simple comparison of energy scales. In case of the interaction dependence R_B has a power law dependence on the interaction strength for all reasonable choices of parameters. The data (dark blue) corresponds to $Cn^6/\Delta = 0.262$ (left panel) and $\Omega/\Delta = 0.05$ (right panel).

the energy scale, which the interaction strength has to be compared with, becomes a constant as a function of Ω. That means that a power law behavior is predicted for R_B as a function of C for all reasonable choices of parameters while it becomes a constant as a function of Ω in the limit of small Ω. The exponent for the power law in case of the interaction dependence is found to be $\beta \approx 0.183$, which again is close to the prediction of $\beta = 1/6$. We would like to remark that the power law behavior seems to hold true even in the regime where R_B is much smaller than the average distance between nearest neighbors.

The above results show that our intuitive predictions, which are based on simple comparison of energy scales, are matched by the numerical data. This, of course, confirms our understanding of the underlying physics of the model. Additionally, we can exclude exotic effects that arise as the interplay of the three terms of the Hamiltonian (3.1).

3.7. A section of the phase diagram

Having discussed various features of the many-particle ground state properties of the interacting Rydberg gas we now want to apply our findings to obtain the phase diagram in the space of parameters introduced in Section 3.1.1. This can be done in the following way: we use the technique introduced in Section 3.3.5 where two power laws are fitted to mean and variance of the excited fraction of Rydberg atoms in the regime of high and low interaction strength. The intersection of these two power laws then defines the critical interaction strength. We simulate the system in a wide parameter regime and for each of them estimate the critical parameters.

Figure 3.11 shows the result of this procedure. The area marked in red is the convex hull of all points corresponding to critical interaction strength. As one can see the critical region extends over a range of almost two orders of magnitude, which is attributed to the difficulties mentioned in Section 3.3.5. Also, one finds that the regions estimated by mean and variance almost coincide. We have to mention that the region estimated by using the variance does not extend over the full width of the simulated data only for the reason that the fitting procedure could not be applied with

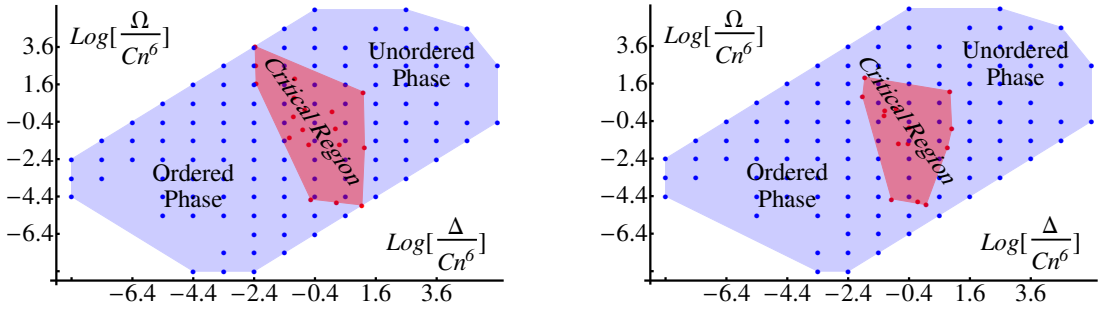

Figure 3.11: Section of the phase diagram. Blue data points correspond to a set of parameters for which simulation data has been obtained. Red data points are the estimations for the critical parameters obtained in the fashion of Section 3.3.5. The blue and red shaded areas resemble the convex hull of the respective data set and are only displayed to aid the eye. In contrast to other data shown in this work the axes are scaled in units of dimensionless parameters introduced by Weimer [2010] to simplify comparison to other data.

confidence in the limit of extreme values for the parameters. In these cases a much larger amount of data would have been required and even then it is not clear whether the fitting routine can be successful. Therefore, the critical values corresponding to these values of parameters are left out. In case the above described routine would work properly even in the case of extreme values of the parameters, the critical region would extent over the full width of the blue area.

As explained in Section 2.3, the ultracold Rydberg gas exhibits a quantum phase transition which was evidenced by Weimer et al. [2008]. Its position is found to be at $\Delta = 0$ and $\Omega = 0$ as one would also expect from general theory on phase transitions. The results shown here are not compatible with this result. Even though the quantum critical point cannot be seen in Figure 3.11 since it is a double logarithmic plot, the critical region and the quantum critical point seem to be separated in parameter space. Then again our method is not capable of assigning its phase to all points in parameter space with full confidence. Therefore, further research has to be done.

Chapter 4

Exact diagonalisation technique applied to bilayer heterostructures

This chapter is devoted to the presentation of the results of our studies on interacting excitons, most of which have already been shown in Breyel et al. [2013]. As in Chapter 3, exact diagonalization is used to obtain the many-particle ground state. Besides the different experimental realization (semiconductor hetero-structures instead of laser-cooled clouds of atoms), the main difference lies in the interaction itself. While in the case of Rydberg atoms the dipole moments are not aligned, the dipole moments of the excitons are aligned by design. Therefore, the interaction potential depends on distance as $1/r^3$ in case of the exciton condensate in contrast to the dependence of $1/r^6$ in the case of Rydberg atoms.

Since the method applied here is identical to the one presented before we shall often refer to Section 3.3.2 to avoid redundancy. The system and its experimental setup will be introduced first and then the results of the computation will be shown. Finally, we will comment on the similarities of the many-particle ground state properties of Rydberg atoms and excitons.

4.1. Indirect excitons in bilayer setups

An exciton is defined as a composite particle which consists of an electron in the conduction band of a solid Coulomb-bound to a hole in the valence band of this solid, see e.g. Ibach and Lüth [2009]. Recent experiments focus on a specific setup which is called bilayer heterostructure. Usually these setups consist of two semiconducting layers of the same material which are separated by a dielectric spacer (see e.g. Butov et al. [2002]). In the case of a bilayer heterostrucure, a sketch of which is shown in Figure 4.1, one distinguishes between direct (in same layer) and indirect (spatially separated) excitons. When these structures are irradiated by laser light of a certain frequency it is possible that electrons of the valence band of one layer tunnel through the dielectric spacer forming a bound state of electron and hole in different layers. This spatial separation between its components motivates the term indirect exciton. This is in contrast to the direct exciton, which is of minor importance to the work presented here.

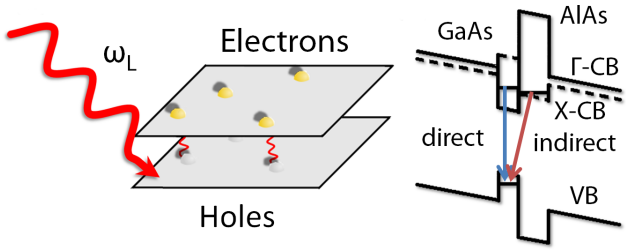

Figure 4.1: On the left a schematic bilayer system in which indirect excitons are created via an applied laser field is shown. A typical experimental realization of this would be given by a GaAs/AlAs heterostructure. Possible exciton states are shown on the right. These coupled quantum wells have two conduction bands (Γ and X) originating from different points in the Brillouin zone and allow for both the formation of direct and indirect excitons, however, with different binding energies. Breyel et al. [2013] use this figure as well.

Just as in any other bosonic many-particle system one has to take into account the possibility of Bose-Einstein condensation (BEC) for the excitons (see e.g. Keldysh and Kozlov [1968] and Blatt et al. [1962]). In addition, there are numerous works, like those of Comte and Nozières [1982], Keldysh and Kozlov [1965], and Lozovik and Yudson [1976], which consider a ground state of Cooper-pair-like quasiparticles, which are well-known from conventional Bardeen-Cooper-Schrieffer (BCS) theory. At intermediate densities, where BEC is prohibited, a third regime opens up in which the dipole moments of the excitons lead to interactions which cause correlations. Here a long-range ordering, which is comparable to a Wigner crystal (see e.g. Hartmann et al. [2005], Kulakovskii et al. [2004], Laikhtman and Rapaport [2009], Lozovik and Berman [1997], Schindler and Zimmermann [2008], and Ranganathan and Johnson [2007]), is possible but hard to detect for the simple reason that the laser-excited excitons are very fragile with respect to irradiation. Therefore, spectroscopic methods are very difficult to apply and there is a need for an alternative. One of these alternatives is given by the first order correlation function whose measurement was reported by High et al. [2012], and Alloing et al. [2012].

The approach we employ here, in analogy to what we did in Chapter 3, relies on the measurement of the first cumulants of the distribution of the number of excitons in a given sample. The corresponding experimental cycle is assumed to consist of the excitation via a laser field applied to the double well structure and the subsequent measurement of the number of excitons via their recombination luminescence. Repetition of this cycle then allows to generate the respective statistics. It is reasonable to expect that the interaction potential will lead to spatial correlations that possibly cause (long-range) ordering. The features and effects of this ordering in the underlying statistics then may be treated with the previously introduced tools. In the next section we will present the predicted results of such a measurement as well as a prediction for the correlation function which both are used to estimate the critical interaction strength of a phase transition.

We would like to briefly explain the procedure we use, even though the method is closely related to the one employed in the case of Rydberg atoms. Here we assume the system to consist of N randomly placed electrons in a fixed (one- or two-dimensional) volume with periodic boundary conditions (open boundaries are also possible but not used in this case). Since free electrons are modeled by plane waves they are not localized in real space. Therefore, the distribution of electrons at the incident of laser illumination is assumed to be uniform and random (see e.g. Snoke et al. [2002]). Each of these electrons is modeled as a two-level subsystem in which the ground state is the bare electron and the excited state corresponds to the exciton. The excitation laser is detuned

by an amount of Δ from the transition frequency between these states. The Rabi frequency Ω, which is the coupling constant between ground and excitonic state, as explained by Östreich and Knorr [1993], is of the same order as the exciton binding energy. Choosing a circularly polarized light beam at a suitable frequency enables one to create both direct and indirect excitons. For our considerations the former ones can be neglected because either the frequency can be chosen such that their excitation is suppressed, or one takes advantage of the much shorter recombination time as compared to the latter ones.

If we want to employ the same method as in case of the Rydberg atoms, we have to justify why it is appropriate to use the frozen gas approximation. The reason is the following: laser pulse duration and measurement time are less than $\tau < 0.1$ns, as claimed by Vörös et al. [2005]. The typical velocity of an exciton is $v_{\text{ex}} \approx 10$m/s, which results in a typically traveled distance of about $v_{\text{ex}}\tau < 1$nm of an exciton during an experimental cycle. This has to be compared to the size and average separation between excitons. While Kuznetsova et al. [2010] find the Bohr radius $a_B \approx 20$nm as a measure of the exciton's size, Liu et al. [2006] give an estimate of the typical separation of excitons to be about 100nm. Since both are sufficiently larger than the average distance of travel we assume the frozen gas approximation to be applicable in this system.

While in the case of the Rydberg atoms there was no alignment of the dipole moments we now have to consider the situation where this is the case since every electron hole pair is separated by the dielectric spacer of thickness d and consequently carries a dipole moment of ed perpendicular to their plane. This leads to an interaction $\propto 1/r^3$, where r is the distance between the excitons, with an interaction constant of $C = e^2d^2/\epsilon$, where ϵ is the dielectric constant of the spacer material. Typical values, as used by Kuznetsova et al. [2012], are $d = 11.5$nm and $\epsilon = 12.9$ for a GaAs/AlGaAs hetero structure.

Just as in a typical experiment (see e.g. Snoke et al. [2002]) we choose the detuning to be larger but still comparable in magnitude to the Rabi frequency. The excitation frequency typically is of the order of 1eV. The spatial extension of the simulated volume is in the range of 200-500nm. In the next section two brief calculations confirm the compatibility of our simulations with experimental conditions by estimating the system size from all other parameters.

With all the parameters being set we can now introduce the Hamiltonian of the system

$$\mathcal{H} = -\frac{\Delta}{2}\sum_{i=1}^{N}\sigma_z^i + \frac{\Omega}{2}\sum_{i=1}^{N}\sigma_x^i + \frac{C}{4}\sum_{i=1}^{N}\sum_{j=1}^{i-1}\frac{(1+\sigma_z^i)(1+\sigma_z^j)}{|\mathbf{r}_i - \mathbf{r}_j|^3}. \tag{4.1}$$

It is again written in the spin notation in which "spin up" corresponds to an exciton and "spin down" to a bare electron. Comparing this Hamiltonian to the one introduced in Section 3.1 for the Rydberg atom system one notices that the only difference lies in the different exponent ($p = 6$ in Equation (3.1) and $p = 3$ in Equation (4.1)) of the interaction as a function of particle distance. There are two consequences accompanying this difference: first, there is a change of dimensionless parameters. The general definition given in Section 3.1.1 is still valid but in contrast to Chapter 3 $p = 3$ throughout this chapter. Secondly, as mentioned above, this system can be treated in exactly the same way as before and we skip details of the numerical procedure as well as the evaluation of observables. Instead we directly continue with the presentation of the results in the next two sections.

A short comment on notation has to be made at this point. We are aware of the fact that electrons are fermions while excitons are bosonic composite particles consisting of an electron and a hole. We treat two-level subsystems in which the electron is the ground state and the exciton is the excited state. The term "particle" is used as a label for such a subsystem. In some cases where confusion may arise we will use the term (pseudo) spin instead of the term particle referring to the above-mentioned mapping between two-level systems and spin systems. Since the particles are frozen in space and thus distinguishable, at no point the statistics plays any role and the term spin or particle can safely be used.

4.1.1. Estimation of system size

In the following we will present two different calculations that show that the parameters used in our simulations are consistent with experimental conditions. This is done by estimating the system size using all other parameters of the system. The agreement of these two approximations supports the validity of our data.

First estimation

Our first estimation takes typical densities observed in experiment as a starting point. They are of the order of $10^{10}\mathrm{cm}^{-2}$, as e.g. given by Kuznetsova et al. [2012]. We therefore start with (in the two-dimensional case)

$$\frac{10^{10}}{\mathrm{cm}^{-2}} = \frac{N}{L^2}, \tag{4.2}$$

where we assume the experimental volume to be a square of edge length L. Most of our simulations were performed in the range from $N_{\mathrm{min}} = 5$ to $N_{\mathrm{max}} = 25$. Inserting these numbers in Equation (4.2) and solving for the edge length L gives

$$L = \sqrt{N} \cdot 10^{-7}\mathrm{m} \approx (2.23 - 5) \cdot 10^{-7}\mathrm{m} = (223 - 500)\mathrm{nm}. \tag{4.3}$$

So our first estimation gives values in the range of approximately 200nm to 500nm.

Second estimation

The second estimation relies on the approximate knowledge of the critical parameters. As it is shown later for a one-dimensional system we find

$$\left(\frac{Cn^3}{\Delta}\right) \approx 3. \tag{4.4}$$

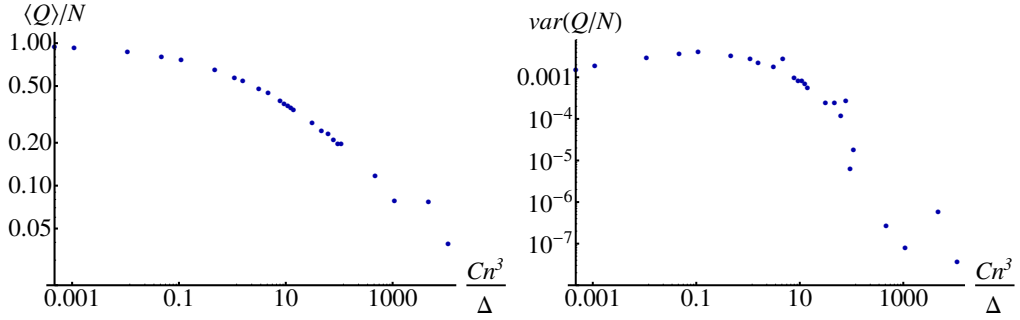

Figure 4.2: Mean (left panel) and variance (right panel) of the distribution of the number of excitons in a one-dimensional system. The data corresponds to the same data set with $\Omega/\Delta = 0.1$. Analogously to the ultracold Rydberg gas the critical parameter is estimated by fitting (not shown) and yields $Cn^3/\Delta \approx 3$ for the mean and $Cn^3/\Delta \approx 5$ for the variance.

With the aforementioned typical values and $\Delta \approx 0.01\text{eV}$ we have

$$L \approx N \sqrt[3]{\frac{e^2 d^2}{\epsilon\epsilon_0 \Delta N}} \approx N 18.3 \cdot 10^{-9}\text{m} \approx 91 - 458\text{nm}, \tag{4.5}$$

where the range corresponds to $N_{\min} = 5$ to $N_{\max} = 25$. Equation (4.3) as well as (4.5) confirm our choice of parameters to be reasonable and experimentally accessible. This fact is even supported by the large overlap of the estimated intervals of system length. We would like to point out that the values here are estimations whose only purpose is to justify the parameters used in our simulations. They shall not be used for any further calculations and we do not claim them to be correct for any specific configuration.

4.2. Estimation of critical parameters via power law method

As for the case of the ultracold Rydberg gas, mean and variance of the number of excitation can be plotted as functions of the interaction strength. A typical result is shown in Figure 4.2. Again, the data points show power law behavior in two different regimes. The critical parameter can be estimated by fitting of the power laws and subsequent determination of the intersection. In the case shown here the estimations $Cn^3/\Delta \approx 3$ for the mean and $Cn^3/\Delta \approx 5$ for the variance agree very well[1], but again it has to be noted that both values have an error which extends over roughly one order of magnitude. No values for these errors are given since their size would be an estimate as well and does not contain any further information.

In case of exciton bilayer systems two-dimensional realizations are of particular interest since these are typically utilized in experiments as well. Increasing the dimension of the system leads to a higher degree of freedom for the excitations to arrange. Therefore, in principle, larger numbers of particles

[1]Even though the two values agree very well in this case it is not entirely typical. Just as in the case of the Rydberg atom only the order of magnitude can be estimated with confidence.

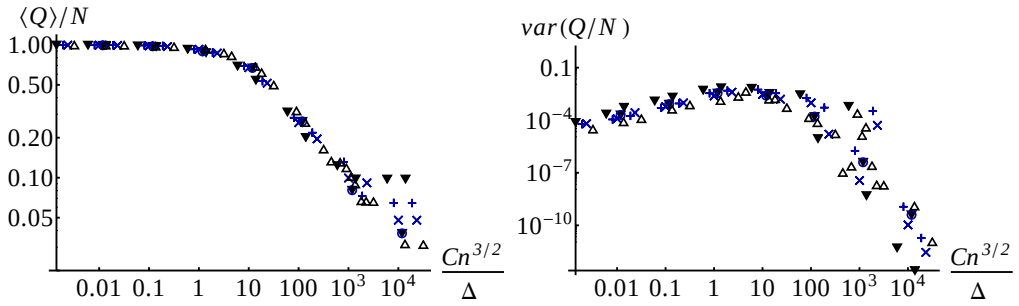

Figure 4.3: Mean (left panel) and variance (right panel) of the distribution of the number of excitons in a two-dimensional system. The different data points shown all corresponds to the same density, whereas the total number of particles is $N = 10$ (triangle pointing downwards), $N = 15$ (plus), $N = 20$ (cross), $N = 25$ (circle), $N = 30$ (triangle pointing upwards). Also, $\Omega/\Delta = 0.1$ for each data set. The estimates of the critical parameters obtained by fitting (not shown) are $Cn^{3/2}/\Delta \approx 3$ for the mean and $Cn^{3/2}/\Delta \approx 15$ for the variance.

are required to allow meaningful results for all parameter regimes. The reason for this simply is the larger surface to volume ratio. Due to the repulsive interaction the most favorable arrangement of excitons (as well as the Rydberg atoms treated in Chapter 3) is in the situation where they are far apart. Therefore, the corners of the system are typically occupied with the highest probability. In case of few particles, which corresponds to very low density, this behavior emphasizes the finite size effects of the system. To eliminate this geometric finite size effect periodic boundary conditions are used in this chapter. For the data shown here the largest number of particles is $N = 30$. The results presented in the following confirm our assumption that two-dimensional systems can reasonably be treated within this limit.

Figure 4.3 shows mean and variance of the distribution of the number of excitons in a single run in a two-dimensional system. All data points shown there are taken at the same density whereas the particle number N was varied. The agreement is, especially in the case of the mean, very good. Subsequently joining these data sets provides an additional advantage concerning the difficulties mentioned in Appendix A.8, where finite size effects in the Rydberg system are discussed. Since different numbers of particles lead to different filling fractions the steps in the mean and the peaks in the variance appear at different positions. Therefore, in the joined data set more points can be used for fitting, thus improving the quality of the result. In the present case we find the critical parameter to be $Cn^{3/2}/\Delta \approx 3$ for the mean and $Cn^{3/2}/\Delta \approx 15$ for the variance, where the result for the mean appears to be more reliable. Since no further insight will be gained by a rigorous estimation of error size we only note that they are approximately of one order of magnitude.

4.3. Correlation functions in one- and two-dimensional systems

Just as in the case of the ultracold Rydberg gas we want to use the pair correlation function as a tool to investigate spatial ordering of the excitations. In particular we are interested whether the extension of long-range order over the whole system length again can be used as an indication of a phase transition. Typical correlation functions corresponding to different interaction strengths are shown for the one-dimensional case in Figure 4.4. Again, the parameters are chosen such that

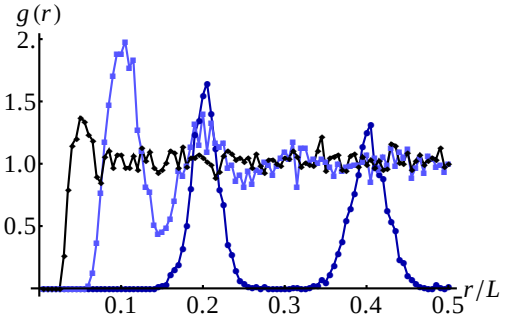

Figure 4.4: Correlation functions of an one-dimensional system. The data shown corresponds to $\Omega/\Delta = 0.1$ and $Cn^3/\Delta = 109.4$ (dark blue), $Cn^3/\Delta = 10.94$ (light blue), and $Cn^3/\Delta = 1.09$ (black). The lines between the data points only serve as a guide to the eye. Whereas the dark blue curve clearly corresponds to the crystalline phase and the black curve to the unordered phase, the light blue curve already shows distinct peaks but the correlations do not extend over the full volume. Therefore, the system is still in the unordered phase still but a slight increase of the interaction strength will lead to crystallization.

the system is in the crystalline phase for the highest and in the unordered phase for the lowest interaction strength. At the intermediate interaction strength the system appears to be in the unordered phase but already a slight increase of interaction strength will lead to crystallization.

With the help of Figure 4.4, we see that it is again possible to estimate the critical interaction strength of the system by finding the smallest interaction strength that leads to order over the full system length. From the data shown there we estimate $Cn^3/\Delta \approx 10 - 20$ as the possible range of the phase transition. Taking into account the large number of samples per curve (>10000) it appears unreasonable to generate even larger data sets to improve the estimation of the critical interaction strength.

In Figure 4.5 the behavior of the correlation function at short distances for a one-dimensional system is shown. In analogy to the case of the Rydberg gas a power law can be observed in the double logarithmic plot. Using the argumentation given in Section 3.4.1, the expected value for the exponent $\beta = 6$ is almost met by fitting the power law to the data set.

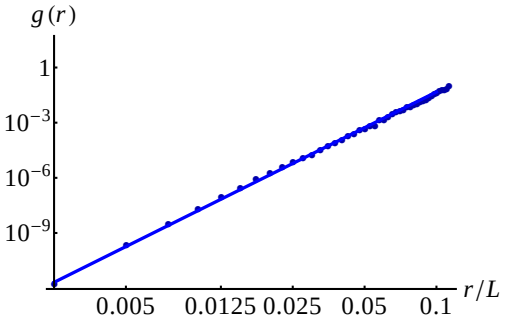

Figure 4.5: Correlation function for small distances. The double logarithmic plot corresponds to a one-dimensional system with parameters $\Omega/\Delta = 0.1$ and $Cn^3/\Delta = 5.12$. The fit of the power law (straight line) has an exponent $\beta \approx 6.46$.

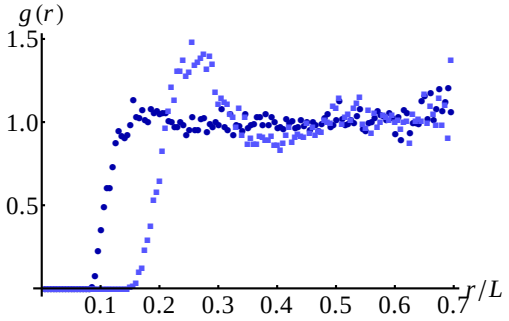

Figure 4.6: Correlation functions of a two-dimensional system. Both data sets are taken at $\Omega/\Delta = 0.1$ and differ in interaction strength $Cn^{3/2}/\Delta = 10.4$ (dark blue) and $Cn^{3/2}/\Delta = 41.6$ (light blue). Whereas the dark blue curve corresponds to the system in the unordered phase, the light blue correlation function shows long-range order up to the system length. The splitting of the secondary maximum in the light blue case is a coincidence and does not have any physical background. The fluctuations of both curves at large distances ($r/L > 0.5$) are caused by the square geometry.

Figure 4.6 shows correlation functions which differ in their respective interaction strength. While the data set corresponding to the smaller interaction strength represents a system in the unordered phase, the data set for the larger interaction strength shows order up to the system length. One may argue whether the system already is in the ordered phase or slightly below the phase transition. Both data sets, and in particular the one corresponding to higher interaction strength, show the simulation difficulties of systems of higher dimension, e.g. the increased number of degrees of freedom for each particle. A much larger number of samples is needed to significantly reduce the fluctuations which lead to the broadened peaks in the correlation function. Additionally, to observe correlation functions as in the strongest interaction case in one dimension a larger number of particles would be needed while the interaction strength would have to be kept constant to ensure a sufficiently larger number of excitations in the volume. Both improvements are in principle realizable, but are very time consuming and as mentioned above we do not expect a significant improvement of the estimation of the critical interaction strength, which is our primary goal.

4.4. Comparison of Rydberg gas and bilayer excitons

The properties of both the ultracold Rydberg gas (Chapter 3) and the excitonic bilayer system (this chapter) have been discussed in detail. They both were mapped onto spin-$1/2$ system and represented by Hamiltonians (3.1) and (4.1), which differ only in the exponent of the distance dependence in the interaction term ($p = 6$ versus $p = 3$). This common structure allowed the treatment with exact diagonalization of an effective Hamiltonian. Subsequently different statistical features of both systems were discussed which we now would like to recapitulate and compare.

In Sections 3.3.5 and 4.2, the first two cumulants of the respective probability distribution of the number of excitations were analyzed as functions of the external parameters. Both the Rydberg gas and the excitonic system exhibit different power law behavior in the limit of weak and strong interaction potential. The intersection of these power laws was used to estimate the critical interaction strength at which crystallization is expected in both cases. Also, in both cases only the order of

magnitude could be estimated. By using different particle densities and corresponding C parameters in the exciton case, we observed that this technique might aid to overcome the difficulties with finite size effects as they are discussed in Appendix A.8. This result can certainly be transferred to the case of the ultracold Rydberg gas.

The second tool to investigate the phase transition of both system is the pair correlation function which is discussed in Sections 3.4 and 4.3. In both cases the critical interaction strength can be estimated by looking for the point at which the range of order in the system reaches the system length. A quantitative determination of the order of magnitude for each system is obtained. While in the case of the Rydberg gas only one-dimensional systems are discussed, the excitonic system is treated in two dimensions as well since this geometry is preferably used in experiment. One and two-dimensional systems qualitatively share the same features, though the results for higher dimensions become harder to obtain due to the additional degrees of freedom, which requires larger numbers of particles. The correlation functions of both systems behave as a power law in the regime of small distances. The different exponent of the distance dependence of the interaction potential causes the exponent of the power law to be different for the two systems.

In summary one may conclude that the systems behave identically up to the fact of the different power law behavior in the regime of small distances. As one may have expected from the beginning, the simple change of the distance dependence of the interaction potential does not qualitatively alter the physics of the system. Also, no radical changes are observable when comparing one to two-dimensional systems. A possible reason for this is given by the fact that in any case the system is subject to long-range interactions. Therefore, the mechanism of ordering is the same even though the dimension and the distance dependence of the system is different. Qualitatively different results are expected when the type of interaction is altered, e.g. to a nearest neighbor interaction.

Chapter 5

Experimental data analysis

In this chapter we will present techniques that were developed to do post processing of experimental data. These techniques, some of which have been used to process the results by Schempp et al. [2013], are necessary since in the real experiment one faces difficulties which were not discussed in Chapter 2. They include on the one hand the effect of finite detection efficiency which has to be taken care of in any experiment and on the other hand every measured quantity is affected by the experimental parameters which are subject to drifts. These drifts are e.g. the result of thermal expansion of a component of the experimental setup, but also might be caused by external factors including vibrations of the building for example. The predictions we have made, in particular in Chapter 3, all refer to an idealized experiment in which these factors were not accounted for. We start by introducing a method to correct the statistical cumulants with respect to the effect of finite detection efficiency and afterwards present a technique which divides a continuous time series of experimental measurements into subsets in which one can assume the experimental parameters to have been stable with respect to any drift.

5.1. Finite detection efficiency

In any experiment one has to deal with finite detection efficiency. In the case of the Rydberg experiment we have in mind throughout this work, which is explained in Chapter 2, this finite detection efficiency most probably arises due to ions being caught by the field plates, ions not hitting the MCP detector or two ions arriving within the dead time. Also, we have to define a lower threshold for the signal strength from which on we count an event in the detector as a detected ion. At this point we do not want to go into detail about the origin of the finite detection efficiency but rather want to state that all of the above events can occur to any ion with equal probability and (in very good approximation) independently. Therefore, we may pool all events that lead to a missed count and define a probability of an actual Rydberg atom to be detected as such, to which we then attribute the detection efficiency η which lies in the range $0 \leq \eta \leq 1$.

At this point we would like to briefly introduce our notation for the following calculation. In every

experimental cycle there is a certain number of Rydberg atoms. This number depends on the arrangement of atoms as we have seen in the preceding chapters. The distribution of the number of Rydberg atoms Q is represented by $P(Q)$. Then a measurement is performed in each experimental cycle giving a measured value of Rydberg atoms Q' smaller than or equal to the original number of Rydberg atoms. The distribution of these measured values is denoted by $P'(Q')$. Obviously these distributions are not connected via a simple multiplication with the detection efficiency since there is a finite probability η for each Rydberg atom (or rather the ion produced from it) to be detected.

Assuming that we know this probability η of detection for each Rydberg atom in a single experimental cycle we find the measuring process to be of binomial nature. This of course crucially relies on the fact that the detection of individual ions is not correlated but independent. Therefore, the probability of the detector counting Q' Rydberg atoms is given by

$$f_\eta(Q'|Q) = \left(\begin{array}{c} Q \\ Q' \end{array} \right) \eta^{Q'} (1-\eta)^{Q-Q'} \tag{5.1}$$

when there were Q Rydberg atoms present in the experiment. This assumption is additionally justified if one considers each loss process as an individual binomial process. In the case of two successive processes with corresponding detection efficiencies η and η' the resulting probability distribution is found to be

$$\begin{aligned} P''(Q'') &= \sum_{Q=0}^{\infty} \left(\sum_{Q'=0}^{\infty} f_\eta(Q''|Q') f_{\eta'}(Q'|Q) \right) P(Q) \\ &= \sum_{Q=0}^{\infty} \left(\left(\begin{array}{c} Q \\ Q'' \end{array} \right) (\eta\eta')^{Q''} \sum_{X=0}^{\infty} \left(\begin{array}{c} Q-Q'' \\ X \end{array} \right) (\eta' - \eta'\eta)^X (1-\eta')^{Q-X-Q''} \right) P(Q) \\ &= \sum_{Q=0}^{\infty} \left(\begin{array}{c} Q \\ Q'' \end{array} \right) (\eta\eta')^{Q''} (1-\eta\eta')^{Q-Q''} P(Q), \end{aligned} \tag{5.2}$$

where we relabeled the summation index $Q' \to X + Q''$ and used the binomial theorem in the last step. Equation (5.2) shows that multiple successive binomial measuring processes can be modeled as a single binomial process in which the overall detection efficiency is given by the product of the detection efficiencies of all processes.

Now, we want to calculate the cumulants of the resulting probability distribution to connect the experimental data to what we have shown earlier in Chapter 3. The cumulants of a probability distribution are defined as

$$\langle\langle Q^n \rangle\rangle = \partial_\lambda^n \chi_Q(\lambda)|_{\lambda=0}, \tag{5.3}$$

where $\chi_Q(\lambda)$ is the cumulant generating function (CGF) which was introduced in Section 2.4.1. It is connected to the probability distribution via

$$\chi_Q(\lambda) = \ln C_Q(\lambda) = \ln\left(\langle e^{\lambda Q}\rangle\right) = \ln\left(\sum_{Q=0}^{\infty} e^{\lambda Q} P(Q)\right). \tag{5.4}$$

For a general probability distribution one finds[1]

$$\langle\langle Q'\rangle\rangle = \langle Q'\rangle = \eta\langle Q\rangle = \eta\langle\langle Q\rangle\rangle, \tag{5.5}$$

using the fact that the mean (first moment) equals the first cumulant, and

$$\langle\langle Q'^2\rangle\rangle = \eta^2\left(\langle Q^2\rangle - \langle Q\rangle^2 - \langle Q\rangle\right) + \eta\langle Q\rangle \tag{5.6}$$

for the second (variance), and

$$\begin{aligned}\langle\langle Q'^3\rangle\rangle = \eta\langle Q\rangle + 3\eta^2\left(\langle Q^2\rangle - \langle Q\rangle - \langle Q\rangle^2\right) \\ + \eta^3\left(2\langle Q\rangle - 3\langle Q^2\rangle + \langle Q^3\rangle - 3\langle Q^2\rangle\langle Q\rangle + 3\langle Q\rangle^2 + 2\langle Q\rangle^3\right)\end{aligned} \tag{5.7}$$

for the third cumulant. Since the first three cumulants of the measured distribution are given as functions of the first three cumulants of the original distribution we can invert this system of equations and obtain the original cumulants in dependence on the measured ones.

At this point we would like to remark that in order to retrieve the original cumulants we have to know the value of η. One could argue that this might not be necessary once one is able to measure two sample sets with different detection efficiencies and same parameters otherwise and then use η as a fitting parameter. But as we have seen in Equation (5.2) the subsequent evaluation of two (or more) binomial processes results in another binomial. That means that if there is any "binomial component" in the original distribution (with physical origin) this contribution could not be isolated from the effect of the detection efficiency. Consequently, all of these binomial components would be subtracted yielding a distribution from which important physical contributions are removed. It is therefore neither possible to obtain the original physical distribution by the use of the above formulas without the knowledge of the detection efficiency η nor to obtain the detection efficiency η from the data.

5.1.1. Poissonian distribution with finite detection efficiency

Because of its great importance in many statistics related problems we would like to illustrate these ideas on the example of the Poisson distribution. The probability mass function[2] of a Poissonian random process with parameter μ is given by

[1] The corresponding calculation for these expression can be found in Appendix B.1.

[2] The probability mass function is the discrete analog of the probability distribution. The two expressions will be used as synonyms.

$$P_\mu(Q) = \frac{\mu^Q}{Q!} e^{-\mu}. \tag{5.8}$$

One finds that every cumulant of this distribution evaluates to $\langle\langle Q^n \rangle\rangle = \mu$. But instead of using the formulas derived in Section 5.1 we may proceed by simply calculating the measured distribution $P'(Q')$ directly. An elementary calculation[3] shows

$$P'(Q') = P_{\eta\mu}(Q'). \tag{5.9}$$

This means that the measured probability distribution again is a Poisson distribution but now with the new parameter being the product $\eta\mu$ of the old parameter and the detection efficiency. Therefore, the cumulants of the measured probability distribution are given by $\langle\langle Q'^n \rangle\rangle = \eta\mu$.

5.2. The data sets

To begin with we want to present the data sets[4] which are are displayed in Figure 5.1. The two data sets[5], which correspond to different densities of atoms in the cloud, are displayed in the form of a histogram rather than in the actual time series in which they were taken in. This is done because much more information can be extracted from the histogram than from the time series with "the naked eye". The data sets are of unequal length because of different measurement intervals which are as long as one could be sure that there was no drastic change in the environmental parameters. In both data sets the same Rydberg state was addressed and therefore the same interaction strength is expected in both cases. Also, the laser intensity and frequency were locked to the same values. This means that the only difference between the data sets is the particle density, making the two data sets comparable. Still one has to face the unavoidable fluctuations that cause any of the parameters to change and alter the underlying probability distribution.

Figure 5.1 already suggests that the distribution of either histogram is neither Poissonian nor Gaussian. Therefore, we will do a closer investigation in the following. Before introducing the techniques for finite detection efficiency and draft correction we have to ensure the independence of each single measurement of all other measurements. This commonly is done by analyzing the auto-correlation function. It is defined (see e.g. Woyczyński [2010]) by

$$\rho_X(\tau) = \frac{\mathrm{cov}(X(t), X(t+\tau))}{\mathrm{std}(X(t))\mathrm{std}(X(t+\tau))}, \tag{5.10}$$

where cov and std stand for the covariance and standard deviation of the random process under investigation. For a a discrete time series as in our case, where measurements are taken approximately 7s apart, the assumption of a stationary process (meaning that all data points were obtained

[3] The calculation is shown in Appendix B.2.

[4] The data sets are a courtesy of Hanna Schempp, Georg Günter, Christoph Hofmann, Martin Robert-de-Saint-Vincent, Shannon Whitlock, and Matthias Weidemüller, Physics Institute, University of Heidelberg. They were previously used by Hofmann et al. [2013a] and Hofmann et al. [2013b].

[5] More information on how this data sets are obtained can be found in Appendix B.3.

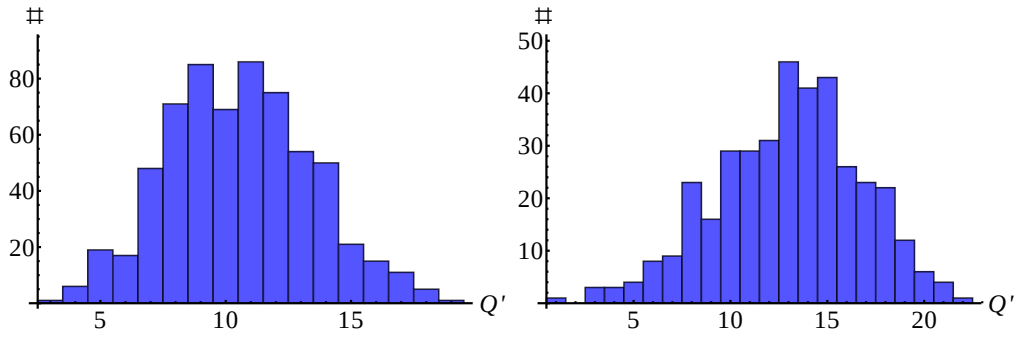

Figure 5.1: Histograms of experimentally measured data[4]. The data sets shown correspond to a high density ($6.2 \cdot 10^{11}\text{cm}^{-3}$, left panel) and a low density ($1.2 \cdot 10^{10}\text{cm}^{-3}$, right panel). The number of counts is displayed as a function of the number of measured Rydberg atoms Q' in each respective bin.

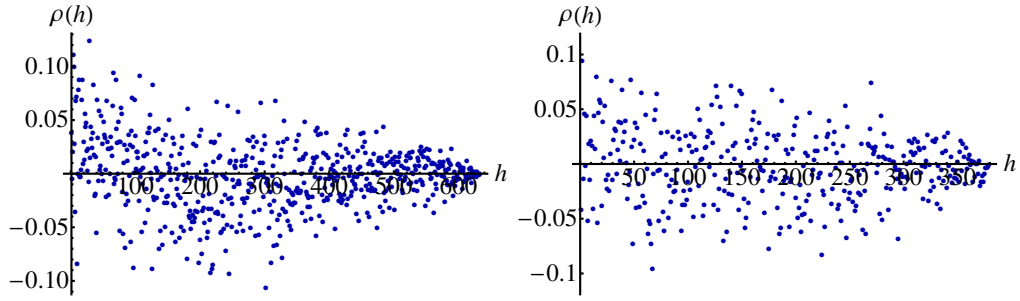

Figure 5.2: Auto-correlation function of the experimental data sets. The small values for both high (left panel) and low (right panel) density at all values for the lag h (the difference in the number of measurements) indicate that the measured values are uncorrelated and thus independent.

from the same underlying probability distribution even though the external parameters are subject to drifts) allows to express the auto-correlation function as

$$\rho(h) = \frac{\sum_{i=1}^{T-h} (Q_i - \langle Q \rangle)(Q_{i+h} - \langle Q \rangle)}{\sum_{i=1}^{T} (Q_i - \langle Q \rangle)^2}, \tag{5.11}$$

where T is the total number of measurements and Q_i the i^{th} measurement. The results of this procedure applied to the data sets introduced above are shown in Figure 5.2. For both data sets and for all lags h the relation $|\rho(h)| \ll 1$ holds true. By means of its definition the auto-correlation functions equals one for fully correlated data and minus one in case of fully anti-correlated data. In case ρ is zero there is no correlation between the data points. Since the values in Figure 5.2 fluctuate around zero and are small in magnitude we conclude that there is no correlation between the data points. Thus, we can consider them to be independent of each other.

5.3. Partitioning of experimental data time series

In this section we want to address the problem of unstable experimental conditions that e.g. arise through drifts as explained above. Our aim is to find subsets in the data given in which the parameters remained unchanged. Certainly this cannot be ensured with full confidence since the parameter change can happen on any time scale and in principle with any amplitude. By finding subsets of stable parameters we therefore mean that we try to exclude sudden changes with moderate amplitudes and continuous drifts with rather small amplitudes. Before presenting our procedure to subdivide the data sets another remark has to be made concerning the reliability of our proceeding: we are aware that we are dealing with a system subject to statistical fluctuations and therefore it might occur that we find a certain feature to be the result of a change of parameters which actually arose by statistical fluctuations with no parameter change present. This means that there is in principle no way of reproducing the original change of parameters and that we might bias the data by subdividing and merging subsets of data. Although they do not completely solve this problem permutation tests are a good tool to check whether two sets of data belong to the same distribution.

5.3.1. Partitioning algorithm

The procedure we use to subdivide the data works as follows[6]: first the number of sudden parameter changes has to be estimated. It is beneficial to overestimate this number since the procedure will accumulate the detected parameter changes at prominent positions. In the first step the data set S is divided into two subsets S_1 and S_2, where S_1 contains the first l elements of S and S_2 contains the remaining $T-l$ elements. The position l at which the set S is divided is determined by calculating

$$A_l = \sum_{j=1}^{l} (Q_j - \langle Q \rangle_1)^2 + \sum_{j=l+1}^{T} (Q_j - \langle Q \rangle_2)^2, \tag{5.12}$$

where Q_l are the elements of S and $\langle Q \rangle_i$ is the mean of subset S_i, for all possible values for l and subsequently choosing the value for l at which A_l is the smallest. In the next step the data set S is divided into three data sets S_1', S_2', and S_3'. Analogously to the first step the sum

$$A'_{l,l'} = \sum_{j=1}^{\min(l,l')} (Q_j - \langle Q \rangle_1)^2 + \sum_{j=\min(l,l')}^{\max(l,l')} (Q_j - \langle Q \rangle_2)^2 + \sum_{j=\max(l,l')}^{T} (Q_j - \langle Q \rangle_3)^2 \tag{5.13}$$

is calculated, where l is the position determined in the first step. Again, the value for l' which minimizes this expression is taken for the subdivision. In each step a new position is added to the set of detected positions of kinks $\{l, l', l'' \ldots\}$. This procedure is repeated until the desired number of subsets is reached. The routine may be stopped at the point when the positions of detected kinks start to accumulate, since in this case not parameter changes but rather statistical fluctuations are detected as break points.

[6] A commented version of the respective source code can be found in Appendix B.4.

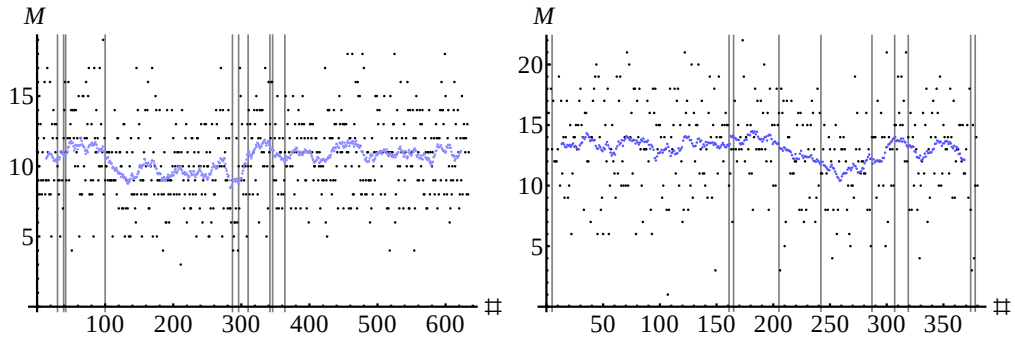

Figure 5.3: Experimental data with moving average thereof and potential parameter changes. The data points (black) are plotted in order of their measurement. A moving average over 25 points of this data (light blue) is given as a guide to the eye. The vertical gray lines indicate a parameter change detected by the routine discussed in Section 5.3.1. One finds three subsets (two in the high density case, left panel; one in the low density case, right panel) in which the parameters appear to be stable.

5.3.2. Application to experimental data sets

We apply the method discussed in the previous section to the data sets[4] introduced in Section 5.2[7]. The data time series together with a moving average over 25 data points and the detected parameter changes are shown in Figure 5.3. In both cases ten parameter changes were found. Since in both cases accumulation thereof starts there is no use in detecting more parameter changes.

We are only interested in data sets that excel a certain length since otherwise the error bars of the deduced quantities are too large. Therefore, we decide to take into account only the two longest subsets of the high density data and the longest subset of the low density data for further investigation.

dataset	high_1	high_2	low_1
interval	100-287	364-634	5-161
$\langle\langle Q' \rangle\rangle$	9.65±0.26	10.97±0.21	13.37±0.38
$\langle\langle {Q'}^2 \rangle\rangle$	7.22±0.94	7.94±0.78	14.91±2.11
$\langle\langle {Q'}^3 \rangle\rangle$	4.88±3.96	3.13±3.27	-20.40±14.69

Table 5.1: Properties of data sets. "Interval" refers to the index in the time line of measurements in the original data. The errors were obtained by bootstrapping and correspond to a 90%-confidence interval. The difference in the cumulants of the the data sets high_1 and high_2 shows that the same experimental setup can lead to different stable conditions.

Table 5.1 shows the first three cumulants of the data sets obtained by the subdivision algorithm. The errors correspond to 90%-confidence intervals obtained by bootstrapping (see e.g. Chernick [2011]). For a given set of data of length l the bootstrap procedure works as follows: a set with the same length l of data points is chosen randomly from the original data set, where any data

[7] In Appendix B.4 we show that the procedure works properly by applying it to data which was previously generated with predefined parameters changes.

point may be chosen arbitrarily many times. For this new data set the cumulants are calculated. This procedure is repeated multiple times resulting in distributions for the cumulants. From these distributions now the desired confidence intervals to level α can be computed.

Permutation test

The original idea behind dividing the original data series into subsets was to find subsets that correspond to the same set of parameters and therefore can be merged. By continuing the measurement for an arbitrarily long time one would then be able to find numerous data subsets that can be merged to finally obtain one very large subset on which cumulants and other statistical observables can be measured with high precision. This is necessary because, as we can already see in Table 5.1, the errors can be unreasonably large for small data sets. Also, the error increases for higher cumulants and one therefore has to have a large amount of data to be able to obtain a reliable result from the data.

To check whether two sets of data possibly can be merged we use the permutation test method in its simplest form (see e.g. Good [2000] for details). First the mean of each data set is computed and the absolute value of their difference is noted. Then the two data sets are merged to the full data set K. Now K is randomly permuted and cut into subsets of length of the two original data sets. The mean of each new subset is calculated and the absolute value of the difference is noted. This procedure is repeated many times and each time the difference of the resulting mean values is noted[8]. Having collected a number s of differences of means one simply calculates the percentage of trials the subsets of which have a greater difference in means than the original data sets. If this percentage is low this indicates that it is not likely that the two original data sets have the same underlying probability distribution.

In our case we only have two sets of data for which the permutation test is meaningful since a comparison of data sets corresponding to different densities is not expected to produce compatible probability distributions. The test performed on the data sets high_1 and high_2 gives a value $< 0.1\%$ as a result. This means that there is only very little chance that these data sets have the same underlying probability distribution. We remark that this result does not come unexpected since the difference in mean values of the original data set is quite large: $\delta\langle\langle Q\rangle\rangle = 1.32$.

At this point we would like to remark that one should not forget the two principal weaknesses of this approach. The first point was already mentioned briefly above and concerns the fact of merging two subsets of data in the first place. There is no proof that we do not bias the data in this way since a different mean in the two subsets might have occurred only due to statistical fluctuations even though they are samples of the same underlying probability distribution. For this reason both the case of merging two subsets that are not compatible as well as the case of refusing two subsets that are samples of the same probability distribution may occur. In addition this point of critique applies to the routine of Section 5.3.1 as well since one cannot be sure that the subsets detected represent the physical reality. The reasoning cannot be countered entirely but two facts may refute it to a large amount: first the experiment was designed in a way to maintain stable experimental conditions and the data points are taken only a few seconds apart. Therefore, it is reasonable to assume that there must be certain intervals in the data in which the conditions remained the same. This justifies the procedure of detecting parameter changes. Secondly, the subsets used each contain

[8] The procedure of recalculating a certain value for a random subsets of the full data set K resembles a Monte Carlo procedure, but the methods do not share any other common point.

a quite large amount of data and therefore the probability of failing the permutation test is small. Also, we want to remark that the permutation test does not distinctively state whether to two data sets can safely be merged but rather the probability of the two sets having the same underlying probability distribution. Now one can define a threshold from which on one is willing to take the two data sets as samples of the same probability distribution. Since there is no possibility of gaining absolute confidence one can only limit the possibility of the procedure failing by taking more and longer data sets.

The second major point is the fact that only the mean is used as a measure of whether two sets of data are compatible. One might want to extend the methods to higher cumulants as well but this is not easily realizable. This can easily be seen on the example of two samples each having a Poisson distribution as underlying probability distribution but with different parameters λ and λ'. Since this parameter equals each cumulant of the respective distribution a difference in means directly causes a difference in variances. If one would do the permutation test in the same fashion for variances of two subsets as for the means one would find unreasonable high compatibility. This simply follows from the fact the difference in means contributes to the variance of the permuted sets. Shifting one of the data sets by the difference in means is also not an option since shifting may result in a change of variance as we have seen in the case of the Poisson distribution. So one has to exactly know a priori what kind of probability distribution one is dealing with. For real experimental data this is not the case and therefore the method cannot simply be applied to the variance or any higher cumulant.

5.4. Consequences and results

We briefly want to summarize the results of the chapter and apply the formulas derived in Section 5.1 to the subsets of data detected with the algorithm introduced in Section 5.3.2. As we have seen in the previous section the permutation test only gives a small probability for the subsets to be generated by the same underlying probability distribution. Therefore, we decided not to merge the subsets. The results for the first three cumulants of these subsets were shown in Table 5.1. Applying Equations (5.5), (5.6), and (5.7) to the values within this table yields the values of the cumulants of the underlying physical probability distribution. We assume the detection efficiency η to be $\eta = 0.4$, which is typical for the experimental conditions under which the data was produced. These final results are shown in Table 5.2.

dataset	high_1	high_2	low_1
interval	100-287	364-634	5-161
$\langle\langle Q \rangle\rangle$	24.1	27.4	33.4
$\langle\langle Q^2 \rangle\rangle$	8.9	8.5	43.1
$\langle\langle Q^3 \rangle\rangle$	307	-879	-1844

Table 5.2: Cumulants of experimental data sets with applied correction for finite detection efficiency $\eta = 0.4$. No errors are given here. The values shown here are directly calculated from the ones shown in Table 5.1.

In Table 5.2 no errors are given since this does not offer any further insight. Taking the Mandel parameter as an indicator the two high density data sets correspond to a sub-Poissonian distribution

while the low density data set is super-Poissonian. But as can be seen from the third cumulant the results do not appear to be reliable. Therefore, we may not conclude whether these values are caused by the formation of an ordered structure or have different origin. We have to remark that these results are not comparable to the ones shown in Chapter 3 since no adiabatic tuning of the laser frequency was done, ergo the ground state of the system most probably was not reached. Also, the value $\eta = 0.4$ has an error itself which reduces the significance of the results. Nonetheless, the presented methods can be used to process the data of upcoming experiments and ultimately be extremely useful for detection of the phase transition we study. The validity of the algorithm was verified using generated data.

Chapter 6

Further developments

6.1. Crystal formation

In Chapter 3 we analyzed the ground state properties of the interacting Rydberg gas under the assumption of the frozen gas approximation. At this point we would like to present a method of treating atoms in motion. The system and the corresponding Hamiltonian remain unchanged, cf. Section 3.1. Instead of introducing kinetic energy to the system we proceed in a simple numerical way: we assume that once the excitation laser is switched on the system is in its many-body ground state corresponding to the present spatial arrangement of atoms. Then every atom is moved in the fashion of a random walk with variable step size leading to a new arrangement. The ground state and its corresponding energy is calculated for the new situation and compared to its earlier value. In style of a Metropolis Monte Carlo algorithm the new state may be accepted either because it is lower in energy than before or by a probability that depends on the relative difference in energies of the two states. In case the new situation is accepted the algorithm starts over with the new state and in case the new state is rejected the procedure is repeated for the initial state. The basic idea that underlies this procedure is that the forces between the Rydberg atoms lead to a motion that will minimize energy. We are aware that this procedure most likely does not mimic the actual situation in the ultracold gas cloud. But since we are neither interested in the motion of the atoms themselves nor any dynamical quantities, we believe our approach to be valid to produce results as they would be obtained after the system evolved for a certain time.

Again, we are interested in the distribution of the number of Rydberg atoms and the pair correlation function, a plot of which is shown in Figure 6.1. The curve shown here corresponds to the many-body ground state of the system after 200 accepted time steps. The most prominent feature one observes is the distinct peaks of the correlation function. A correlation function of this type directly proves the system to be in a crystalline phase. But as one can see the peaks are not equidistant for an arbitrary choice of parameters. Whereas in some situations only equidistant peaks are present, additional secondary peaks can appear for others (see right panel of Figure 6.1). This effect can be explained in the following way: the new peaks correspond to a lattice with a different lattice constant.

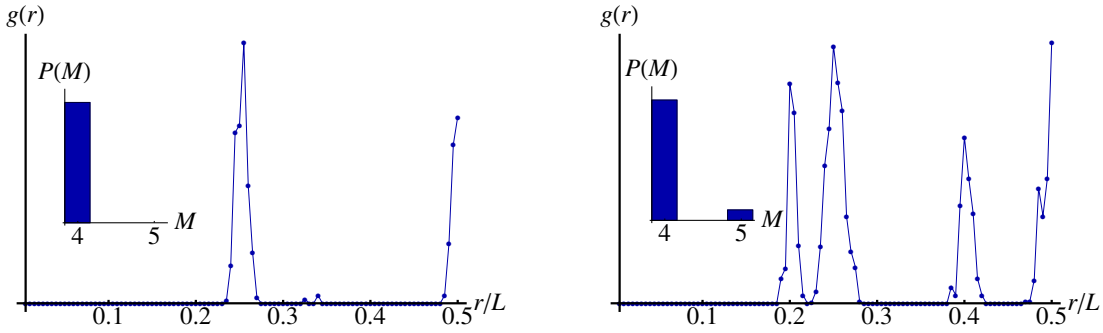

Figure 6.1: Correlation functions with respective histograms (inset). On the left ($\Omega/\Delta = 0.1$ and $Cn^6/\Delta = 3.5$) the system always approaches a crystal with the same lattice constant, while on the right ($\Omega/\Delta = 0.1$ and $Cn^6/\Delta = 13.1$) two different values for the lattice constant are possible, whereas one of them corresponds to a local minimum in the high-dimensional potential manifold. The data points are connected by straight lines to aid the eye.

As confirmed by the histograms, the different peaks correspond to ground states whose numbers of excitations differ by one. For any given set of parameters either one of the two realizations of the crystal may be lower in energy and therefore represent the (approximate) ground state of the system. Now our procedure tries to find the global minimum of the potential landscape in the high dimensional space of atom positions and their excitation configuration for a given set of parameters. At some point the procedure may reach a local minimum, which is given as a crystal with a lattice constant different from the one of the crystal at the global minimum. In principle it is possible that both states are realized in experiment as well. Unfortunately, evidence for that has not yet been seen experimentally.

The criterion which decides whether a certain arrangement is accepted even though its energy is higher than the energy of the present arrangement usually is defined via the Boltzmann factor $e^{-\beta E}$. Here, the system is assumed to be at $T = 0$ (which means that the Boltzmann factor is not meaningful) and therefore we define

$$\kappa = \frac{|E_{\text{old}} - E_{\text{new}}|}{|E_{\text{old}}|}, \tag{6.1}$$

where "old" refers to the present arrangement of atoms and "new" to the potential arrangement whose acceptance has to be decided. This parameter is computed for each time step and leads to acceptance if

$$\kappa\lambda_a < R, \tag{6.2}$$

where R is a random number in $[0, 1]$ and λ_a controls the acceptance rate. λ_a on the one hand has to be chosen such that the algorithm can escape local potential minima but on the other hand also small enough to ensure that it will "converge" on a reasonable time scale. Also, an appropriate choice for λ_a depends on the number of particles and the other system parameters. In Figure 6.2 the energy of the many-body system is plotted as a function of time steps. After some fluctuations in the very beginning the procedure continuously decreases the energy. It has been stopped after 200 time

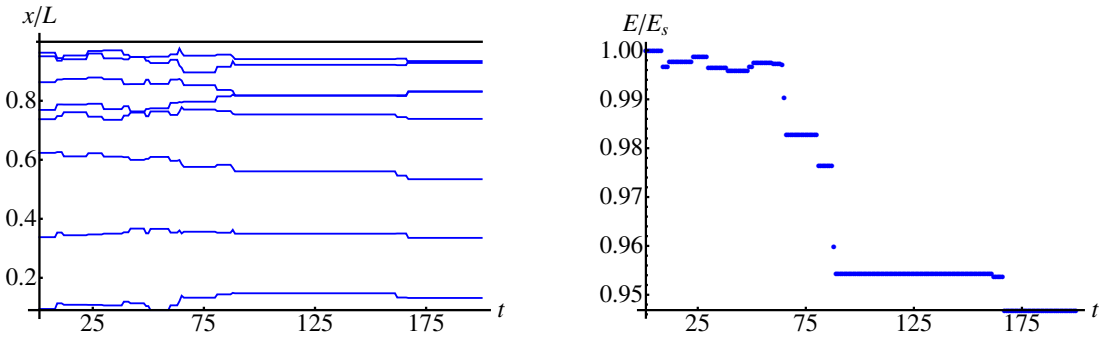

Figure 6.2: Positions of atoms (left panel) and corresponding full system energy (right panel) of a typical simulation run. In the text the atoms are referred to as counting them from top to bottom. The time t is measured in multiples of accepted steps and therefore is a bare number without units. The maximum step size is set to $L/50$, the acceptance factor $\lambda_a = 1/500$. Energy is measured in units of E_s, which is the ground state energy of the initial configuration. The parameters of the simulation are $\Omega/\Delta = 0.1$ and $Cn^6/\Delta = 13.1$.

steps since no further drastic changes are expected, which is confirmed by the atom positions also shown in Figure 6.2. While in the beginning the atoms are distributed randomly, order emerges at the end of the simulation. The lowest (referring to the scale on the left) four atoms are equidistantly spaced, indicating that they are most likely excited in the full system ground state, the uppermost two atoms are very close together and the third atom from the top is at some intermediate distance to its nearest neighbors. The ground state of such a configuration is expected to be a superposition of the states in which the lowest four atoms are excited and exclusively one of the uppermost two atoms, while the third atom from the top remains in its ground state.

The results shown here all were obtained in the regime $\Omega/\Delta \lesssim 1$. This, as we have discussed in Chapter 3, causes the ground state of a randomly arranged cloud of atoms to have an (almost) integer number of excitations. Once this relation is violated the sharp peaks in the histogram broaden and the resulting number of Rydbergs becomes truly non-integer. We expect the same to happen in this procedure, which makes the interpretation of the approach much more difficult. Still, the formation of a Rydberg crystal is expected even though the ground state is a superposition in which much more basis states contribute than in the present case, leading to a slower convergence. Simulations of this parameter regime are not performed since the results already shown are much more promising for the realization of a Rydberg crystal and therefore no new insight will be gained.

6.2. Different Rydberg states

So far the systems consisted of two-level subsystems with repulsive interaction. Now, experimentally motivated, an additional level for each subsystem is introduced. It corresponds to a Rydberg state with different principal quantum number $\tilde{n}$. Furthermore, both Rydberg states, which are coupled via a microwave field, are assumed to be of S ($l = 0$) type. The energy level scheme of this situation is depicted in Figure 6.3. In general, there are two lasers that excite atoms from their ground state $|0\rangle$ to either one of the Rydberg states $|n\rangle$ and $|\tilde{n}\rangle$. Each of them can be detuned by Δ and $\tilde{\Delta}$, respectively. Also, the microwave field may be detuned by Δ_m. The Rabi frequencies corresponding to the transitions from $|0\rangle$ to $|n\rangle$, from $|0\rangle$ to $|\tilde{n}\rangle$, and from $|n\rangle$ to $|\tilde{n}\rangle$ are denoted by Ω, $\tilde{\Omega}$, and

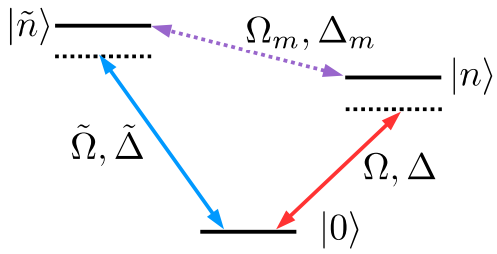

Figure 6.3: Energy level scheme including two Rydberg states. The Rydberg states are coupled to the ground states via lasers, the two-photon excitation process is implicitly assumed for both of them. An additional microwave field couples the Rydberg states. The Rabi frequency of each electromagnetic field depends on its respective intensity. Also, each field can be detuned from its respective transition frequency.

Ω_m, respectively. Analogously to the case discussed in Chapter 3 the states $|n\rangle$ and $|\tilde{n}\rangle$ interact repulsively via an interaction potential $\propto 1/r^6$. Different coefficients C and $\tilde{C}$ have to be introduced to describe the interaction between Rydberg atoms of the same state. The interaction between $|n\rangle$ and $|\tilde{n}\rangle$ is considered by introducing the interaction parameter $C_{n\tilde{n}}$.

Comparing the above model to the one investigated in Chapter 3 the tremendous increase in complexity immediately becomes apparent. Therefore, it does not seem reasonable to assume that the full system can be treated right away with the methods that have been discussed so far. We approach the problem by first assuming experimental conditions to be such that some terms in the Hamiltonian can be neglected. Then the Hamiltonian simplifies and can be treated by mean field calculations.

6.2.1. Mean field calculation for simple experimental conditions

To simplify the model discussed above, our calculations are performed in a special experimental situation. We assume only one laser to be present, setting $\tilde{\Omega} = 0$ and $\tilde{\Delta} = 0$. Also, we assume the remaining laser and the microwave field to be resonant with the respective transition frequency of atomic levels, which means that $\Delta = 0$ and $\Delta_m = 0$. It is reasonable to assume that these conditions can easily be created in experiment, possibly even simpler than a situation in which each parameter has to be controlled with high precision. Additionally to these assumptions we apply an approximation: we assume interaction only to be present for each Rydberg state separately but no interaction between the different Rydberg states, meaning $C_{n\tilde{n}} = 0$. If one assumes the principal quantum numbers of the two considered Rydberg states to be different by a large amount, $|n - \tilde{n}| \gg 1$, the properties of the Rydberg states are much different as has been shown in Chapter 2. The interaction strength in particular can be different by orders of magnitude due to the difference in magnitude of the respective dipole matrix elements. Therefore, we expect interactions between Rydberg atoms of the same state to be dominant compared to those between Rydberg atoms of different states.

Using all of the above assumptions and the approximation the Hamiltonian of the system can be written down in analogy to the one presented in Section 3.1. It reads

$$\mathcal{H} = \frac{\Omega}{2}\sum_{i=1}^{N}\sigma_x^i + \frac{\Omega_m}{2}\sum_{i=1}^{N}\tilde{\sigma}_x^i + C\sum_{i\neq j}^{N}\frac{P_iP_j}{r_{ij}^6} + \tilde{C}\sum_{i\neq j}^{N}\frac{Q_iQ_j}{r_{ij}^6}, \tag{6.3}$$

where the tilde at $\tilde{\sigma}$ indicates a Pauli matrix between the two Rydberg states. To simplify notation the symbols P_i and Q_i were introduced. They are the operators that project the state of atom i on either of the two Rydberg states. Representing the state of a single atom by a vector in which the first entry corresponds to the Rydberg state that is laser-coupled to the ground state, the second one to the other Rydberg state, and the third one to the atomic ground state these operators have the form

$$\sigma_x = \begin{pmatrix}0&0&1\\0&0&0\\1&0&0\end{pmatrix}, \quad \tilde{\sigma}_x = \begin{pmatrix}0&1&0\\1&0&0\\0&0&0\end{pmatrix}, \quad P = \begin{pmatrix}1&0&0\\0&0&0\\0&0&0\end{pmatrix} \quad \text{and} \quad Q = \begin{pmatrix}0&0&0\\0&1&0\\0&0&0\end{pmatrix}, \tag{6.4}$$

where we omitted the index corresponding to the atom. The projection operators can be expressed by the $\sigma/\tilde{\sigma}$-matrices in the following way:

$$P = \frac{1}{3}(\mathbb{1} + \sigma_z + \tilde{\sigma}_z) \qquad \text{and} \qquad Q = \frac{1}{3}(\mathbb{1} - 2\tilde{\sigma}_z + \sigma_z), \tag{6.5}$$

where again we dropped the atom index. From this point on we are going to work along the lines of Weimer et al. [2008] (c.f. Weimer [2010]). First, we assume the pair correlation function for both Rydberg states to be of the form

$$g(r) = \Theta(r - a), \tag{6.6}$$

where a is a parameter that can (and should) be different for each Rydberg state and therefore carry an index which is dropped here. This assumption explicitly accounts for the effect of the blockade radius, which has been discussed before. Still, it is not compatible with what one would expect for hard spheres (c.f. Section 3.5.2), but matches the situation of hard spheres in the limit of vanishing density. Now the mean field approximation is used in expanding the projection operators and neglecting the correlations between them. Together with the assumption of the correlation function one arrives at

$$\begin{aligned} P_iP_j &= \left(P_i\langle P_j\rangle + P_j\langle P_i\rangle - \langle P_i\rangle\langle P_j\rangle\right) g_n(r_i - r_j),\\ Q_iQ_j &= \left(Q_i\langle Q_j\rangle + Q_j\langle Q_i\rangle - \langle Q_i\rangle\langle Q_j\rangle\right) g_{\tilde{n}}(r_i - r_j). \end{aligned} \tag{6.7}$$

These expressions are now inserted into Equation (6.3). Denoting the expectation values $\langle P_i\rangle$ and $\langle Q_i\rangle$ by f_n and $f_{\tilde{n}}$, respectively, simplifies the interaction terms to give

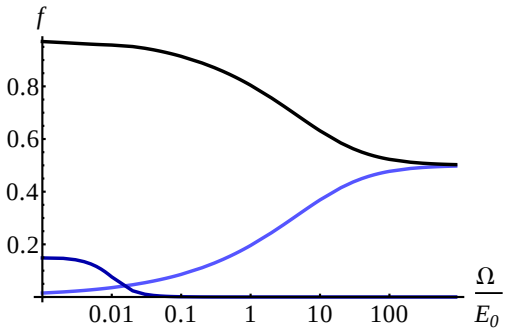

Figure 6.4: Occupation of the three states. The light blue curve corresponds to the laser-coupled Rydberg state, the black curve to the ground state and the dark blue curve (which is scaled by a factor of 10 to make its functional dependence visible) to the other Rydberg state. The parameters are $\Omega_m/E_0 = 0.7$ and $C/\tilde{C} = 10$.

$$\mathcal{H} = \frac{\Omega}{2}\sum_i \sigma_x^i + \frac{\Omega_m}{2}\sum_i \tilde{\sigma}_x^i + C\sum_{i\neq j}\frac{2P_i f_n - f_n^2}{r_{ij}^6} + \tilde{C}\sum_{i\neq j}\frac{2Q_i f_{\tilde{n}} - f_{\tilde{n}}^2}{r_{ij}^6}. \tag{6.8}$$

All terms are independent of the summation index j. Executing this sum leaves us with the Hamiltonian being given as the sum over single particle Hamiltonians. To this end, the summation is replaced by an integration,

$$\sum \to n\int \mathrm{d}V, \tag{6.9}$$

where n is the particle density[1] and V is the considered volume, which we here assume to have three dimensions (and to be arbitrarily large). The calculation can be performed for any other choice of dimension in the exact same way. It is not shown here since no further insight can be gained. The single particle Hamiltonian resulting from the integration reads

$$\mathcal{H}^{(i)} \approx \frac{\Omega}{2}\sigma_x^i + \frac{\Omega_m}{2}\tilde{\sigma}_x^i + Cn(2P_i f_n - f_n^2)\frac{4\pi}{3a_n^3} + \tilde{C}n(2Q_i f_{\tilde{n}} - f_{\tilde{n}}^2)\frac{4\pi}{3a_{\tilde{n}}^3}. \tag{6.10}$$

Now, to make this expression independent of the parameter a, which has been introduced by hand, the relation

$$nf\int \mathrm{d}V(1 - g(r)) = 1 \tag{6.11}$$

is used. It holds true for both Rydberg states individually[2] and yields $a = (3/4\pi f n)^{1/3}$, where

[1] Even though one of the Rydberg states is labeled $|n\rangle$ we believe that there is no danger of confusion between this state and the particle density n.

[2] The fact that the normalization is given by Equation (6.11) for each Rydberg state individually strongly relies on our assumption of absent interaction between the different Rydberg states.

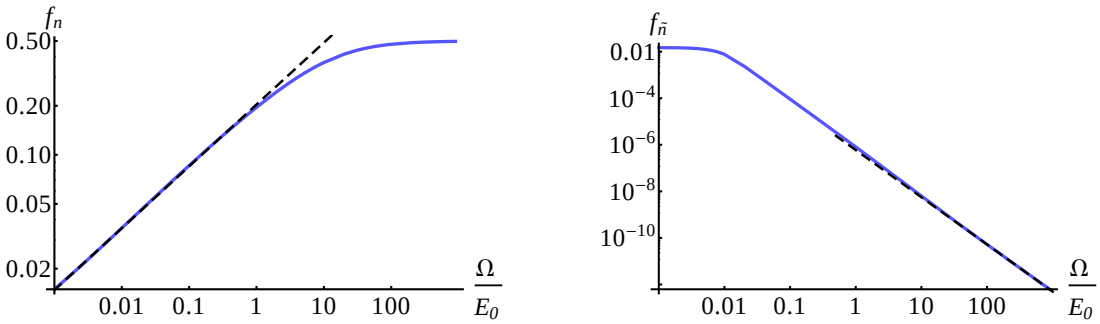

Figure 6.5: Excited fractions of laser-coupled (left panel) and other Rydberg state (right panel). Both curves are shown as a double logarithmic plot to display the power law character. The black dashed lines correspond to power law fits. The data is the same as shown in Figure 6.4.

f and a carry the same index, which again has been omitted. The final expression of the single particle Hamiltonian is then given by

$$\mathcal{H}^{(i)} \approx \frac{\Omega}{2}\sigma_x^i + \frac{\Omega_m}{2}\tilde{\sigma}_x^i + Cn^2 f_1(2P_i f_n - f_n^2) + \tilde{C}n^2 f_2(2Q_i f_{\tilde{n}} - f_{\tilde{n}}^2). \tag{6.12}$$

From this equation we now can compute the observables like the excited fraction of either of the two Rydberg states. Before continuing we would like to rewrite the Hamiltonian as a matrix corresponding to the above-mentioned state vectors. At the same time we would like to introduce dimensionless constants to be able to compare the results to other approaches and experiment. We define the energy scale $E_0 = \tilde{C}n^2$ and the parameters $\alpha = \Omega/E_0$, $\alpha_m = \Omega_m/E_0$ and $\hat{C} = C/\tilde{C}$. With these definitions the Hamiltonian is given by

$$\frac{\mathcal{H}^{(i)}}{E_0} \approx \begin{pmatrix} 2\hat{C}f_n^2 & \alpha_m & \alpha \\ \alpha_m & 2f_{\tilde{n}}^2 & 0 \\ \alpha & 0 & 0 \end{pmatrix} - \mathbb{1}(\hat{C}f_n^3 + f_{\tilde{n}}^3). \tag{6.13}$$

There are two possible choices of states which can be used to evaluate the observables. Since it is not relevant for the scaling laws that we are about to calculate, whether one chooses the "stationary state" or the ground state (cf. Weimer et al. [2008]), we choose the ground state for convenience. The ground state $|\mathrm{GS}\rangle$ of the single particle system with Hamiltonian (6.13) can be obtained via diagonalization and is then used in the evaluation of

$$f_n = \langle \mathrm{GS}|P|\mathrm{GS}\rangle \qquad \text{and} \qquad f_{\tilde{n}} = \langle \mathrm{GS}|Q|\mathrm{GS}\rangle, \tag{6.14}$$

where we dropped the atom index since the expectation value has to be the same for every atom in mean field approximation. The two Equations (6.14) are coupled since the right hand side of either equation is a function of both f_n and $f_{\tilde{n}}$. We solve the problem numerically. The resulting occupations of each state are shown in Figure 6.4 as a function of α. In Figure 6.5 the occupation

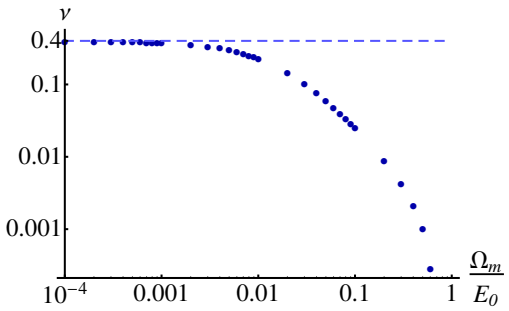

Figure 6.6: Scaling exponent in dependence on microwave Rabi frequency Ω_m. The data points result from fitting power laws to curves as the ones shown in Figure 6.5 with $C/\tilde{C} = 10$. The dashed line shows the limit of a two-level system and corresponds to $\nu = 2/5$ as shown by Weimer et al. [2008].

of the two Rydberg states is displayed separately in a double logarithmic plot. Here, the power law character of both curves becomes obvious.

To show that the present results are compatible with existing work we analyze the system in the limit of vanishing microwave Rabi frequency Ω_m. In this limit one of the Rydberg states decouples from the rest of the system resulting in an effective two-level system, which resembles the one treated by Weimer et al. [2008]. One of the central results of this work is the scaling exponent ν, which is found to be $2/5$ in the three dimensional case. ν is defined as the exponent of the asymptotic power law of the excited fraction of Rydberg atoms in dependence on the parameter α, which is proportional to the Rabi frequency Ω. Here we proceed by fitting a power law to the data points of f_n as a function of Ω/E_0, a sample of which is shown in Figure 6.5. Each time the exponent ν is noted and finally plotted as a function of the microwave Rabi frequency Ω_m in Figure 6.6. It becomes evident that the above-stated expectation for the exponent ν, which is indicated as a dashed line, is met in the limit of small Ω_m.

A remarkable feature is the behavior of the excited fraction $f_{\tilde{n}}$ of the microwave-coupled Rydberg state. As can be seen in Figure 6.5 it displays power law behavior as a function of Ω_m/E_0 in a wide parameter range. The corresponding exponent will be labeled $\nu_{\tilde{n}}$ and can be obtained by a fitting procedure. The result of this procedure is quite universal, giving $\nu_{\tilde{n}} \approx -2$ independent of the choice of parameters of the system. This feature may possibly be used as a benchmark of whether the present model resembles experimental conditions or whether other approaches have to be used.

In his work Weimer [2010] uses the existence of the exponent ν as a proof of a quantum phase transition. Whereas in general it is true that power law behavior is an indication of a phase transition we want proceed very carefully at this point and briefly list some points that have to be taken into account when considering the results presented here. First of all, one has to mention that the assumption of the correlation function (6.6) and the normalization condition (6.11) are not fully compatible. Still, one can argue that this assumption is a good approximation that will not alter results critically. But in addition, the normalization condition (6.11) has to be fulfilled separately by both Rydberg states. This can only be accomplished when the different types of Rydberg atoms do not interact with each other, which hardly can be justified for arbitrary Rydberg states. Therefore, it is debatable whether this approximation is controlled. Another point of critique is that – already in the two-level system – no fluctuations are present as in all mean field calculations. As a consequence no comparison to the results of Chapter 3 can be done.

6.2.2. Rearrangement of Rydberg atoms in different states

In this section the following experimental situation is treated: as previously introduced in Chapter 2 a cloud of atoms is trapped and subsequently cooled. Then the system is irradiated by laser light (single- or two-photon excitation) of two lasers which are tuned to different Rydberg states of a single atom for a finite period after which the lasers are switched off again. Having performed the illumination process non-adiabatically the system then is in a quasi-stationary state. In this state excitations of both Rydberg states are present but they are possibly not arranged in the energetically most favorable way. Now, instead of the well-known van der Waals interaction (see Chapter 3) energy can be transferred from one atom to another. For this energy transfer it is required that one of the atoms is in the first and the other atom is in the second Rydberg state. Then energy can be transferred by exchanging the states of the atoms. An additional laser may be switched on which couples the one to the other Rydberg state.

A short comment has to be made why the van der Waals interaction is not accounted for in our model. This can be explained in the following way: by using the frozen gas approximation we assume all atoms to be fixed in space. That means, that if a pair of atoms exchanges their Rydberg states their interaction energy will not be altered. Still, one has to consider that once the Rydberg state has been exchanged the neighborhood of the Rydberg atoms changed. Therefore, the interaction energy of the surrounding atoms – or potentially all Rydberg atoms in the sample – would have to be taken into account. In case the Rydberg states are very similar, meaning that the difference in principal quantum number is small and both are zero angular momentum states, the difference in interaction energy is expected to be negligible as compared to our new type of interaction. The fact that the van der Waals interaction has a $1/r^6$ dependence whereas the new interaction depends on distance as $1/r^3$ additionally supports this argument since if the mean distance between particles is large enough the interaction will always be dominated by the $1/r^3$ contribution. For this line of reasoning it is essential that no Rydberg atom can be deexcited to the electronic ground state but remains in either of the two Rydberg states.

To model this situation we start at the point at which the lasers are switched off and the system is in the quasi-stationary state. All atoms that have not been excited to any of the two Rydberg states and remained in their respective ground state can be neglected and the system reduces so that it can be described by a model consisting of two-level subsystems. In these subsystems each of the two Rydberg states corresponds to one of the levels. Analogously to the model used in Chapter 3 these two-level subsystems are represented as spin-$1/2$ particles. In the stationary state reached after excitation these spins are distributed uniformly in the experimental volume. Again, we use the frozen gas approximation which assumes the atoms not to move within the experimental relevant time scales. The energy transfer between two of these spins is modeled by the process $|\uparrow\downarrow\rangle \leftrightarrow |\downarrow\uparrow\rangle$, which is closely related to the effect of Förster resonant energy transfer (see Förster [1948][3]). We assume the energy transfer to be of dipole-dipole type and to depend on distance $\propto 1/r^3$. The additional laser mentioned above again is introduced to the system in the RWA, which neglects all high frequency terms since their average is expected to be zero. The two relevant parameters, as in the cases treated before, are the detuning Δ from the transition frequency between the atomic levels and the Rabi frequency, which depends on the intensity. The model Hamiltonian under these assumptions reads

[3]This effect manifests itself e.g. in photosynthesis and is used in bio-chemistry as a tool to measure distances. No further details will be given since this is out of the focus of this work.

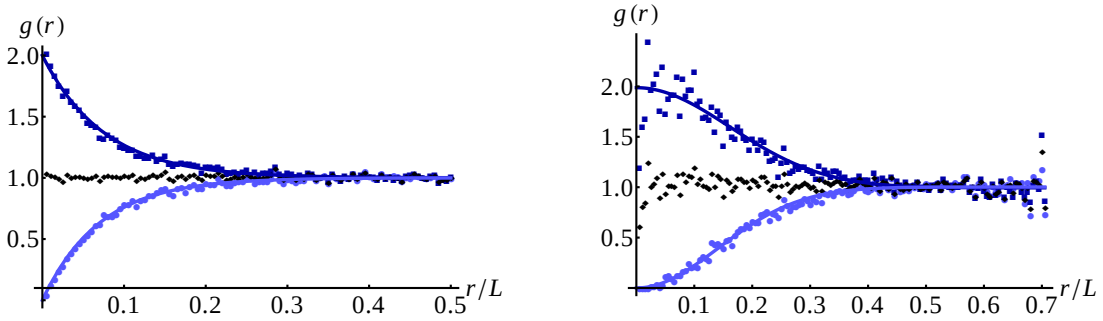

Figure 6.7: Correlation functions in case of no coupling between the Rydberg states in one dimension (left panel) and two dimensions (right panel). The curves correspond to $g_{\uparrow\uparrow}(r)$ (bright blue) and $g_{\uparrow\downarrow}(r)$ (dark blue). The constant (black) is the sum of the two correlation functions and used as a check. The fitting parameters are given as $r_0/L = 0.070$ ($\uparrow\uparrow$) and $r_0/L = 0.076$ ($\uparrow\downarrow$) for the 1D case and $r_0/L = 0.2$ ($\uparrow\uparrow$) and $r_0/L = 0.23$ ($\uparrow\downarrow$) for 2D. The parameters of the simulation are $N = 7$ and $L = 10$ for 1D and 2D.

$$\mathcal{H} = -\frac{\Delta}{2}\sum_{i=1}^{N}\sigma_z^i + \frac{\Omega}{2}\sum_{i=1}^{N}\sigma_x^i + C\sum_{i=1}^{N}\sum_{j=i}^{N}\frac{\sigma_+^i\sigma_-^j + \sigma_-^i\sigma_+^j}{r_{ij}^3}, \tag{6.15}$$

where C labels the strength of the interaction leading to the energy transfer. The operators σ_+ and σ_- are defined via

$$\sigma_\pm = \sigma_x \pm i\sigma_y. \tag{6.16}$$

While σ_+ applied to a spin down state returns a spin up state, σ_- does the opposite. Therefore, the sum of the products of these two operators with interchanged atom indices exchanges the states of spin between a spin up and a spin down atom.

Laser switched off

The simplest case is the situation in which Ω and Δ are set to zero. This means that the excitation laser is switched off once a state is reached in which both types of Rydberg atoms are present and the two Rydberg states are not coupled with an additional laser.. In Figure 6.7 two correlation functions corresponding to this situation are shown. The plots display the correlation function that measures the correlation of Rydberg atoms of the same kind $g_{\uparrow\uparrow}(r)$ and of different kind $g_{\uparrow\downarrow}(r)$. Since the atoms were initially distributed uniformly, we can check whether the sum of the two correlation functions is a constant as a function of distance r, which is also confirmed in Figure 6.7. The correlation function can be modeled by the functions

$$f_{\uparrow\uparrow}(r;\{r_0\}) = 1 - e^{-\left(\frac{r}{r_0}\right)^d} \qquad \text{and} \qquad f_{\uparrow\downarrow}(r;\{r_0\}) = 1 + e^{-\left(\frac{r}{r_0}\right)^d}, \tag{6.17}$$

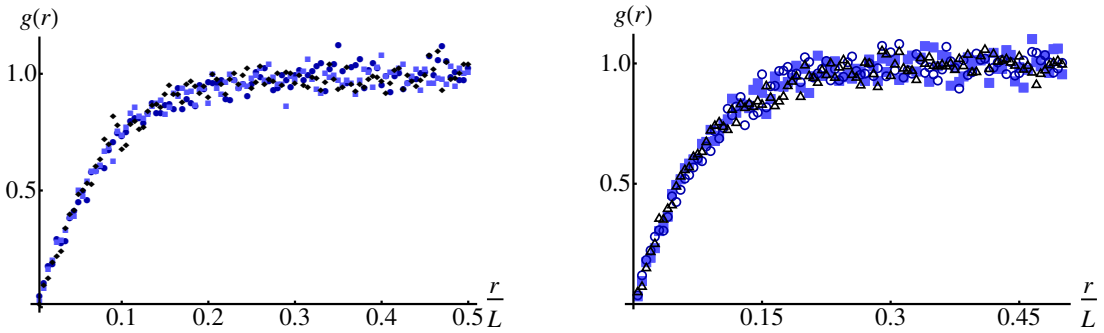

Figure 6.8: Correlation function $g_{\uparrow\uparrow}(r)$ for different types of interaction (left panel) and for different interaction strength (right panel). The coincidence of the curves, which correspond to $p = 3$ (dark blue), $p = 7$ (light blue), and $p = 11$ (black) for the same magnitude of C, shows that the numerical value of the exponent of the power law has no effect on the correlation function (left panel). The correlation function has no dependence on the interaction strength as well (right panel). These facts support the conjecture that this universal behavior is of geometric or statistical origin.

where r_0 is a parameter used to fit these functions to the data points and d is the dimension of the system under consideration.

Interestingly, the behavior of the correlation functions does not change in the case when the exponent p of the interaction is altered, see Figure 6.8. Also, the magnitude of the interaction strength does not play a role simply because there is no other energy scale in the system which it can be compared to. This can be deduced directly from the Hamiltonian in which every non-zero entry is proportional to the interaction strength and therefore it may be used as a unit. These facts lead to the reasonable conjecture that the functional dependence of the correlation functions is solely caused by geometric and/or statistical effects. This idea is supported by the similarity of the correlation function to the probability to find no point within a certain distance around a fixed point in a set of uniformly distributed random points (see Kendall and Moran [1963] or Moltchanov [2012]).

Additionally, we investigated the effect of density on the correlation function. The results are shown in Figure 6.9. Both particle number and system length were varied separately to ensure that density dependent effects could be observed. The observed behavior confirms the above stated idea of the functional dependence of the correlation function solely being caused by statistical and/or geometric effects.

Laser switched on

In this case the parameters Δ and Ω are finite and dimensionless as introduced in Section 3.1.1, leading to a coupling between the different Rydberg states. This generates a new energy scale which leads to a new effect that manifests itself in the correlation function $g_{\uparrow\uparrow}(r)$ of the system which is shown in Figure 6.10 for different interactions. On top of the behavior that has been discussed in the previous section, the correlation function now exhibits an additional shoulder whose position depends on the system parameters. The mere existence of a new feature can be explained by the fact that the Hamiltonian (6.15) is not symmetric with respect to the exchange of spin up and spin

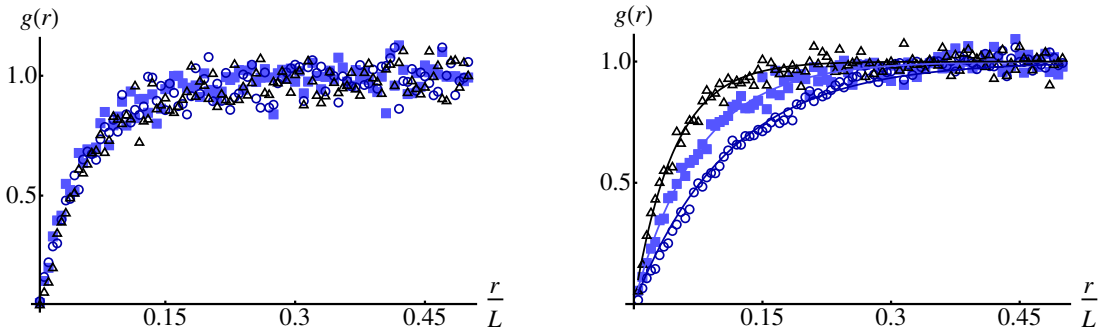

Figure 6.9: Correlation function $g_{\uparrow\uparrow}(r)$ for different densities. Both system length (left panel) and particle number (right panel) are independently varied to confirm the system's dependence on density, while all other parameters are kept constant. When comparing the two panels one has to take into account that a different system length also affects the abscissa of the plots. One finds the plots to be compatible.

down, which is in contrast to the situation of $\Delta = 0$ and $\Omega = 0$.

As can be seen from Figure 6.10 directly, the position of the shoulder is a function of interaction strength. For small distances the interaction term is dominant and therefore the correlation function shows the same behavior as in the case where the excitation laser is switched off, which is discussed in the previous section. For large distances the behavior of the correlation function is dominated by the laser terms of the Hamiltonian (6.15). Since these terms are not distance dependent one finds the observed constant in this regime to be reasonable. These regimes are separated by a crossover at which the terms of the Hamiltonian are of equal magnitude and a steep shoulder can be observed in the correlation function.

To confirm the above-made statements the position of the shoulder R_s is plotted in dependence on the interaction strength in Figure 6.11. The function

$$h(r; \{\alpha, \beta\}) = \alpha x^{\beta} \tag{6.18}$$

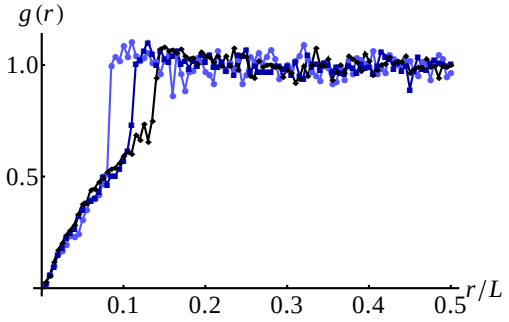

Figure 6.10: Correlation function $g_{\uparrow\uparrow}(r)$. Finite detuning and Rabi frequency lead to an additional feature that does not appear in the situation discussed in the preceding section. The position of the shoulder depends on the parameters, which in this case are given by $\Omega/\Delta = 0.005$ and $Cn^6/\Delta = 0.108, 0.27, 0.54$ for the bright blue, dark blue, and black curve, respectively. The data points are joined only as a guide to the eye.

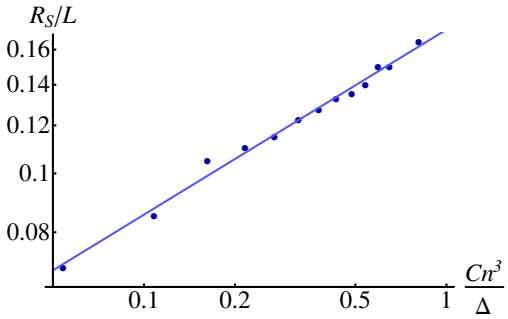

Figure 6.11: Crossover distance in dependence on interaction strength. The light blue solid line is a power law fit to the dark blue data points. The data shown corresponds to $\Omega/\Delta = 0.005$

is used to fit the data points. The fit yields $\beta = 0.31 \approx 1/3$. Estimating the crossover by equating a constant (with respect to distance) for the first two terms of the Hamiltonian (6.15) with a term that depends on distance as $1/r^3$, like the third term of the Hamiltonian, and solving for r makes this result appear to be reasonable.

6.3. Rydberg clusters

So far, we always treated ground state properties and assumed that this state is reached adiabatically. Now, if no chirped laser pulse is applied, as explained in Section 2.2.1, this assumption of adiabatic transfer to the ground state is not valid any more. Therefore, we want to address the question of what happens in the excitation process in the situation where the excitation laser has a finite and constant detuning Δ during the pulse. In addition we are interested in the features of the resulting probability distribution. The idea of our treatment, which will be explained in the remainder of this section, is based on is the following: assume a system consisting of a single atom that interacts with a light field that is detuned by a large amount from the transition frequency between the atomic levels. The broadening of the atomic levels only leads to an exponentially small probability of exciting the atom to the desired Rydberg state. If a second atom is included in the system there is a finite contribution to the total energy of the system if both atoms are in the Rydberg state. This interaction energy depends on distance as explained earlier. At a certain distance the interaction energy therefore exactly compensates for the finite detuning of the laser, so that the transition from both atoms being in their respective ground state to the doubly excited state becomes resonant. In this case the probability of a simultaneous excitation of the pair of atoms is expected to be larger than the probability of exciting either of the atoms independently[4]. For an arbitrary distance between the atoms each atom has a finite probability to be singly excited and a probability to be excited as a member of a pair, where the latter depends on this distance.

The same reasoning can be applied to clusters, where a cluster is what we call an ensemble of atoms that may be resonantly excited, of more than two atoms for the situation of even larger detuning. One may argue that any finite detuning can be compensated for by the interaction energy at particular distance between the atoms, but for a large detuning this distance has to be

[4]In a rigorous treatment one would have to take into account the fact that a two-photon process is much less likely than a single-photon process. This effect is not discussed since it is not included in our model.

very small. If we now consider an atomic gas cloud we have to find a pair of atoms that are at approximately this particular distance to allow resonant excitation. Once the distance between the atoms has to be much smaller than the average particle distance in the gas cloud, there is very little chance of finding a pair of atoms that matches the resonance condition. That means that for a certain detuning the excitation of three-atom Rydberg clusters can be larger than the probability to excite two-atom clusters, even though this probability is not negligible.

The simplest situation is the one of a one-dimensional excitation volume. In any higher dimension the possibility of arranging atoms differently while keeping their distance to the nearest neighbor constant will possibly smear out any effects that can be observed due to the above-mentioned criterion. Even though our model does not include the effects of spatial arrangements we expect its features to be confirmed (or rejected) most easily in (quasi) one-dimensional systems.

The system consists of N atoms, each of which can be excited to the Rydberg state either by itself or as a member of a cluster. The maximum size of a cluster m can be chosen by hand. It is assumed that the atoms are distributed uniformly in the excitation volume leading to the approximation that the probability of exciting an atom as a member of any cluster of size k is equal for each atom. That means that there are probabilities $p_1, p_2, p_3, \ldots$ to excite each atom individually, as a member of a pair or as a member of a cluster of size three and so on. In experiment these probabilities are functions of the detuning Δ, but to demonstrate and explain the most important features it is sufficient to investigate the behavior of the model by manually defined values of the p_i.

The above assumptions lead to a multinomial distribution. Out of N atoms it defines the probabilities of finding n_0 ground state atoms, n_1 individually excited atoms and n_i atoms excited as members of a cluster of size i as

$$P_{\text{mult}}(n_0, n_1, \ldots, p_m) = \begin{cases} \binom{N}{n_0, n_1, \ldots, n_m} p_0^{n_0} p_1^{n_1} \cdots p_m^{n_m} & \text{if} \quad N = n_0 + n_1 + \ldots n_m \\ 0 & \text{otherwise.} \end{cases} \tag{6.19}$$

Here, the probability to find an atom in its ground state is given by $p_0 = 1 - p_1 - p_2 - \ldots p_m$ and m is the maximum cluster size. The multinomial coefficient in Equation (6.19) is defined as

$$\binom{N}{n_0, n_1, \ldots, n_m} = \frac{N!}{n_0! n_1! \ldots n_m!}. \tag{6.20}$$

Since the Rydberg atoms are excited as a member of a cluster of a certain size not all occupation numbers $n_0, n_1, \ldots$ are allowed. We have to restrict the probabilities in Equation (6.19) to the cases in which n_2 is divisible by two, n_3 is divisible by three and so on. The probabilities then read

$$P_{\text{ryd}}(n_0, n_1, \ldots, p_m) = 1/Z \begin{cases} \binom{N}{n_0, n_1, \ldots, n_m} p_0^{n_0} p_1^{n_1} \cdots p_m^{n_m} & \text{if} \quad N = n_0 + n_1 + \ldots n_m \quad \text{and} \\ & \qquad \text{Mod}(n_i, i) = 0 \\ 0 & \text{otherwise,} \end{cases} \tag{6.21}$$

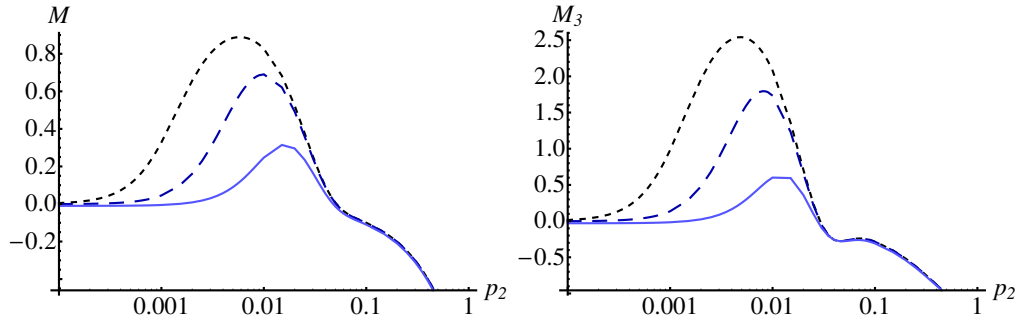

Figure 6.12: Mandel parameters M (left panel) and M_3 (right panel) as function of p_2. The size of clusters is limited by $m = 2$. The curves correspond to systems with $p_1 = 0.0001$ (black, short dashed), $p_1 = 0.001$ (dark blue, long dashed) and $p_1 = 0.01$ (light blue), all containing 50 atoms. In a wide range both M and M_3 have positive values, indicating super-Poissonian statistics. For larger values of p_2 both become negative, indicating sub-Poissonian statistics.

where the normalization is the total of all "probabilities", which is given by

$$Z = \sum_{n_0=0}^{N} \sum_{n_1=0}^{N} \cdots \sum_{n_m=0}^{N} \begin{cases} \binom{N}{n_0, n_1, \ldots, n_m} p_0^{n_0} p_1^{n_1} \cdots p_m^{n_m} & \text{if} \quad \begin{array}{c} N = n_0 + n_1 + \ldots n_m \quad \text{and} \\ \text{Mod}(n_i, i) = 0 \end{array} \\ 0 & \text{otherwise.} \end{cases} \tag{6.22}$$

Figures 6.12 and 6.13 show the Mandel parameter M and its third cumulant equivalent M_3 (see Equation (2.31)) for the case of a maximum cluster size $m = 2$ and $m = 3$, respectively. They are plotted as functions of the probability of the largest possible cluster p_m. In both situations ($m = 2$ and $m = 3$) M as well as M_3 are positive in a certain regime. As long as the probability to excite single atoms p_1 is larger than all other p_i in the system M and M_3 are (almost) zero, indicating purely Poissonian statistics. If one of the p_i is larger than p_1 but still small, the limit of both M and M_3 is non-zero as can be seen in the dark blue curve in Figure 6.13. A common feature shared by all curves is the maximum whose position as a function of p_m depends on all other p_i.

We see that the model shows super- as well as sub-Poissonian statistics in certain regimes of the parameter space. This is a profound difference to modeling the system by Poissonian or binomial statistics. In the former case both M and M_3 are identically zero, while in the latter case $M = -p$ and $M_3 = 2p^2 - 3p$, where p is the probability parameter of the binomial distribution. Since $p \in [0, 1]$, M and M_3 are always negative. Therefore, a super-Poissonian distribution cannot be explained by either of these two simple models. This makes the new model a valuable tool that reveals the formation of Rydberg clusters in an ultracold atomic cloud by a simple measurement of the cumulants of the underlying probability distribution. That means that positive values for M or M_3 allow to rule out models that exclusively feature excitations of individual atoms.

From this model we can deduce even more information. Assuming the effect of finite detection efficiency to be corrected, as discussed in Chapter 5, M and M_3 can reveal the existence of clusters of a certain size. This can be explained as follows: assume that excitation is only possible in clusters

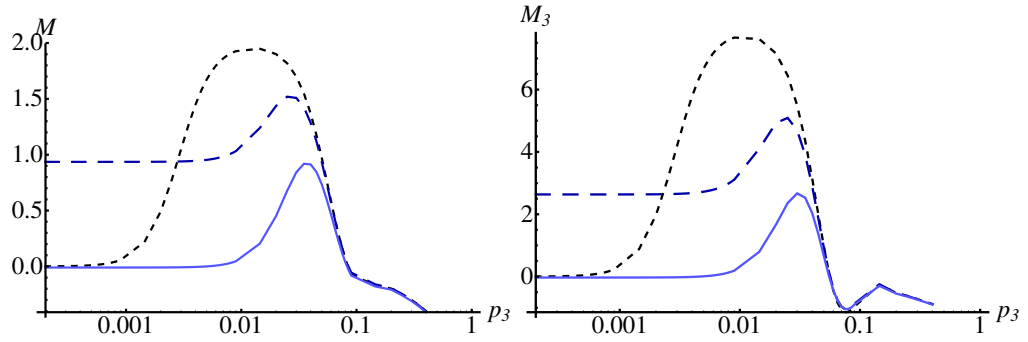

Figure 6.13: Mandel parameters M (left panel) and M_3 (right panel) as function of p_3. The size of clusters is limited by $m = 3$. The curves correspond to systems with $p_1 = 10^{-5}$ and $p_2 = 10^{-5}$ (black, short dashed), $p_1 = 10^{-5}$ and $p_2 = 10^{-2}$ (dark blue, long dashed) and $p_1 = 10^{-2}$ and $p_2 = 10^{-5}$ (light blue) at 30 atoms each. The behavior of both M and M_3 is very similar to the case of $m = 2$, which is shown in Figure 6.12. Here the maxima are much larger than in the $m = 2$ case. Only the dark blue curve is non-zero for both M and M_3 in the limit of small p_3.

of size c. Furthermore, we assume that the process of excitation of these clusters is a Poissonian process[5]. The number of excitations Q then is given by $Q = cQ_{\text{cluster}}$. Therefore, the first cumulants are found to be $\langle Q\rangle = c\langle Q_{\text{cluster}}\rangle$, $\langle\langle Q^2\rangle\rangle = \langle Q^2\rangle - \langle Q\rangle^2 = c^2\langle Q^2_{\text{cluster}}\rangle - c^2\langle Q_{\text{cluster}}\rangle^2 = c^2\langle\langle Q^2_{\text{cluster}}\rangle\rangle$ and $\langle\langle Q^3\rangle\rangle = \ldots = c^3\langle\langle Q^3_{\text{cluster}}\rangle\rangle$. For the Poissonian probability distribution all cumulants are equal, resulting in

$$M = \frac{\langle\langle Q^2\rangle\rangle}{\langle Q\rangle} - 1 = c - 1 \qquad \text{and} \qquad M_3 = \frac{\langle\langle Q^3\rangle\rangle}{\langle Q\rangle} - 1 = c^2 - 1. \tag{6.23}$$

This allows to prove the existence of at least one cluster of size $\tilde{c}$ if $M > \tilde{c} - 1$ or $M > \tilde{c}^2 - 1$ since these values cannot be produced by smaller clusters only. This effect also manifests itself in the limits of M and M_3 shown in Figures 6.12 and 6.13.

In order to compare the predictions of this section to experimental results the model has to be extended though: so far the probabilities p_i are not related to the system parameters detuning Δ, Rabi frequency Ω, interaction strength C, and density n, as introduced in Chapter 3. A further improvement of the model would be to assign the excitation probabilities individually to each atom depending on its relative position to all other atoms in the cloud.

[5]Since binomial statistics approaches Poissonian statistics if $N \to \infty$, $p \to 0$ and Np remains constant this is no critical assumption.

Chapter 7

Summary, conclusion, and outlook

Finally, we want to summarize the results presented in this thesis. As a guide we use the major goals and questions listed in Section 1.2. Afterwards we will give a brief outlook on possible future research in particular concerning new questions that arose in progress of the present work.

We accessed the ground state of an ultracold gas cloud of interacting Rydberg atoms via an exact diagonalization technique using two Hilbert space truncation schemes. Two different properties of the ground state were used to independently estimate the critical interaction strength of the transition from an unordered to a crystalline phase. First, the number of excited particles for different arrangements of atoms, which also can be measured in experiment, was determined and the corresponding excited fraction and the variance were analyzed. Two different power laws were observed in the regimes of weak and strong interactions. The critical parameter of this phase transition was obtained by identifying it with the intersection of the extrapolation of these two different power laws.

These results were simultaneously confirmed by the pair correlation function which was as well extracted from the ground state obtained by the exact diagonalization routine. It exhibits the features typical for either of the two phases, which namely are an almost constant behavior after a certain distance in the unordered phase and distinct peaks over the full system length in the crystalline phase. The critical interaction strength of the phase transition was estimated as the smallest interaction strength at which the correlations extend over the full system size. The two methods agree quantitatively since the estimates for the critical parameters obtained with either methods are compatible taking into account the fairly large uncertainty of the values for each method.

Subsequently the correlation functions of the ultracold atomic gas of Rydberg atoms was compared to a classical hard sphere model as well as a (non-)interacting electron gas. The Rydberg gas shares some similarities with each of the systems, as e.g. the blockade radius or the smooth functional dependence for small distances. Other features, like the phase transition, are not shared by these systems in one-dimensional geometry.

Having successfully treated the Rydberg gas, we transferred the method to the exciton bilayer system, a system that shares multiple properties with the Rydberg gas. With the same numerical approach the first cumulants of the distribution of the number of excitons were analyzed in one- and two-dimensional realizations, revealing a phase transition from an unordered phase to an ordered excitonic crystal. This feature manifests itself even clearer in the pair correlation function than in the case of the Rydberg gas. The critical parameter of the transition could again be estimated by either the intersection of the two power laws or by determining the point in parameter space at which correlations are present over the full system length.

In order to compare theoretical with experimental work two effects have to be taken into account. First, the effect of finite detection efficiency, which was modeled by a binomial process, was discussed. Within this model the moments – and consequently the cumulants – of the physical and measured probability distribution of the number of excitations were related. The knowledge of these relations is of particular interest for the predictions made in Section 6.3, where we pick up this topic again when treating Rydberg clusters.

The second difficulty experiments have to cope with are unstable conditions, meaning that parameters are not time-independent but may either drift slowly or even change abruptly as compared to the time scale of consecutive experimental cycles. This problem is approached by introducing a routine that subdivides a data set into pieces which then are assumed to be free of any parameter fluctuation. A subsequent permutation test allows to merge compatible data subsets. Even though it is debatable whether the data sets obtained in this way are biased, the statistical significance increases due to the larger amount of data resulting in smaller errors.

It turns out that one can circumvent the frozen gas approximation restrictions and take care of the Rydberg atom kinetics. This is done in Section 6.1 by a random walk combined with a procedure similar to the Monte Carlo Metropolis algorithm. This technique is used to find the energetic minimum of the many-particle ground state. It is found that for a large region in the parameter space this ground state displays crystalline order. Depending on whether the system approaches the global minimum or a local minimum the lattice constant may be different. Since no experimental results are available it is non-conclusive whether both types of crystals are realized.

Motivated by current experiments the model of the ultracold Rydberg gas was augmented by an additional Rydberg state in Section 6.2. Using a mean field approach the system is treated in the situation in which the additional Rydberg state is coupled only via a microwave field. The calculations reveal power laws for the excited fractions of both Rydberg levels, whereas the exponent of the laser-coupled state is found to be compatible with a previous work in a two-level system. The other exponent shows universal behavior and is independent of the system parameters.

In a different model we treat the situation in which each atom again is modeled as a two-level subsystem whose states correspond to different Rydberg states. The interaction between these states is modeled such that a pair of atoms may exchange their Rydberg state. In the case that no electromagnetic field is present to couple the states a very universal behavior is observed in the pair correlation function, which possibly is a consequence of solely geometrical or statistical effects. In presence of a laser field there is an additional feature – a steep shoulder – in the correlation function. Its existence may be explained by the fact that different terms of the Hamiltonian dominate in different regimes.

While the topics treated in Chapter 3 and 4 appear to be very conclusive and complete and Chapter 5 treats a specific situation closely related to the aforementioned chapters, Chapter 6 offers a number

of new questions that could not have been answered exhaustively within this thesis. At this point we would like to list these questions as a motivation for future research. We note that this outlook has no claim of completeness but rather is intended to remind of the broad variety of facets the ultracold Rydberg gas can be viewed in.

Considering the method of taking atom kinematics into consideration in Section 6.1, one can question the role kinetic terms really play in the situation of slow-moving atoms. Related to this one may ask whether a field theoretical treatment, in which the kinetic term is used to generate different arrangements at distinct points in time, is possible. This eventually can be used to derive a statistical average. If this procedure is valid one may even use field theoretical methods to treat the alternative Rydberg model where Rydberg atoms with different principal quantum numbers are present. In this way it might be possible to determine whether the universal behavior of the correlation function shown in Section 6.2.2 truly is a geometric effect or is of physical nature.

Moreover, the concept of Rydberg clusters seems very promising in the quest to understand elementary physics. One major question is whether these clusters are excited collectively via a multi-photon process or sequentially by a single-photon process. Besides, as already mentioned in Section 6.3, the model used here is of purely statistical nature. Therefore, it is necessary to relate the excitation probabilities to the parameters of laser and interaction strength to be able to predict the statistical properties of the ultracold gas cloud. Finally, the spacial distribution of atoms would have to be taken into account, either in a statistical way (assuming a certain distribution for the distances between atoms) or by averaging over multiple realizations as done before.

Peer-reviewed Publications

Large parts of this thesis have already been published or are currently under peer-review. Papers in preparation are also listed. (Information as of October 2, 2013)

- D. Breyel, T. L. Schmidt, and A. Komnik. Rydberg crystallization detection by statistical means. *Phys. Rev. A*, 86:023405, Aug 2012. doi:10.1103/PhysRevA.86.023405

Publications in preparation

- H. Schempp, G. Günter, M. Robert-de-Saint-Vincent, C. S. Hofmann, D. Breyel, A. Komnik, D. W. Schönleber, M. Gärttner, J. Evers, S. Whitlock, and M. Weidemüller. Full counting statistics of laser excited Rydberg aggregates in a one-dimensional geometry. *ArXiv e-prints*, August 2013

- D. Breyel, H. Soller, T. L. Schmidt, and A. Komnik. Detecting an exciton crystal by statistical means. *ArXiv e-prints*, April 2013

Publications not related to this thesis

- D. Breyel and A. Komnik. Nonequilibrium transport properties of a double quantum dot in the Kondo regime. *Phys. Rev. B*, 84:155305, Oct 2011. doi:10.1103/PhysRevB.84.155305

- H. Soller and D. Breyel. Signatures in the conductance for phase transitions in excitonic systems. *ArXiv e-prints*, August 2013

Conference/Workshop Participation

I have given the following invited talks and participated in the following conferences and workshops:

- Workshop 'Non-equilibrium transport in nanostructures', Heidelberg, 19.2.2010
- DPG meeting SKM, Regensburg, 21.-26.3.2010
- Conference 'Quantum Dynamics in Nanoscale Heterostructures', Bad Honnef, 7.-10.12.2010 [poster]
- Center for Quantum Dynamics poster session, Heidelberg, 20.10.2010 [poster]
- DPG meeting SKM, Dresden, 13.-18.3.2011 [poster]
- Conference 'Non-equilibrium transport in nanostructures', Freiburg, 8.6.2011 [talk]
- CFN Summerschool on Nano-Electronics, Bad Herrenalb, 11.-14.9.2011 [poster]
- Center for Quantum Dynamics poster session, Heidelberg, 9.11.2011 [poster]
- DPG meeting SKM, Berlin, 25.-30.3.2012 [poster]
- Center for Quantum Dynamics poster session, Heidelberg, 6.6.2012 [poster]
- Center for Quantum Dynamics Colloquium, Heidelberg, 9.1.2013 [talk]

Appendix A

Appendix I

A.1. Measurement versus expectation value

It is stated in the main text in Section 3.3.1 that it is of minor importance whether for each realization the quantum mechanical average with respect to the ground state is taken or not. The latter case closely relates to an experimental measurement in which the ground state is projected onto a basis state with a certain probability. By measurement we mean that we have the probabilities to measure a state having a certain number of excitations.

The difference of the probability distributions in case of expectation value and measurement are shown in Figure A.1. Just as expected the distribution is much narrower in the case of the expectation value. We note that in the limit of small Ω the distribution of the measurement approaches that of the expectation value. In the case $\Omega = 0$ they match exactly since in both cases the ground state is given by a single basis state (which is measured with probability 1). Since in most cases we treat systems in which $\Omega < \Delta$ this additionally supports our statement that the choice of using the measurement or the expectation value is of minor importance.

Moreover, Figure A.2 shows mean and variance of the number of excited particles in dependence on the interaction strength. While one can see that the values for the mean coincide there is a clear difference in the variance. We note that, in any case, we expect the variance in the case of the measurement to be equal or larger than in the case of the expectation value since in the latter case the contributions of very small and very large numbers of excitations average out, yielding a smaller variance. The difference shown in Figure A.2 is of little importance to us because we are interested in the functional dependence, e.g. a kink of the function. This kink then will appear in both cases at the same position (at least within our uncertainty of finding the position of the kink).

Still, we have to mention that by using the quantum mechanical expectation value instead of the measurement we forfeit the possibility to distinguish sub- and super-Poissonian distributions. This is commonly done by using the Mandel parameter which is defined as the ratio of variance over mean minus one, see Equation 2.31. The variance inserted in this expression would have to be

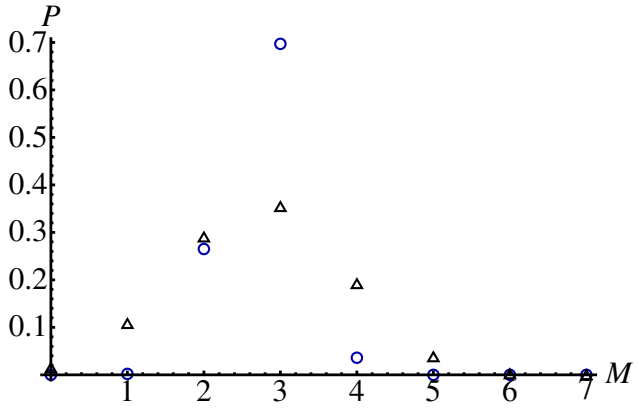

Figure A.1: Probability distribution for expectation value and measurement. The distribution of the expectation value (blue circles) is much more narrow than the distribution of measurements (black triangles). All important features are contained in both distributions. The data corresponds to $\Omega/\Delta = 2$ and $Cn^6/\Delta = 10$.

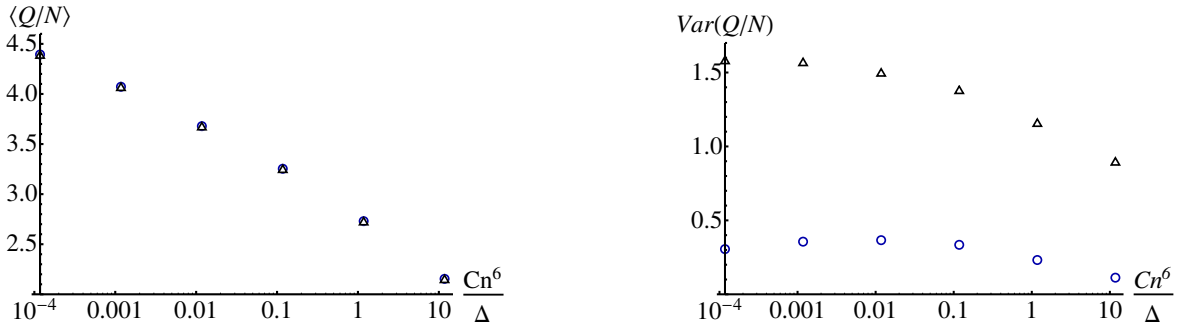

Figure A.2: Mean and variance of the distribution excited atoms. Mean number of excited atoms for expectation value (blue circles) and measurement (black triangles) coincide (left panel). The variances of expectation value and measurement differ in magnitude but show the same functional behavior (right panel). Therefore, we can choose the expectation value throughout this work. The data corresponds to $\Omega/\Delta = 2$.

the one obtained by measurements. For further discussion of this topic we would like to refer to literature (see e.g. Cubel Liebisch et al. [2005] and references therein).

A.2. Commented version of code

In this section we want to present a commented version of the source code used to generate the results shown in the main text. The version shown here is very elementary as it only serves the goal of introducing the basic principles. The code for particular situations is a modification thereof. Due to its simple form we chose the Mathematica version. The FORTRAN version of the code has a better performance but lacks readability (which is also caused by the length of the code). In the following the executable parts of the code remain in the Mathematica style while the comments appear as plain text.

In the beginning the parameters for the simulation are set. They include (in order) the number of particles, the dimension of the Hilbert space, the number of realizations and the number of bins for the correlation function. Also the range for Δ, Ω and the interaction strength are given together with the length of the system. At the end the boundary conditions are fixed and the number of states of the truncated Hilbert space are given.

```
number = 15;
dimension = 2^ number ;
repeat = 10;
grid = 200;
deltamin = 1; deltamax = 1; deltastep = 1;
C1min = 0.5; C1max = 0.5; C1step = 4 / 100;
Omegamin = 0.1; Omegamax = 15; Omegastep = 30;
length = 10;
bc = 0;
states = 50;
```

Here "$bc = 0$" stands for periodic boundary conditions, any other number stands for open boundary conditions. The number of states contributing can be changed. One finds that the results do not depend on this number once it is larger than a certain threshold. We checked for every graph that this criterion is met.

The following two functions are used to find out whether a certain particle is excited in a given state and to find the number of excited particles. They rely on the convention to represent an excited particle by "1" and a ground state one by "0".

```
k[digit_, zustand_] := IntegerDigits[zustand, 2, number][[digit]]
M[zustand_] := Sum[ k[i, zustand], {i, 1, number}]
```

The next set of functions is used to calculate the diagonal entries of the Hamiltonian matrix. Each diagonal element depends on two functions: the double sum, which in turn depends on the distances between excited particles, and an offset, which is a constant shift that ensures all diagonal elements to be positive. The latter is done since the algorithm to determine the smallest eigenvalue is more efficient this way and we are not interested in the eigenvalue itself.

```
hamdiag[alpha_] := -Delta (M[alpha] - number / 2) + C1 / 4 * abssum[alpha] + offset[Delta, Omega]
abssum[zustand_] := Sum[Sum[If[ k[i, zustand] * k[j, zustand] > 0,
                                    1 / (distance[i, j])^6, 0], {i, 1, j - 1}], {j, 1, number}]
distance[a_, b_] := If[bc == 0, Min[Abs[r[a] - r[b]],
                            length - Abs[r[a] - r[b]]](*periodic*), Abs[r[a] - r[b]](*open*)]
offset[u_, v_] := Max[{Abs[number / 2*(u - v)], Abs[number / 2*(u + v)]}]
```

This loop initialises the bins for the correlation function. The procedure to evaluate the correlation function is explained in detail in the main text in Section 3.4. In this version an index for Ω is carried since a range of values for Ω is to be covered. In case other parameters are to be varied additional iterators can be introduced at this point.

```
For[nm = Omegamin, nm ≤ Omegamax, nm = nm + Omegastep, For[t = 1, t ≤ grid, t++, alpha[nm][t] = 0]]
```

In "paket" the magnetizations of the individual runs are going to be saved. Therefore it is initialized as an empty array. When doing a scan over a range of parameters one has to keep in mind that all results are saved in this array independent of their corresponding set of parameters. Still the results can be divided easily afterwards since the order of the parameter sets and the number of samples is known.

```
paket = {};
```

Here the actual diagonalization routine begins. The first loop runs over different realizations. Additional loops have to be introduced at this point if one wants to do a scan over a range of parameters. In this case these loops are omitted since we are only interested in the basic version of the code.

```
For[count = 1, count ≤ repeat, count++, {
```

The random positions for the particles are generated as random numbers in the interval $[0, \text{length}]$. The build-in routine of Mathematica for the generation of random numbers is used.

```
For[i = 1, i ≤ number, i++, pos[i] = RandomReal[{0, length}]];
```

The parameters are set to the values defined above. In case a complete range for a parameter is to be covered an additional loop can be introduced at this point.

```
paraset = {Delta → deltamin, C1 → C1min, Omega → Omegamin};
For[i = 1, i ≤ number, i++, AppendTo[paraset, r[i] → pos[i]]];
```

An array is filled with the diagonal elements of the Hamiltonian.

```
array = Table[N[hamdiag[i]] /. paraset, {i, 1, dimension}];
order = Ordering[array, states];
```

Now the states corresponding to the smallest diagonal elements of the Hamiltonian are found. They are then relabeled to make their handling more convenient.

At this point the FORTRAN version of the code differs from this one since the size of this array grows exponentially with the number of particles. Instead a certain amount of diagonal elements is counted, then ordered and only the smallest ones are kept. Now the next diagonal elements are calculated, joined with the smallest ones of the preceding run and ordered again. In this way only a small amount of diagonal elements has to be saved while the result of the procedure is the same as with the one shown here.

```
For[i = 0, i < states, i++, {neuzustand[i] = order[[i + 1]]}];
```

With this reduced set of basis states the Hamiltonian matrix can be written down. This is done in the fashion of a sparse array to reduce storage requirements. In the FORTRAN version of the code this is much more cumbersome but also necessary to reduce computation time.

```
Hhelp = {};
For[eins = 0, eins < states, eins++,
  For[zwei = 0, zwei < eins, zwei++, If[Abs[M[neuzustand[eins]] - M[neuzustand[zwei]]] == 1,
    If[Sum[Abs[k[i, neuzustand[eins]] - k[i, neuzustand[zwei]]], {i, 1, number}] == 1,
     {AppendTo[Hhelp, {eins + 1, zwei + 1} → Omega / 2],
      AppendTo[Hhelp, {zwei + 1, eins + 1} → Omega / 2]}]]]];
For[i = 1, i ≤ states, i++, AppendTo[Hhelp, {i, i} → hamdiag[neuzustand[i - 1]]]];
Hamil = SparseArray[Hhelp /. paraset];
```

The ground state is found by diagonalization. The method of choice to do this is the Lanczos-algorithm which works explicitly well on sparse matrices. It is briefly explained in the next section.

```
vector[count] = Eigenvectors[Hamil, -1][[1]];
deltahelp = Delta /. paraset;
C1help = C1 /. paraset;
Omegahelp = Omega /. paraset;
```

The result – in this case the number of excitations – is calculated and afterwards stored in the array "paket" which in the beginning was initialized empty. The formula used here is explained in the main text.

```
magnetisierung[count][deltahelp][C1help][Omegahelp] =
  Sum[M[neuzustand[t]] * (vector[count][[t + 1]])^2, {t, 0, states - 1}];
AppendTo[paket, magnetisierung[count][deltahelp][C1help][Omegahelp]];
```

In the very end the routine to calculate the correlation function from the ground state is started. Further details on this can be found in the main text in Section 3.4.

```
For[w = 1, w ≤ number, w++, For[v = w + 1, v ≤ number, v++, For[t = 1, t ≤ grid, t++,
     If[distance[v, w] ≤ (t) * length / grid && distance[v, w] > (t - 1) * length / grid,
      alpha[Omegahelp][t] = alpha[Omegahelp][t] + Sum[(vector[count][[y + 1]])^2
          * k[v, neuzustand[y]] * k[w, neuzustand[y]], {y, 0, states - 1}]]]]]
  }]
```

A.3. Lanczos algorithm for diagonalization of sparse matrices

In this section we briefly want to introduce the algorithm used for diagonalization of the Hamiltonian. In any but the case of very few atoms this matrix is sparse since each state is coupled to only few

other states. This results from the fact that two states may only be coupled if their total number of excitations differs by one. To be coupled they also have to vary only in the state of one single particle. In this choice of diagonalization method one also has to consider that the Hamiltonian always is a Hermitian matrix (in the particular case considered in this work it is even symmetric). Two of the methods that were designed for these exact circumstances (sparsity and symmetry) are the Arnoldi-algorithm (introduced by Arnoldi [1951]) and the Lanczos-algorithm (introduced by Lanczos [1950]), which are closely related as both being iterative Krylov subspace methods. They are discussed together with numerous variations in great detail in literature. Since this is no main topic of our work we restrict us to the review article by Freund et al. [1992] and only discuss the Lanczos-algorithm since this is the one used. Lehoucq et al. [1997] give further information about the implementation and an detailed overview of the functions of ARPACK, a collection of subroutines designed to solve large-scale eigenvalue problems.

We follow the lines of Freund et al. [1992] who show the pseudo code of the Lanczos algorithm. We adapt it to the situation discussed in the previous paragraph and consider the arguments of Paige [1972] to make the algorithm numerically stable. The aim is to find the eigenvalues and eigenvectors of a matrix A. The routine is started by

- choosing a random vector $\mathbf{v}_1$ of unit length and assigning the values $v_0 = 0$ and $\beta_1 = 0$.

For these starting conditions it has to be noted that the starting vector should have no effect on the final result. As in most iterative algorithms the numerical inaccuracies eliminate the chances of coincidentally choosing a starting vector orthogonal to a certain subspace of the respective problem. Now the iteration starts with

- doing a loop for $i = 1$ to $i = m$ where the following orders are executed
  - $\mathbf{w}_j = A\mathbf{v}_j$
  - $\alpha_j = \mathbf{w}_j \cdot \mathbf{v}_j$
  - $\mathbf{w}_j = \mathbf{w}_j - \alpha_j\mathbf{v}_j - \beta_j\mathbf{v}_{j-1}$
  - $\beta_{j+1} = \mathrm{norm}(\mathbf{w}_j)$
  - $\mathbf{v}_{j+1} = \mathbf{w}_j/\beta_{j+1}$

where in the second line of the loop the scalar product is used to project $\mathbf{w}_j$ onto $\mathbf{v}_j$. In the subsequent step this projection is used to subtract the component parallel to any previously found vector $\mathbf{v}_{j-1}$. This guarantees pairwise orthogonality of the vectors $\mathbf{v}_j$. The last two steps normalize the new vector $\mathbf{v}_j$ making the vectors even orthonormal.

In each iteration of the above shown loop one obtains values α_j and β_j which then are inserted in the matrix

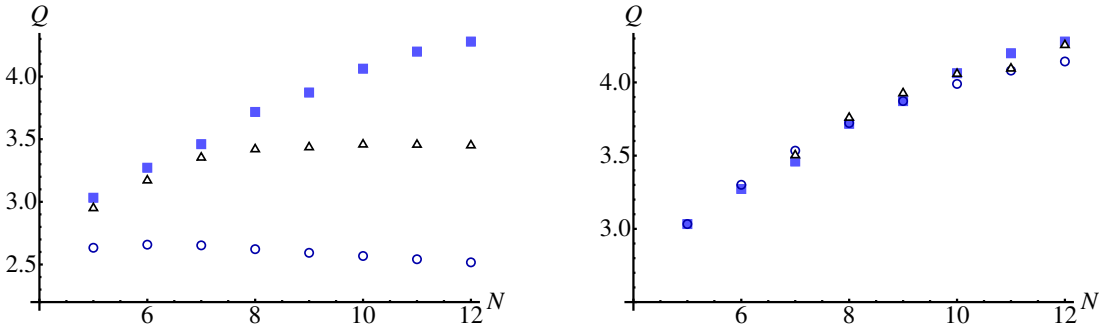

Figure A.3: Mean of excited number of particles in dependence on number of particles. The curves correspond to exact data (light blue squares) in both panels. The data sets (left panel) are taken at $M^* = 3$ (blue circles), $M^* = 4$ (black triangles). The other data sets (right panel) are taken at $M^* = 5$ (blue circles) and $M^* = 6$ (black triangles). The parameters are $\Omega/\Delta = 1$ and $Cn^6/\Delta = 60$. While in the cases $M^* = 3$ and $M^* = 4$ there is no agreement with the exact curve, the cases $M^* = 5$ and $M^* = 6$ almost coincide with the exact data. We therefore conclude that for small deviations of the parameters $M^* = 6$ is sufficient to obtain unbiased data.

$$H_m = \begin{pmatrix} \alpha_1 & \beta_2 & & & & 0 \\ \beta_2 & \alpha_2 & \beta_3 & & & \\ & \beta_3 & \alpha_3 & \ddots & & \\ & & \ddots & \ddots & \beta_{m-1} & \\ & & & \beta_{m-1} & \alpha_{m-1} & \beta_m \\ 0 & & & & \beta_m & \alpha_m \end{pmatrix}. \tag{A.1}$$

The approximate eigenvalues and eigenstates of A can now be obtained from H_m by using e.g. the well-known QR-algorithm (see e.g. Preuss et al. [2001]). While the approximate eigenvalues are directly obtained as eigenvalues of H_m the eigenvectors are computed by multiplication of V_m with the eigenvectors of H_m, where V_m is the matrix given as $V_m = (\mathbf{v}_1, \mathbf{v}_2, \ldots, \mathbf{v}_m)$.

A.4. Convergence

In this section we discuss whether the approximations used are reasonable and which values can be chosen as cut-offs. We start with the approximation that only allows a maximum number M^* of excitations.

In Figure A.3 the expectation values of the distributions are given in dependence on the particle number N for various choices of M^*. The curve we call "exact" corresponds to the case $M^* = N$ and does not contain any approximation. The exact curve can only be obtained for rather small numbers of particles because of the rapid growth of the Hilbert space that was already discussed. While on the left side of Figure A.3 one can clearly see the difference of $M^* = 3$, $M^* = 4$, and the exact curve, the difference vanishes for higher numbers of M^*. This results from the fact that for a given set of parameters the excitation of Rydberg atoms is strongly suppressed by the blockade phenomenon. Therefore, states with these larger numbers of excitations do not contribute to the

ground state. This means that it is sufficient to consider at most $M^* = 6$ excitations for the given set of parameters and $N \leq 12$ to obtain any desired (ground state) observable with negligible error.

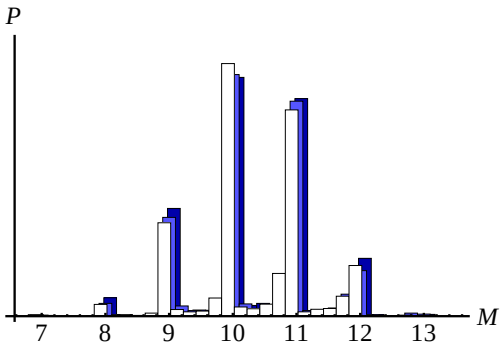

Figure A.4: Distribution of excited particles for different number of contributing basis states. The distributions correspond to $k = 100$ (dark blue), $k = 500$ (light blue) and $k = 1000$ (white). There is only very little difference between the distributions and consequentially very small difference in their cumulants as well. These remaining differences are caused by statistics since not the same set of particle arrangements was used for the three values of k. The parameters are $Cn^6/\Delta = 24.4$ and $\Omega/\Delta = 0.1$.

The second type of approximation fixes the number of states k that are used for the exact diagonalization afterwards. To see whether this type of approximation is adequate and therefore generates results that are unbiased by the approximation we compare the distributions of $k = 100$, $k = 500$ and $k = 1000$ in Figure A.4. The shown distribution correspond to 3000 samples each. The remaining differences are statistical fluctuations and do not contradict the fact the once a certain minimal value of k is overcome the result is independent on the precise value of k.

A.5. Aliasing related effect

In this section we would like to address a topic closely related to an effect called aliasing. This feature arises when using periodic boundary conditions as it is done in most of the results shown throughout this work. We will not explain aliasing in detail but concentrate on the features that manifest in our results. The effect is shown in Figure A.5, where one can see additional (secondary) peaks on the shoulders of the well-known ones (primary). In the following we will explain its origin.

Consider a one-dimensional system at a rather high particle density in the ground state. When measuring the correlation function in this system we always measure up to half of the length of the system since this is the largest possible distance between two particles and therefore no larger distances are meaningful. Now assume that parameters are chosen such that the system length is no integer multiple of the blockade radius (the effect is most prominent in case that this criterion is not even fulfilled approximately). Because of the periodic boundary conditions we can think of our system as a ring on which we place our reference particle and measure the density of excitations in distance r to it. Taking a "classical" point of view a particle can only be excited or in its ground state, therefore the most natural order appears to be the one where we find an excited particle in distance R_B to our reference particle, the next one at $2R_B$ and so on. This of course can be done

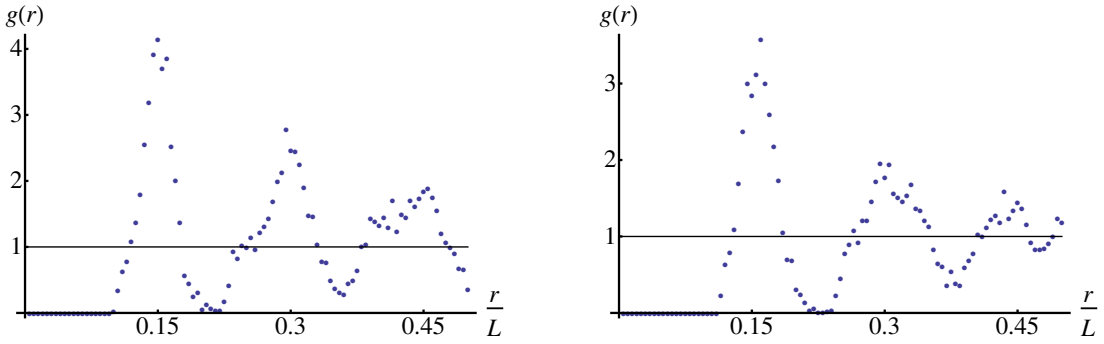

Figure A.5: Correlation functions of systems with and without aliasing related effect. While on the left side the aliasing related effect can be observed in the secondary peaks on the shoulders of the primary ones, this feature is eliminated on the right side. This is done by reducing the system length (and therefore increasing the density) such that the criterion discussed in the main text is met and keeping all other parameters constant. The parameters chosen here are $\Omega/\Delta = 25$ and $Cn^6/\Delta = 2916$ (left panel) and $Cn^6/\Delta = 5487$ (right panel).

both clockwise and counter clockwise, leading to different positions for each direction because of the above-mentioned criterion. These preferred positions are always spaced by a constant distance. When we now measure the density of excited particles clockwise we not only find an increased probability at integer multiples of the blockade radius just as discussed above but also at the points where excitation is preferred from the counter clockwise direction. This leads to additional peaks in the correlation function. All of them have the same distance to their respective neighbor. In contrast to the well-understood peaks we have discussed so far, the height of these new peaks increases with distance.

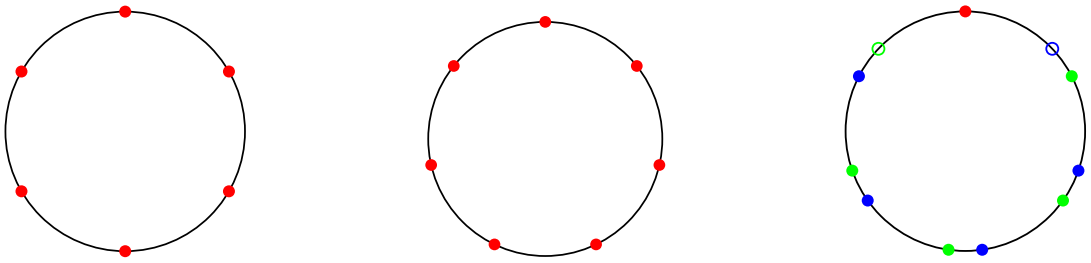

Figure A.6: Arrangements of atoms in system with periodic boundary conditions. The left and middle show situations in which the system length is an integer multiple of the blockade radius, points of high probability of finding an excitation are marked with a red dot. In all cases the red dot at the top is taken as a reference particle. On the right the ratio of system length and blockade radius is non-integer. Green dots correspond to preferred ordering clockwise and blue dots to preferred ordering counter clockwise. The small open circles represent excitations that are suppressed due to blockade with the reference particle. The constant spatial difference between blue and green particles gives rise to the feature observed in the correlation functions.

In Figure A.6 we demonstrate this feature. The left and center sketch show systems in which the criterion of the system length being an integer multiple of the blockade radius is met. In this case only the primary peaks appear in the correlation function. The situation is changed in the system on the right. Here the above criterion is violated, leading to different preferred positions for

clockwise and counter clockwise ordering of the excitations. On can see that each pair of neighboring excitations of clockwise and counter clockwise ordering has the same spatial distance. Also, the correlation between nearest neighbors is always stronger than between next-to-nearest neighbors and so on. Therefore, the size of the peaks in the correlation function decreases with increasing order of neighborhood. The opposite is true for the secondary peaks since they are ordered in the opposite direction.

Finally, we want to rule out other possibilities that might have caused additional peaks in the correlation function. The only two options we can think of are dimerization and the formation of sublattices. In the first case the double peak structure must appear at every peak including the first order maximum which apparently is not the case here. Therefore, it cannot be the reason for the observed feature. In the second case one has to face to major points which preclude this possibility to be the reason for the additional peaks: if there were different sublattices the height of higher order secondary peaks should decrease but not increase as it happens here. The second reason is that a second sublattice introduces a second length scale to the system. This does not seem to be reasonable to us since this second length scale then should appear in any other correlation function as well and not be affected by the ratio of blockade radius and system length.

We conclude this section by noting that this feature also confirms the existence of an ordered phase. The appearance of the secondary peaks is only possible because the ordering in the system extends around the full ring (one-dimensional system with periodic boundary conditions). This means that the order exceeds the length of the system which we take as a criterion for a system to be in a crystalline phase.

A.6. Alternative method: Imaginary time propagation

In this section we want to present a method which can be seen as an alternative to the exact diagonalization even though the methods share some common ground. By this we mean that both the imaginary time propagation (ITP) and the exact diagonalization via the Lanczos method are iterative methods to obtain the eigenvalues of a given matrix. While in case of the Lanczos method in principle all eigenvalues can be obtained this is rather cumbersome in the case of the ITP. As we will see ITP, also known as vector iteration, relies on the repeated multiplication of the matrix with a random vector.

The idea of the procedure is to apply the operator

$$e^{-\tau\mathcal{H}} = \lim_{n\to\infty}\left(1 - \frac{\tau\mathcal{H}}{n}\right)^n \tag{A.2}$$

to an (arbitrary) initial state. In the limit of infinitely large times τ this operator projects any state onto the (not yet normalized) ground state of the system. Normalization then yields the desired ground state of the system. To begin with, we will treat the non-interacting case only which we will also treat analytically after we have introduced the numerical procedure. Every state now can be represented by a vector

$$|\psi\rangle = \left| \begin{pmatrix} \alpha \\ \beta \end{pmatrix}, \begin{pmatrix} \alpha' \\ \beta' \end{pmatrix}, \ldots, \begin{pmatrix} \alpha^{(N-1)} \\ \beta^{(N-1)} \end{pmatrix} \right\rangle, \tag{A.3}$$

composed of N 2-vectors, each representing the state of a particle which is normalized if $|\alpha^{(i)}|^2 + |\beta^{(i)}|^2 = 1$ for all i. We now have to express the Hamiltonian in this basis. Having done this we can proceed with the following approximation

$$\lim_{n\to\infty} \left(1 - \frac{\tau\mathcal{H}}{n}\right)^n |\psi\rangle \overset{n\text{large}}{\approx} \left(1 - \frac{\tau\mathcal{H}}{n}\right)^n |\psi\rangle. \tag{A.4}$$

We see that we have two independent parameters τ and n on the right hand side. While n specifies the number of iterations we want to rename the ratio

$$\frac{\tau}{n} \equiv \Delta\tau \tag{A.5}$$

which we will call step size from now on. For n certainly a large number is desired since the approximation then improves. In contrast we expect that we have to choose τ also rather large since we want to propagate the state to large times. This leaves us with the question whether $\Delta\tau$ is of small, moderate or large magnitude (large and small with respect to Δ as a scale). The answer to this question is that both can be true: large $\Delta\tau$ improve the speed of our calculation while too large $\Delta\tau$ lead to instabilities in the calculation. In practice it seems to work best when we chose $\Delta\tau$ to be the smallest scale in the system and to increase the number of iterations to achieve the desired accuracy. We made an appropriate choice for all results shown. Since no new results are obtained in comparison to the exact diagonalization we will not further concentrate on this issue.

In case of the non-interacting system the calculation to obtain the expectation value of excited particles can be calculated analytically. We present this calculation just as a check to the calculation shown in Section 3.2. Of course, the results are expected to be the same.

We note that is again enough to treat the problem of a single particle and obtain the result for N particles afterwards by multiplication. We start by using Equation (3.6) to obtain

$$e^{-\tau\mathcal{H}} = \exp\left(-\tau\frac{1}{2}\begin{pmatrix} -\Delta & \Omega \\ \Omega & \Delta \end{pmatrix}\right) \equiv \exp\left(-\tilde{\tau}\begin{pmatrix} -\Delta & \Omega \\ \Omega & \Delta \end{pmatrix}\right), \tag{A.6}$$

where we absorbed the factor of $1/2$ in $\tilde{\tau}$ which we will rename as τ from now on. This matrix exponential can be calculated be elementary means and is given by

$$e^{-\tau\mathcal{H}} = \begin{pmatrix} \cosh(\Lambda\tau) - \frac{\Delta}{\Lambda}\sinh(\Lambda\tau) & -\frac{\Omega}{\Lambda}\sinh(\Lambda\tau) \\ -\frac{\Omega}{\Lambda}\sinh(\Lambda\tau) & \cosh(\Lambda\tau) + \frac{\Delta}{\Lambda}\sinh(\Lambda\tau) \end{pmatrix}, \tag{A.7}$$

where we introduced $\Lambda = \sqrt{\Delta^2 + \Omega^2}$ to be able to display the formula conveniently. Now we take a random vector which we assume to be normalized

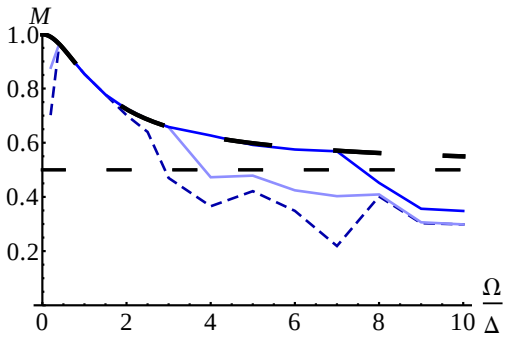

Figure A.7: Magnetization (excited fraction $\langle Q/N \rangle$) in dependence of Ω. The step size was set to $\Delta\tau = 0.01$. While the data for 200 (dark blue, short dashed) and 400 (light blue, solid line) iterations only agree with the exact solution (black, long dashed) in the regime of small Ω/Δ the data for 1000 iterations already converged for most of the range shown.

$$|v\rangle = \begin{pmatrix} \alpha \\ \beta \end{pmatrix} \qquad \text{with} \qquad |\alpha|^2 + |\beta|^2 = 1, \tag{A.8}$$

which we will propagate in imaginary time. For infinitely long times this will converge towards the ground state

$$|v_{\mathrm{GS}}\rangle = \lim_{\tau \to \infty} \frac{e^{-\tau \mathcal{H}} |v\rangle}{|e^{-\tau \mathcal{H}} |v\rangle|} \tag{A.9}$$

of the system. After inserting Equation (A.7) into Equation (A.9) a straightforward calculation yields

$$|v_{\mathrm{GS}}\rangle = \frac{\tilde{\mathcal{H}}|v\rangle}{|\tilde{\mathcal{H}}|v\rangle|} = \frac{1}{|\tilde{\mathcal{H}}|v\rangle|} \begin{pmatrix} \alpha - \frac{\alpha\Delta + \beta\Omega}{\Lambda} \\ \beta + \frac{\beta\Delta - \alpha\Omega}{\Lambda} \end{pmatrix}, \tag{A.10}$$

where we defined $\tilde{\mathcal{H}}$ by the right hand side of Equation (A.7) in the limit of τ to infinity. This ground state, just as we expected, coincides with the one obtained previously. To both confirm this claim as well as to give some further insight we numerically evaluate the magnetization for finite n. The results are shown in Figure A.7. Here one can see that the result agrees with the exact solution almost perfectly for 1000 iterations up to a certain value of Ω/Δ but has some fluctuations for smaller numbers of iterations. We note that the result is completely independent on the starting vector.

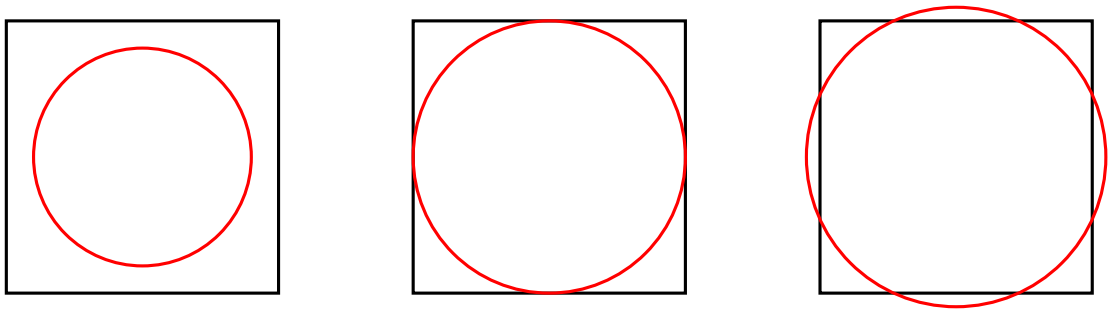

Figure A.8: Three possible situations for the distance of a particle to a reference one. We assume a reference particle at the center in all three cases, a particle in distance r can be found on the red circle. The area of the circle first increases quadratically (left) and then reaches the borders of the system (middle). Once the radius of the circle is larger than half the system size the area on the outside has to be subtracted to maintain proper normalization.

A.7. Dimension dependent normalization

So far, when considering one-dimensional systems, there was no need to normalize the data generated. By normalization we mean that we have to take into account the probability of finding a particle (regardless of whether it is excited or not) in distance r to the reference particle. In the one-dimensional system with periodic boundary conditions the distances between randomly and uniformly distributed particles are themselves randomly and uniformly distributed. Therefore, our method of evaluating the correlation function is not biased by the distribution of the distances.

The situation changes in a two-dimensional system (and in any higher dimension as well, we do not discuss it here though). Taking one particle as reference particle we see that the probability of finding another particle at larger distances is greater than finding a particle at a short distance since the area of the ring with inner radius r and outer radius $r + \Delta r$ grows linearly with r.

In our calculations we always use a quadratic system with edges of length L. That means that the largest distance possible between two particles is $\sqrt{2}L$ in case of open boundary conditions and $L/\sqrt{2}$ in case of periodic boundary conditions, which we treat here. The largest circle that fits within the system has a radius of $L/2$. Therefore, if we want to calculate the area within a distance r around the reference particle, we have to distinguish the cases $0 < r < L/2$ and $L/2 \leq r < L/\sqrt{2}$. This is illustrated in Figure A.8 where the distance r around the reference particle is indicated by a red circle and the system by a black square. A simple calculation yields

$$A(r) = \begin{cases} \pi r^2 & \text{for } 0 < r < L/2 \text{ and} \\ \pi r^2 - 4\left[\cos^{-1}\left(\frac{L}{2r}\right) r^2 - \frac{L}{2}\sqrt{r^2 - \frac{L^2}{4}}\right] & \text{for } L/2 \leq r < L/\sqrt{2} \end{cases} \tag{A.11}$$

for the area of interest. Since we are interested in particles within the distance interval $[r, r + \Delta r]$ we have to take the derivative with respect to r of this expression

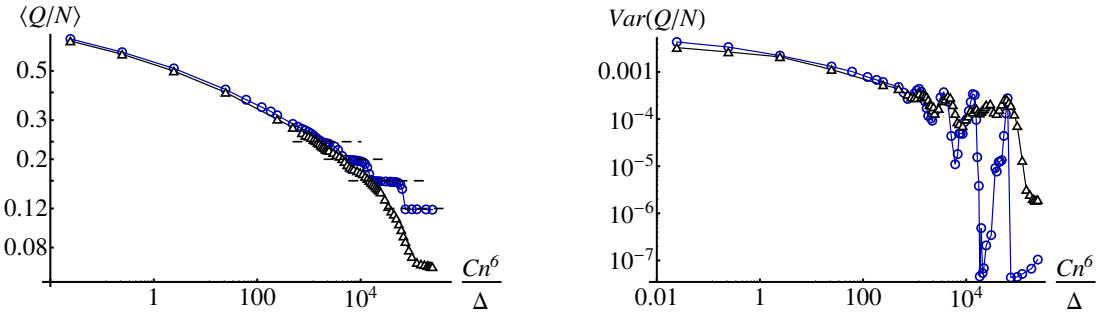

Figure A.9: Mean (left panel) and variance (right panel) of normalized number of Rydberg atoms. The dark blue data (circles) corresponds to $\Omega/\Delta = 0.1$ and the black to $\Omega/\Delta = 10$ (triangles). The dashed lines (left panel) serve as a guide to the eye only which indicate integer values of excitations (fractions with denominator 25, where $N = 25$).

$$a(r) = \begin{cases} 2\pi r & \text{for } 0 < r < L/2 \text{ and} \\ 2\pi r - 8r\cos^{-1}\left(\frac{L}{2r}\right) + \frac{2Lr}{\sqrt{r^2 - \frac{L^2}{4}}} & \text{for } L/2 \leq r < L/\sqrt{2}. \end{cases} \tag{A.12}$$

As explained earlier the program produces the correlation function for a given bin size as the cumulative sum over numerous samples. The value obtained in every bin now has to be normalized by $1/a(r)$, where r is chosen such that is in the center of the respective bin. In this way the data of one- and two-dimensional system become comparable.

A.8. Finite size effects

Mean and variance of the normalized number of Rydberg atoms were already discussed in the main text. Here we would like to show effects that arise from the finite size of the simulation volume as well as the finite number of particles therein. Typical curves for both mean and variance are shown in Figure A.9. They show steps and kinks which are characteristic for finite size effects. In case of the mean dashed lines indicate values at which an integer number of atoms is excited to the Rydberg state. These lines coincide with the steps of the curve showing that the volume is blockaded by an integer number of excitations. In case of $\Omega/\Delta \geq 1$ the steps and kinks are not as prominent since the underlying probability distribution does not consist of sharp peaks any more (as shown in Section 3.3.4).

The question arises whether the procedure used to detect the phase transition can still be applied since it relies on assigning a power law to both phases whose intersection then is computed. We believe that this is still possible. As one can see in Figure A.9 the curve is either smooth as in the case of the mean for $\Omega/\Delta = 10$ and the power law can be fitted or has fluctuations which start at approximately the same interaction strength as the power law indicates. Since the fitting method does not have a high accuracy the critical point can still be estimated with almost the same precision by choosing the point where fluctuations start. Also, one may use the minima of the fluctuation structure in the variance as a rough estimated of where the power law is to be found and the previous fitting routine still works properly.

Also, the correlation function may be subject to finite size effects. Since there is no indication that the results shown here are affected in any way besides the already discussed aliasing-related effect, no discussion on this topic is given. Further details are given by Gärttner et al. [2012b].

Appendix B

Appendix II

B.1. Calculation of cumulants effected by finite detection efficiency

Here we briefly want to present the calculation that leads to the expressions given in the main text. We use the definition of the n^{th} moment $\langle Q^n \rangle$ which is given by

$$\langle Q^n \rangle = \text{Expectation value}(Q^n) = \sum_{Q=0}^{\infty} Q^n P(Q), \tag{B.1}$$

where $P(Q)$ is the underlying probability distribution, which gives probability to detect Q Rydberg atoms[1] in a single measurement. Assuming a binomial measuring process

$$f_\eta(Q'|Q) = \left(\begin{array}{c} Q \\ Q' \end{array} \right) \eta^{Q'} (1-\eta)^{Q-Q'} \tag{B.2}$$

the probability distribution of the measured number of Rydberg atoms is given by

$$P'(Q') = \sum_{Q=0}^{\infty} f_\eta(Q'|Q) P(Q). \tag{B.3}$$

With this knowledge we can compute the first moment

[1] In the case of a continuous variable Q the summation has to be replaced by an integration. Since we always treat Rydberg atoms Q is integer and there is no need for integration.

$$\begin{aligned}\langle Q' \rangle &= \sum_{Q'} Q' \sum_{Q} f_\eta(Q'|Q) P(Q) \\ &= \sum_{Q} P(Q) \sum_{Q'} Q' f_\eta(Q'|Q) \\ &= \eta \sum_{Q} Q P(Q) \\ &= \eta \langle Q \rangle, \end{aligned} \tag{B.4}$$

where we have used that the first moment of a binomial distribution is given by $\langle Q \rangle = \eta Q$, the second moment

$$\begin{aligned}\langle Q'^2 \rangle &= \sum_{Q'=0}^{N} Q'^2 P'(Q') \\ &= \sum_{Q'} Q'^2 \sum_{Q} f_\eta(Q'|Q) P(Q) \\ &= \sum_{Q} P(Q) \sum_{Q'} Q'^2 f_\eta(Q'|Q) \\ &= \sum_{Q} P(Q) \left[\eta Q - \eta^2 Q(1-Q)\right] \\ &= \eta^2 \left[\sum_{Q} Q^2 P(Q) - \sum_{Q} Q P(Q)\right] + \eta \sum_{Q} Q P(Q) \\ &= \eta^2 \left(\langle Q^2 \rangle - \langle Q \rangle\right) + \eta \langle Q \rangle, \end{aligned} \tag{B.5}$$

and the third moment

$$\begin{aligned}\langle Q'^3 \rangle &= \sum_{Q'} Q'^3 P'(Q') \\ &= \sum_{Q'} Q'^3 \sum_{Q} f_\eta(Q'|Q) P(Q) \\ &= \sum_{Q} P(Q) \sum_{Q'} f_\eta(Q'|Q) Q'^3 \\ &= \sum_{Q} P(Q) \left[\eta Q + 3\eta^2 (Q-1) + \eta^3 Q(Q-1)(Q-2)\right] \\ &= \eta \sum_{Q} Q P(Q) + 3\eta^2 \sum_{Q} (Q-1) P(Q) + \eta^3 \sum_{Q} Q(Q-1)(Q-2) P(Q) \\ &= \langle Q \rangle (\eta - 3\eta^2 + 2\eta^3) + \langle Q^2 \rangle (3\eta^2 - 3\eta^3) + \eta^3 \langle Q^3 \rangle. \end{aligned} \tag{B.6}$$

These expressions now can be used to evaluate the variance and the third cumulant of the measured distribution by inserting them into $\langle\langle Q'^2\rangle\rangle = \langle Q'^2\rangle - \langle Q'\rangle^2$, and $\langle\langle Q'^3\rangle\rangle = \langle Q'^3\rangle - 3\langle Q'^2\rangle\langle Q'\rangle + 2\langle Q'\rangle^3$. We find

$$\langle\langle Q'^2\rangle\rangle = \eta^2\left(\langle Q^2\rangle - \langle Q\rangle^2 - \langle Q\rangle\right) + \eta\langle Q\rangle \tag{B.7}$$

and

$$\begin{aligned}\langle\langle Q'^3\rangle\rangle = \eta\langle Q\rangle + 3\eta^2\left(\langle Q^2\rangle - \langle Q\rangle - \langle Q\rangle^2\right)\\ + \eta^3\left(2\langle Q\rangle - 3\langle Q^2\rangle + \langle Q^3\rangle - 3\langle Q^2\rangle\langle Q\rangle + 3\langle Q\rangle^2 + 2\langle Q\rangle^3\right),\end{aligned} \tag{B.8}$$

respectively.

B.2. Transformation of Poisson distribution

A Poisson distribution is measured as a Poisson distribution under the assumption of a binomial measuring process. The proof of this statement is given by

$$\begin{aligned}P'(Q') &= \sum_Q \left(\begin{array}{c} Q \\ Q' \end{array}\right)\eta^{Q'}(1-\eta)^{Q-Q'}\frac{\mu^Q}{Q!}e^{-\mu}\\ &= \sum_Q \frac{\mu^Q}{Q'!(Q-Q')!}\eta^{Q'}(1-\eta)^{Q-Q'}e^{-\mu}\\ &= e^{-\mu}\sum_Q \frac{\mu^{Q-Q'}\mu^{Q'}}{Q'!(Q-Q')!}\eta^{Q'}(1-\eta)^{Q-Q'}\\ &= e^{-\mu}\frac{(\eta\mu)^{Q'}}{Q'!}\sum_Q \frac{\mu^{Q-Q'}}{(Q-Q')!}(1-\eta)^{Q-Q'}\\ &= e^{-\mu}e^{(1-\eta)\mu}\frac{(\eta\mu)^{Q'}}{Q'!}\\ &= e^{-\eta\mu}\frac{(\eta\mu)^{Q'}}{Q'!} = P_{\eta\mu}(Q').\end{aligned} \tag{B.9}$$

B.3. Details on experimental data

To obtain the data shown in the main text the experiment has to be performed many times and each time the detector signal has to be recorded. This signal is then given as a function $I(t)$ of

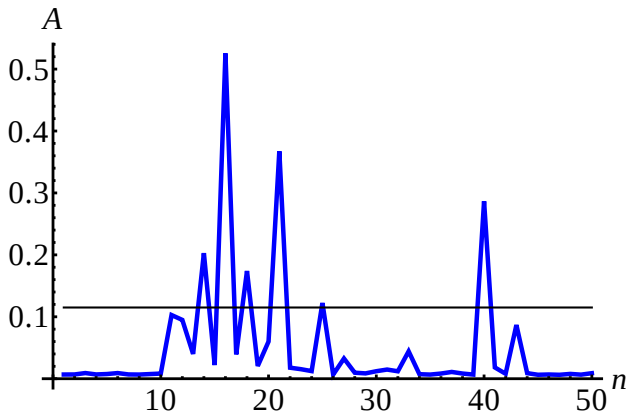

Figure B.1: Amplitudes A of 50 fitted peaks in the detector signal. The amplitude is given in arbitrary units. The abscissa labels the number n of the fitted peak (see text). The black horizontal line indicates the threshold. In this particular example six Rydberg atoms are counted. The data shown here is taken from the data sets introduced in the main text, see footnote 4 in Section 5.2.

current in dependence on time. To deduce the actual number of Rydberg atoms from this signal the following routine is applied by the experimentalist: the typical signal of an ion of a Rydberg atom is recorded. This signal then is translated to a function $f(t, \{a_1, a_2, \ldots\})$ with several fitting parameters $a_1, a_2, \ldots$. Once the signal of an experimental cycle is recorded $f(t, \{a_1, a_2, \ldots\})$ is fitted to the 50 (this number is chosen rather arbitrarily, but is reasonable in magnitude) most prominent peaks of the signal which show the characteristics of the previously recorded typical peak. The maximum of the function f, which we call amplitude A, for each of these 50 fits is written down for this particular peak. An example of this is shown in Figure B.1. Here n labels the number of the fitted peak from one to 50. Even though the numbers of the peaks orders them chronologically (in the order they hit the detector) the number of peaks may not be understood as a (linear) measure of time since difference in time between adjacent peaks is random. Now a threshold has to be introduced which states whether a certain peak is counted as an actual event or background. This threshold can be chosen basically freely within a reasonable range but has to be the same for each experimental cycle. Having defined this threshold one simply has to count the number of peaks whose amplitudes surmount the threshold. In this way the statistic shown in Section 5.2 can be found.

We would like to remark that even though the choice of the threshold is free (and in principle should not effect the physics) one has to pay attention at this point. While a low threshold allows for background to be counted as actual events a high threshold may exclude actual events from being counted and in both ways the statistics may be altered. In Figure B.2 the first three cumulants of the high density data set are shown in dependence on the threshold λ. Even though no rigorous bounds can be put on the threshold λ, the range $[0.07, 0.1]$ appears to be the most reasonable one since above the distribution becomes more and more Poissonian indicating a purely random process. Of course, we cannot exclude the possibility that this resembles the physical reality but our expectations based on the simulations presented in Chapter 3 suggest that this might not be reasonable. On the other side a very low threshold results in high particle counts which are not expected a priori from the experimental parameters. Finally, we note that the threshold gives one the opportunity to change the detection efficiency η even after the experiment is finished. As discussed above a low threshold corresponds to a high detection efficiency but also is prone to background miscounts. Also, there is no evidence for a simple functional relation between λ and η and therefore we only chose one fixed

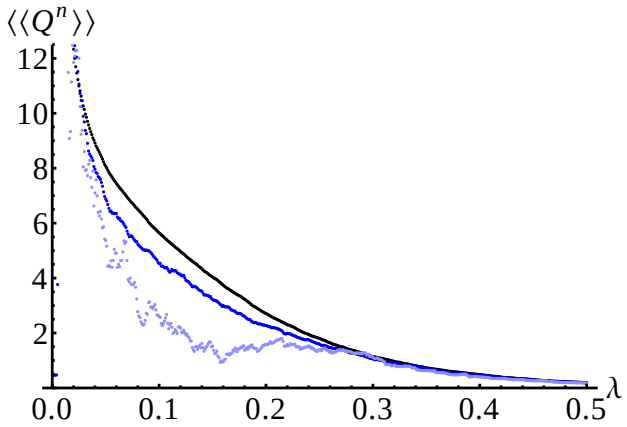

Figure B.2: Cumulants of high density data set in dependence on threshold λ. Mean (black), variance (dark blue) and third cumulant (light blue) all drop for increasing threshold. For values $\lambda \gtrsim 0.2$ the distribution becomes more and more Poissonian while for values $\lambda \lesssim 0.07$ the fluctuations of the third cumulant get greater and the total number of Rydberg atoms gets unreasonably high.

threshold and do not change it during the data analysis.

B.4. Subdivision algorithm

In this section we show the commented routine to find the parameter changes in given data. Afterwards we will apply this procedure to a data set for which we predefined the parameter changes so that we can check whether they can be reconstructed. Again we would like to remark that this does not give full certainty for no further parameter changes to exist or any of the changes found not to correspond to statistical fluctuations, but we see no better possibility to approach this problem.

First the function

```
V[d_] := Total[(d - Mean[d])^2]
```

is defined. It takes a data set as an argument and sums the squared residuals (relative to the mean of the data set) of each data point within this set. The smaller the value of this function, the closer data points lie relative to the mean. Certainly, this value depends on the variance of the distribution from which this data set was generated. Assuming that the type of distribution does not change while the parameters vary allows this to be a measure of how stable the parameters where within a certain set of data.

The function

```
L[d_, f_, t_, cuts_] := Block[{data = Take[d, {f, t}], v, cut, cc, j},
```

takes multiple arguments. The first argument d is the data set, the second and third argument define the range of the data set which one wants to investigate and the last argument is a list of numbers which give the position of already detected parameter changes. In the beginning of the routine this list is empty and never can contain neither "1" or "l", where l is the length of the data set. The statement

```
If[t - f < 5, Return[{}]];
```

is only included to ensure that the given data set has at least length five. This threshold is implemented since a division of an even shorter data set is not meaningful by construction. Now a table

```
v = Table[cc = DeleteDuplicates[Sort[cuts ~ Join ~ {1, n, Length[data]}]];
   Sum[V[Take[data, {cc[[j]], cc[[j + 1]]}]], {j, 1, Length[cc] - 1}], {n, 2, Length[data] - 2}];
```

is generated. Every entry of this table is given by the sum over the function V, which was defined above, applied to a subset of the full data set. The subsets are defined by the cuts from previous recursions and a trial cut which is given by the table index. Having computed this table the line

```
v2 = Delete[v, Table[{cuts[[o]] - 1}, {o, 1, Length[cuts]}]];
```

creates another table from which the previously found cuts are deleted. The offset of one is needed since the table v started with index two. In the table v_2 one can now look for the best choice of a new cut by finding the minimum and then finding the position of this minimum in table v. Again, an offset of one has to be included in

```
cut = Position[v, Min[v2]][[1, 1]] + 1;
```

to correct for the offset in the table v. Finally, the new cut can be collected in the *cuts* table

```
cuts ~ Join ~ {cut}
```

and the procedure can be started over. In this way arbitrarily many cuts can be found but as we mentioned above the procedure can be stopped once the cuts start to accumulate at certain positions since then no further new ones are expected.

Figure B.3 shows a data set of Gaussian distributed data with mean zero for the first 300 data points, mean 0.4 for the next 300 data points, and mean -0.2 for the last 400 data points. Our algorithm is tested with sample data sets like this one to check whether the positions of parameter changes (300 and 600 in this case) can be reproduced correctly. Obviously both instances are detected with sufficient accuracy. The instances that are detected at the beginning and the end

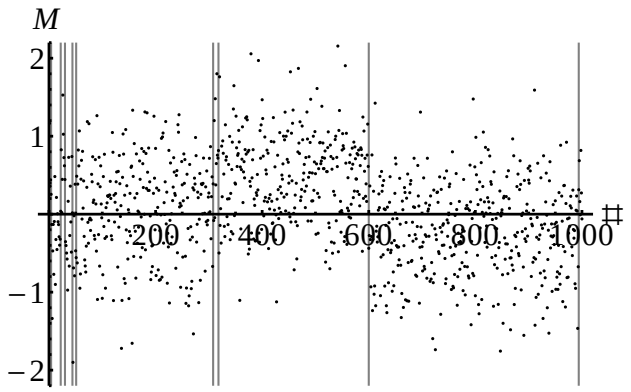

Figure B.3: Normal distributed data with offset. The data points (black) are normal distributed with a mean of zero for the first 300 data points, with a mean of 0.4 for the next 300 data points, and with a mean of -0.2 for the remaining 400. The vertical lines indicate the positions of detected parameter changes. The accumulation of detected parameter changes at the beginning of the data series hints that all major changes in parameters have been detected.

show that there are most likely no further parameter changes in this sample since a clustering of detected parameter changes suggests that only little benefit is given by further detection of additional subsets. The results shown here are very typical for a test of the algorithm. In almost any case all predefined parameter changes can be detected as long as the difference in means is sufficiently large. Also, on very few occasions only parameter changes are detected which do not coincide with the predefined ones other than at the ends of the data set. For the experimental data sets additionally a permutation test can be performed to check the degree of which two subsets belong to the same distribution, which cannot be performed by this algorithm.

Bibliography

M. Alloing, D. Fuster, Y. Gonzalez, L. Gonzalez, and F. Dubin. Observation of macroscopic coherence in self-organized dipolar excitons. *ArXiv e-prints*, page 1210.3176, 2012.

B. L. Altshuler, P. A. Lee, and R. A. Webb. *Mesoscopic Phenomena in Solids*. Human Factors in Information Technology. North-Holland Publ., 1991. ISBN 9780444884541.

T. Amthor, J. Denskat, C. Giese, N. N. Bezuglov, A. Ekers, L. S. Cederbaum, and M. Weidemüller. Autoionization of an ultracold rydberg gas through resonant dipole coupling. *The European Physical Journal D - Atomic, Molecular, Optical and Plasma Physics*, 53:329–335, 2009a. ISSN 1434-6060. 10.1140/epjd/e2009-00119-4.

T. Amthor, M. Reetz-Lamour, and M. Weidemüller. *Cold Atoms and Molecules: Concepts, Experiments and Applications to Fundamental Physics*. Wiley-VCH, Berlin, 2009b.

Thomas Amthor, Markus Reetz-Lamour, Christian Giese, and Matthias Weidemüller. Modeling many-particle mechanical effects of an interacting Rydberg gas. *Phys. Rev. A*, 76:054702, Nov 2007. doi:10.1103/PhysRevA.76.054702.

M. H. Anderson, J. R. Ensher, M. R. Matthews, C. E. Wieman, and E. A. Cornell. Observation of Bose-Einstein Condensation in a Dilute Atomic Vapor. *Science*, 269:198–201, July 1995. doi:10.1126/science.269.5221.198.

W. R. Anderson, J. R. Veale, and T. F. Gallagher. Resonant Dipole-Dipole Energy Transfer in a Nearly Frozen Rydberg Gas. *Phys. Rev. Lett.*, 80:249–252, Jan 1998. doi:10.1103/PhysRevLett.80.249.

W. E. Arnoldi. The principle of minimized iterations in the solution of the matrix eigenvalue problem. *Q. Appl. Math.*, 9(17):17–29, 1951.

G. E. Astrakharchik, J. Boronat, I. L. Kurbakov, and Yu. E. Lozovik. Quantum phase transition in a two-dimensional system of dipoles. *Phys. Rev. Lett.*, 98:060405, Feb 2007. doi:10.1103/PhysRevLett.98.060405.

C. Ates and I. Lesanovsky. Entropic enhancement of spatial correlations in a laser-driven Rydberg gas. *Phys. Rev. A*, 86:013408, Jul 2012. doi:10.1103/PhysRevA.86.013408.

C. Ates, S. Sevinçli, and T. Pohl. Electromagnetically induced transparency in strongly interacting Rydberg gases. *Phys. Rev. A*, 83(4):041802, Apr 2011. doi:10.1103/PhysRevA.83.041802.

Waseem S. Bakr, Jonathon I. Gillen, Amy Peng, Simon Folling, and Markus Greiner. A quantum gas microscope for detecting single atoms in a Hubbard-regime optical lattice. *Nature*, 462(7269): 74–77, November 2009. ISSN 0028-0836.

M. L. Bellac, F. Mortessagne, and G. G. Batrouni. *Equilibrium and Non-Equilibrium Statistical Thermodynamics*. Cambridge University Press, 2004. ISBN 9780521821438.

John M. Blatt. Practical points concerning the solution of the Schrödinger equation. *Journal of Computational Physics*, 1(3):382–396, 1967. ISSN 0021-9991. doi:http://dx.doi.org/10.1016/0021-9991(67)90046-0.

John M. Blatt, K. W. Böer, and Werner Brandt. Bose-Einstein Condensation of Excitons. *Phys. Rev.*, 126:1691–1692, Jun 1962. doi:10.1103/PhysRev.126.1691.

Rainer Blatt and David Wineland. Entangled states of trapped atomic ions. *Nature*, 453(7198): 1008–1015, June 2008. ISSN 0028-0836.

Immanuel Bloch, Jean Dalibard, and Wilhelm Zwerger. Many-body physics with ultracold gases. *Rev. Mod. Phys.*, 80:885–964, Jul 2008. doi:10.1103/RevModPhys.80.885.

Christophe Boisseau, Ionel Simbotin, and Robin Côté. Macrodimers: Ultralong Range Rydberg Molecules. *Phys. Rev. Lett.*, 88(13):133004, Mar 2002. doi:10.1103/PhysRevLett.88.133004.

S. Bose. Plancks Gesetz und Lichtquantenhypothese. *Zeitschrift fur Physik*, 26:178–181, December 1924. doi:10.1007/BF01327326.

C. C. Bradley, C. A. Sackett, J. J. Tollett, and R. G. Hulet. Evidence of Bose-Einstein Condensation in an Atomic Gas with Attractive Interactions. *Phys. Rev. Lett.*, 75:1687–1690, Aug 1995. doi:10.1103/PhysRevLett.75.1687.

D. Breyel and A. Komnik. Nonequilibrium transport properties of a double quantum dot in the Kondo regime. *Phys. Rev. B*, 84:155305, Oct 2011. doi:10.1103/PhysRevB.84.155305.

D. Breyel, T. L. Schmidt, and A. Komnik. Rydberg crystallization detection by statistical means. *Phys. Rev. A*, 86:023405, Aug 2012. doi:10.1103/PhysRevA.86.023405.

D. Breyel, H. Soller, T. L. Schmidt, and A. Komnik. Detecting an exciton crystal by statistical means. *ArXiv e-prints*, April 2013.

H. P. Büchler, E. Demler, M. Lukin, A. Micheli, N. Prokof'ev, G. Pupillo, and P. Zoller. Strongly Correlated 2D Quantum Phases with Cold Polar Molecules: Controlling the Shape of the Interaction Potential. *Phys. Rev. Lett.*, 98:060404, Feb 2007. doi:10.1103/PhysRevLett.98.060404.

L. V. Butov, A. C. Gossard, and D. S. Chemla. Macroscopically ordered state in an exciton system. *Nature*, 418(6899):751–754, August 2002. ISSN 0028-0836.

Thomas J. Carroll, Katharine Claringbould, Anne Goodsell, M. J. Lim, and Michael W. Noel. Angular Dependence of the Dipole-Dipole Interaction in a Nearly One-Dimensional Sample of Rydberg Atoms. *Phys. Rev. Lett.*, 93(15):153001, Oct 2004. doi:10.1103/PhysRevLett.93.153001.

M. R. Chernick. *Bootstrap Methods: A Guide for Practitioners and Researchers*. Wiley Series in Probability and Statistics. Wiley, 2011. ISBN 9781118211595.

F. Cinti, P. Jain, M. Boninsegni, A. Micheli, P. Zoller, and G. Pupillo. Supersolid droplet crystal in a dipole-blockaded gas. *Phys. Rev. Lett.*, 105:135301, Sep 2010. doi:10.1103/PhysRevLett.105.135301.

J. I. Cirac and P. Zoller. Quantum computations with cold trapped ions. *Phys. Rev. Lett.*, 74: 4091–4094, May 1995. doi:10.1103/PhysRevLett.74.4091.

C. Cohen-Tannoudji, J. Dupont-Roc, and G. Grynberg. *Atom-photon interactions: basic processes and applications*. Wiley-Interscience publication. J. Wiley, 1992. ISBN 9780471293361.

Daniel Comparat and Pierre Pillet. Dipole blockade in a cold Rydberg atomic sample [invited]. *J. Opt. Soc. Am. B*, 27(6):A208–A232, Jun 2010. doi:10.1364/JOSAB.27.00A208.

C. Comte and P. Nozières. Exciton Bose condensation : the ground state of an electron-hole gas - I. Mean field description of a simplified model. *J. Phys. France*, 43(7):1069–1081, 1982. doi:10.1051/jphys:019820043070106900.

David S. Corti and Pablo G. Debenedetti. Statistical mechanics of fluids under internal constraints: Rigorous results for the one-dimensional hard rod fluid. *Phys. Rev. E*, 57:4211–4226, Apr 1998. doi:10.1103/PhysRevE.57.4211.

Ph. Courteille, R. S. Freeland, D. J. Heinzen, F. A. van Abeelen, and B. J. Verhaar. Observation of a Feshbach Resonance in Cold Atom Scattering. *Phys. Rev. Lett.*, 81:69–72, Jul 1998. doi:10.1103/PhysRevLett.81.69.

T. Cubel Liebisch, A. Reinhard, P. R. Berman, and G. Raithel. Atom Counting Statistics in Ensembles of Interacting Rydberg Atoms. *Phys. Rev. Lett.*, 95(25):253002, Dec 2005. doi:10.1103/PhysRevLett.95.253002.

T. Cubel Cubel Liebisch, A. Reinhard, P. R. Berman, and G. Raithel. Erratum: Atom Counting Statistics in Ensembles of Interacting Rydberg Atoms [Phys. Rev. Lett. 95, 253002 (2005)]. *Phys. Rev. Lett.*, 98:109903, Mar 2007. doi:10.1103/PhysRevLett.98.109903.

K. B. Davis, M.-O. Mewes, M. R. Andrews, N. J. van Druten, D. S. Durfee, D. M. Kurn, and W. Ketterle. Bose-Einstein condensation in a gas of sodium atoms. *Physical Review Letters*, 75: 3969–3973, November 1995. doi:10.1103/PhysRevLett.75.3969.

J. Deiglmayr, M. Reetz-Lamour, T. Amthor, S. Westermann, A. L. de Oliveira, and M. Weidemüller. Coherent excitation of Rydberg atoms in an ultracold gas. *Optics Communications*, 264(2):293–298, 2006. ISSN 0030-4018. doi:http://dx.doi.org/10.1016/j.optcom.2006.02.058.

N. B. Delone and V. P. Goreslavsky, S. P.and Krainov. Dipole matrix elements in the quasi-classical approximation. *Journal of Physics B: Atomic, Molecular and Optical Physics*, 27(19):4403, 1994.

N. B. Delone and V. P. Krainov. *Multiphoton Processes in Atoms*. Springer Series on Atomic, Optical, and Plasma Physics. Springer London, Limited, 2012. ISBN 9783642975110.

W. Demtröder. *Experimentalphysik 3: Atome, Moleküle und Festkörper*. Experimentalphysik / Wolfgang Demtröder. Springer, 2005. ISBN 9783540214731.

Y. O. Dudin and A. Kuzmich. Strongly Interacting Rydberg Excitations of a Cold Atomic Gas. *Science*, 336(6083):887–889, 2012. doi:10.1126/science.1217901.

Y. O. Dudin, L. Li, F. Bariani, and A. Kuzmich. Observation of coherent many-body Rabi oscillations. *Nat. Phys.*, 8(11):790–794, November 2012. ISSN 1745-2473.

A. Einstein. Quantentheorie des einatomigen idealen Gases. *Sitzungsberichte der Preußischen Akademie der Wissenschaften*, Physikalisch-mathematische Klasse:261–267, 1924.

A. Einstein. Quantentheorie des einatomigen idealen Gases: Zweite Abhandlung. *Sitzungsberichte der Preußischen Akademie der Wissenschaften*, Physikalisch-mathematische Klasse(3):3–10, 1925.

Richard P. Feynman. Simulating physics with computers. *International Journal of Theoretical Physics*, 21(6-7):467–488, 1982. ISSN 0020-7748. doi:10.1007/BF02650179.

A. V. Filinov, M. Bonitz, and Yu. E. Lozovik. Wigner Crystallization in Mesoscopic 2D Electron Systems. *Phys. Rev. Lett.*, 86:3851–3854, Apr 2001. doi:10.1103/PhysRevLett.86.3851.

A. Fioretti, D. Comparat, C. Drag, T. F. Gallagher, and P. Pillet. Long-range forces between cold atoms. *Phys. Rev. Lett.*, 82:1839–1842, Mar 1999. doi:10.1103/PhysRevLett.82.1839.

Michael E. Fisher. Renormalization group theory: Its basis and formulation in statistical physics. *Rev. Mod. Phys.*, 70:653–681, Apr 1998. doi:10.1103/RevModPhys.70.653.

T. Fließbach. *Statistische Physik: Lehrbuch Zur Theoretischen Physik IV*. Spektrum Akademischer Verlag GmbH, 2010. ISBN 9783827425287.

Th. Förster. Zwischenmolekulare Energiewanderung und Fluoreszenz. *Annalen der Physik*, 437 (1-2):55–75, 1948. ISSN 1521-3889. doi:10.1002/andp.19484370105.

J. S. Frasier, V. Celli, and T. Blum. Resonant processes in a frozen gas. *Phys. Rev. A*, 59:4358–4367, Jun 1999. doi:10.1103/PhysRevA.59.4358.

Roland Freund, Gene H. Golub, and Noel M. Nachtigal. Iterative Solution of Linear Systems. *Acta Numerica*, 1:57–100, 1992.

H. L. Frisch and J. L. Lebowitz. *The Equilibrium Theory of Classical Fluids: A Lecture Note and Reprint Volume*. Frontiers in Physics: Lecture note and reprint series, A. W.A. Benjamin, 1964.

A. Gaëtan, Y. Miroshnychenko, T. Wilk, A. Chotia, M. Viteau, D. Comparat, P. Pillet, A. Browaeys,

and P. Grangier. Observation of collective excitation of two individual atoms in the Rydberg blockade regime. *Nat. Phys.*, 5:115–118, 2009.

T. F. Gallagher. *Rydberg Atoms*. Cambridge Monographs on Atomic, Molecular and Chemical Physics. Cambridge University Press, 2005. ISBN 9780521021661.

M. Gärttner, K. P. Heeg, T. Gasenzer, and J. Evers. Optimal self-assembly of Rydberg excitations for quantum gate operations. *ArXiv e-prints*, March 2012a.

Martin Gärttner, Kilian P. Heeg, Thomas Gasenzer, and Jörg Evers. Finite-size effects in strongly interacting Rydberg gases. *Phys. Rev. A*, 86:033422, Sep 2012b. doi:10.1103/PhysRevA.86.033422.

Tatjana Gericke, Peter Wurtz, Daniel Reitz, Tim Langen, and Herwig Ott. High-resolution scanning electron microscopy of an ultracold quantum gas. *Nat. Phys.*, 4(12):949–953, December 2008. ISSN 1745-2473.

G. F. Giuliani and G. Vignale. *Quantum Theory of the Electron Liquid*. Cambridge University Press, Cambridge, 2005. ISBN 0521821126.

N. Goldenfeld. *Lectures on Phase Transistions and the Renormalization Group*. Advanced Book Program. Perseus [Addison-Wesley], Advanced Book Program, 1992. ISBN 9780201554090.

P. I. Good. *Permutation tests: a practical guide to resampling methods for testing hypotheses*. Springer series in statistics. Springer, 2000. ISBN 9780387988986.

Alexey V. Gorshkov, Johannes Otterbach, Michael Fleischhauer, Thomas Pohl, and Mikhail D. Lukin. Photon-Photon Interactions via Rydberg Blockade. *Phys. Rev. Lett.*, 107:133602, Sep 2011. doi:10.1103/PhysRevLett.107.133602.

Markus Greiner, Olaf Mandel, Tilman Esslinger, Theodor W. Hänsch, and Immanuel Bloch. Quantum phase transition from a superfluid to a Mott insulator in a gas of ultracold atoms. *Nature*, 415(6867):39–44, January 2002. ISSN 0028-0836.

G. Günter, M. Robert-de-Saint-Vincent, H. Schempp, C. S. Hofmann, S. Whitlock, and M. Weidemüller. Interaction Enhanced Imaging of Individual Rydberg Atoms in Dense Gases. *Physical Review Letters*, 108(1):013002, January 2012. doi:10.1103/PhysRevLett.108.013002.

P. Hartmann, Z. Donkó, and G. J. Kalman. Structure and phase diagram of strongly-coupled bipolar charged-particle bilayers. *Europhys. Lett.*, 72(3):396, 2005.

Kilian P. Heeg, Martin Gärttner, and Jörg Evers. Hybrid model for Rydberg gases including exact two-body correlations. *Phys. Rev. A*, 86:063421, Dec 2012. doi:10.1103/PhysRevA.86.063421.

Rolf Heidemann. *Rydberg Excitation of Bose-Einstein Condensates: Coherent Collective Dynamics*. PhD thesis, Universität Stuttgart, 2008.

Rolf Heidemann, Ulrich Raitzsch, Vera Bendkowsky, Björn Butscher, Robert Löw, Luis Santos, and Tilman Pfau. Evidence for Coherent Collective Rydberg Excitation in the Strong Blockade Regime. *Phys. Rev. Lett.*, 99:163601, Oct 2007. doi:10.1103/PhysRevLett.99.163601.

J. V. Hernández and F. Robicheaux. Coherence conditions for groups of Rydberg atoms. *Journal of Physics B: Atomic, Molecular and Optical Physics*, 39(23):4883, 2006.

A. A. High, J. R. Leonard, A. T. Hammack, M. M. Fogler, L. V. Butov, A. V. Kavokin, K. L. Campman, and A. C. Gossard. Spontaneous coherence in a cold exciton gas. *Nature*, 483:584, 2012.

C. S. Hofmann, G. Günter, H. Schempp, N. L. M. Müller, A. Faber, H. Busche, M. Robert-de-Saint-Vincent, S. Whitlock, and M. Weidemüller. An experimental approach for investigating many-body phenomena in Rydberg-interacting quantum systems. *ArXiv e-prints*, July 2013a.

C. S. Hofmann, G. Günter, H. Schempp, M. Robert-de Saint-Vincent, M. Gärttner, J. Evers, S. Whitlock, and M. Weidemüller. Sub-Poissonian Statistics of Rydberg-Interacting Dark-State Polaritons. *Phys. Rev. Lett.*, 110:203601, May 2013b. doi:10.1103/PhysRevLett.110.203601.

J. Honer, H. Weimer, T. Pfau, and H. P. Büchler. Collective Many-Body Interaction in Rydberg Dressed Atoms. *Phys. Rev. Lett.*, 105(16):160404, Oct 2010. doi:10.1103/PhysRevLett.105.160404.

H. Ibach and H. Lüth. *Festkorperphysik Einführung In Die Grundlagen*. Springer-Lehrbuch. Springer, 2009. ISBN 9783540857952.

S. Inouye, M. R. Andrews, J. Stenger, H.-J. Miesner, D. M. Stamper-Kurn, and W. Ketterle. Observation of Feshbach resonances in a Bose-Einstein condensate. *Nature*, 392(6672):151–154, March 1998. ISSN 0028-0836.

J. D. Jackson. *Classical electrodynamics*. Wiley, 1975. ISBN 9780471431329.

D. Jaksch, J. I. Cirac, P. Zoller, S. L. Rolston, R. Côté, and M. D. Lukin. Fast Quantum Gates for Neutral Atoms. *Phys. Rev. Lett.*, 85:2208–2211, Sep 2000. doi:10.1103/PhysRevLett.85.2208.

T. A. Johnson, E. Urban, T. Henage, L. Isenhower, D. D. Yavuz, T. G. Walker, and M. Saffman. Rabi Oscillations between Ground and Rydberg States with Dipole-Dipole Atomic Interactions. *Phys. Rev. Lett.*, 100(11):113003, Mar 2008. doi:10.1103/PhysRevLett.100.113003.

L. P. Kadanoff. Scaling laws for ising models near T_c. *Physics*, 2:263, 1966.

L. V. Keldysh and A. N. Kozlov. Possible instability of the semimetallic state toward Coulomb interaction. *Sov. Phys. Solid State*, 6:2219, 1965.

L. V. Keldysh and A. N. Kozlov. Collective properties of excitons in semiconductors. *Zh. Eksperim. i Teor. Fiz. [Sov. Phys. JETP 27, 521 (1968)]*, 54:978–993, 1968.

M. G. Kendall and P. A. P. Moran. *Geometrical probability*. Griffin's statistical monographs & courses. C. Griffin, 1963.

A. N. Kolmogorov. *Grundbegriffe der Wahrscheinlichkeitsrechnung*. J. Springer, 1933.

D. Kulakovskii, Yu. Lozovik, and A. Chaplik. Collective excitations in exciton crystal. *JETP*, 99: 850–855, 2004.

Y. Y. Kuznetsova, A. A. High, and L. V. Butov. Control of excitons by laterally modulated electrode density. *Applied Physics Letters*, 97(20):201106, 2010. doi:10.1063/1.3517444.

Y. Y. Kuznetsova, J. R. Leonard, L. V. Butov, J. Wilkes, E. A. Muljarov, K. L. Campman, and A. C. Gossard. Excitation energy dependence of the exciton inner ring. *Phys. Rev. B*, 85:165452, Apr 2012. doi:10.1103/PhysRevB.85.165452.

B. Laikhtman and R. Rapaport. Exciton correlations in coupled quantum wells and their luminescence blue shift. *Phys. Rev. B*, 80:195313, Nov 2009. doi:10.1103/PhysRevB.80.195313.

Cornelius Lanczos. An iteration method for the solution of the eigenvalue problem of linear differential and integral operators. *Journal of Research of the National Bureau of Standards*, 45:255–282, 1950. ISSN 0160-1741.

R. B. Lehoucq, D. C. Sorensen, and C. Yang. ARPACK users′ guide. Technical report, Computer Based Learning Unit, University of Leeds, 1997.

Robert J. LeRoy. Long-Range Potential Coefficients From RKR Turning Points: C_6 and C_8 for $B(3\sqcap_{Ou+})$-State Cl_2, Br_2, and I_2. *Canadian Journal of Physics*, 52(3):246–256, 1974. doi:10.1139/p74-035.

Igor Lesanovsky. Many-Body Spin Interactions and the Ground State of a Dense Rydberg Lattice Gas. *Phys. Rev. Lett.*, 106:025301, Jan 2011. doi:10.1103/PhysRevLett.106.025301.

Wenhui Li, Paul J. Tanner, and T. F. Gallagher. Dipole-Dipole Excitation and Ionization in an Ultracold Gas of Rydberg Atoms. *Phys. Rev. Lett.*, 94:173001, May 2005. doi:10.1103/PhysRevLett.94.173001.

C. S. Liu, H. G. Luo, and W. C. Wu. Pattern formation of indirect excitons in coupled quantum wells. *Journal of Physics: Condensed Matter*, 18(42):9659, 2006.

C. J. Lorenzen and K. Niemax. Quantum Defects of the $n^2P_{1/2,3/2}$ Levels in ^{39}K I and ^{85}Rb I. *Phys. Scr.*, 27(4):300–305, 1983.

R. Löw, H. Weimer, U. Krohn, R. Heidemann, V. Bendkowsky, B. Butscher, H. P. Büchler, and T. Pfau. Universal scaling in a strongly interacting Rydberg gas. *Phys. Rev. A*, 80:033422, 2009. doi:10.1103/PhysRevA.80.033422.

Y. E. Lozovik and O. L. Berman. Phase transitions in a system of spatially separated electrons and holes. *Zh. Éksp. Teor. Fiz. [JETP 84, 1027 (1997)]*, 111:1879, 1997.

Yu. E. Lozovik and V. I. Yudson. Exciton. *Zh. Éksp. Teor. Fiz. [Sov. Phys. JETP 44, 389 (1976)]*, 71:738, 1976.

M. D. Lukin, M. Fleischhauer, R. Cote, L. M. Duan, D. Jaksch, J. I. Cirac, and P. Zoller. Dipole Blockade and Quantum Information Processing in Mesoscopic Atomic Ensembles. *Phys. Rev. Lett.*, 87(3):037901, Jun 2001. doi:10.1103/PhysRevLett.87.037901.

G. D. Mahan. *Many Particle Physics*. Physics of Solids and Liquids. Springer, 2000. ISBN 9780306463389.

A. Malijevský, J. Kolafa, A. Mulero, C.A. Galán, M.I. Parra, I. Cachadiña, C. Barrio, J.R. Solana, M. López de Haro, S.B. Yuste, A. Santos, P. Tarazona, J.A. Cuesta, Y. Martínez-Ratón, F.L. Román, J.A. White, A. González, Silva C.M., H. Liu, and V. Garzó. *Theory and Simulation of Hard-Sphere Fluids and Related Systems*. Springer Berlin Heidelberg, 2008.

L. Mandel. Sub-Poissonian photon statistics in resonance fluorescence. *Opt. Lett.*, 4(7):205–207, Jul 1979. doi:10.1364/OL.4.000205.

M. Marinescu. Dispersion coefficients for the nP-nP asymptote of homonuclear alkali-metal dimers. *Phys. Rev. A*, 56:4764–4773, Dec 1997. doi:10.1103/PhysRevA.56.4764.

H. J. Metcalf and P. Van Der Straten. *Laser Cooling and Trapping*. Graduate Texts in Contemporary Physics. Springer-Verlag GmbH, 1999. ISBN 9780387987286.

D. Moltchanov. Survey Paper: Distance distributions in random networks. *Ad Hoc Netw.*, 10(6): 1146–1166, August 2012. ISSN 1570-8705. doi:10.1016/j.adhoc.2012.02.005.

I. Mourachko, D. Comparat, F. de Tomasi, A. Fioretti, P. Nosbaum, V. M. Akulin, and P. Pillet. Many-Body Effects in a Frozen Rydberg Gas. *Phys. Rev. Lett.*, 80(2):253–256, Jan 1998. doi:10.1103/PhysRevLett.80.253.

I. Mourachko, Wenhui Li, and T. F. Gallagher. Controlled many-body interactions in a frozen Rydberg gas. *Phys. Rev. A*, 70:031401, Sep 2004. doi:10.1103/PhysRevA.70.031401.

M. Müller, I. Lesanovsky, H. Weimer, H. P. Büchler, and P. Zoller. Mesoscopic Rydberg Gate Based on Electromagnetically Induced Transparency. *Phys. Rev. Lett.*, 102:170502, Apr 2009. doi:10.1103/PhysRevLett.102.170502.

M. A. Nielsen and I. L. Chuang. *Quantum Computation and Quantum Information*. Cambridge Series on Information and the Natural Sciences. Cambridge University Press, 2000. ISBN 9780521635035.

W. Nolting. *Grundkurs Theoretische Physik 6: Statistische Physik*. Grundkurs Theoretische Physik / Wolfgang Nolting. Springer, 2005. ISBN 9783540205050.

B. Olmos, W. Li, S. Hofferberth, and I. Lesanovsky. Amplifying single impurities immersed in a gas of ultracold atoms. *Phys. Rev. A*, 84:041607, Oct 2011. doi:10.1103/PhysRevA.84.041607.

L. S. Ornstein and F. Zernike. Accidental deviations of density and opalescence at the critical point of a single substance. *Proc. Acad. Sci. Amsterdam*, 17:795, 1914.

Th. Östreich and A. Knorr. Various appearances of Rabi oscillations for 2π-pulse excitation in a semiconductor. *Phys. Rev. B*, 48:17811–17817, 1993. doi:10.1103/PhysRevB.48.17811.

C. C. Paige. Computational variants of the Lanczos method for the eigenproblem. *J. Inst. Math. Appl.*, 10:373–381, 1972. ISSN 0020-2932.

D. Petrosyan and M. Fleischhauer. Electromagnetically induced transparency and photon-photon interactions with Rydberg atoms. *Journal of Physics: Conference Series*, 350(1):012001, 2012.

Thibault Peyronel, Ofer Firstenberg, Qi-Yu Liang, Sebastian Hofferberth, Alexey V. Gorshkov, Thomas Pohl, Mikhail D. Lukin, and Vladan Vuletic. Quantum nonlinear optics with single photons enabled by strongly interacting atoms. *Nature*, 488(7409):57–60, August 2012. ISSN 0028-0836.

Max Planck. Über irreversible Strahlungsvorgänge. *Sitzungsberichte der Königlich Preußischen Akademie der Wissenschaften*, 5:440â480, 1899.

T. Pohl, E. Demler, and M. D. Lukin. Dynamical Crystallization in the Dipole Blockade of Ultracold Atoms. *Phys. Rev. Lett.*, 104(4):043002, Jan 2010. doi:10.1103/PhysRevLett.104.043002.

W. Preuss, F. B. Günter Wenisch, and F. Bierbaum. *Lehr- und Übungsbuch numerische Mathematik*. Fachbuchverl. Leipzig im Carl-Hanser-Verlag, 2001. ISBN 9783446213753.

G. Pupillo, A. Micheli, M. Boninsegni, I. Lesanovsky, and P. Zoller. Mesoscopic phases of dipolar ensembles with polar molecules and Rydberg atoms. *ArXiv e-prints*, April 2009.

G. Pupillo, A. Micheli, M. Boninsegni, I. Lesanovsky, and P. Zoller. Strongly Correlated Gases of Rydberg-Dressed Atoms: Quantum and Classical Dynamics. *Phys. Rev. Lett.*, 104(22):223002, Jun 2010. doi:10.1103/PhysRevLett.104.223002.

S. Ranganathan and R. E. Johnson. Diffusion and phase diagram of an electron-hole bilayer: A molecular dynamics study. *Phys. Rev. B*, 75:155314, Apr 2007. doi:10.1103/PhysRevB.75.155314.

A. Reinhard, T. Cubel Liebisch, B. Knuffman, and G. Raithel. Level shifts of rubidium Rydberg states due to binary interactions. *Phys. Rev. A*, 75:032712, Mar 2007. doi:10.1103/PhysRevA.75.032712.

F. Robicheaux and J. V. Hernández. Many-body wave function in a dipole blockade configuration. *Phys. Rev. A*, 72(6):063403, Dec 2005. doi:10.1103/PhysRevA.72.063403.

M. P. Robinson, B. Laburthe Tolra, Michael W. Noel, T. F. Gallagher, and P. Pillet. Spontaneous Evolution of Rydberg Atoms into an Ultracold Plasma. *Phys. Rev. Lett.*, 85:4466–4469, Nov 2000. doi:10.1103/PhysRevLett.85.4466.

M. Saffman, T. G. Walker, and K. Mølmer. Quantum information with Rydberg atoms. *Rev. Mod. Phys.*, 82:2313–2363, Aug 2010. doi:10.1103/RevModPhys.82.2313.

J. J. Sakurai. *Modern Quantum Mechanics*. Pearson Education, 2006. ISBN 9788177585483.

Peter Schausz, Marc Cheneau, Manuel Endres, Takeshi Fukuhara, Sebastian Hild, Ahmed Omran, Thomas Pohl, Christian Gross, Stefan Kuhr, and Immanuel Bloch. Observation of spatially ordered structures in a two-dimensional Rydberg gas. *Nature*, 491(7422):87–91, November 2012. ISSN 0028-0836.

H. Schempp, G. Günter, C. S. Hofmann, C. Giese, S. D. Saliba, B. D. DePaola, T. Amthor, M. Weidemüller, S. Sevinçli, and T. Pohl. Coherent Population Trapping with Controlled Interparticle Interactions. *Phys. Rev. Lett.*, 104:173602, Apr 2010. doi:10.1103/PhysRevLett.104.173602.

H. Schempp, G. Günter, M. Robert-de-Saint-Vincent, C. S. Hofmann, D. Breyel, A. Komnik, D. W.

Schönleber, M. Gärttner, J. Evers, S. Whitlock, and M. Weidemüller. Full counting statistics of laser excited Rydberg aggregates in a one-dimensional geometry. *ArXiv e-prints*, August 2013.

Christoph Schindler and Roland Zimmermann. Analysis of the exciton-exciton interaction in semiconductor quantum wells. *Phys. Rev. B*, 78:045313, Jul 2008. doi:10.1103/PhysRevB.78.045313.

F. Schwabl. *Quantenmechanik (QM I)*. Springer-Lehrbuch. Springer, 2002. ISBN 9783540431060.

A. Schwarzkopf, R. E. Sapiro, and G. Raithel. Imaging Spatial Correlations of Rydberg Excitations in Cold Atom Clouds. *Phys. Rev. Lett.*, 107:103001, Aug 2011. doi:10.1103/PhysRevLett.107.103001.

M. O. Scully and S. Zubairy. *Quantum Optics*. Cambridge University Press, 1997. ISBN 9780521435956.

Eran Sela, Matthias Punk, and Markus Garst. Dislocation-mediated melting of one-dimensional Rydberg crystals. *Phys. Rev. B*, 84:085434, Aug 2011. doi:10.1103/PhysRevB.84.085434.

S. Sevinçli, N. Henkel, C. Ates, and T. Pohl. Nonlocal Nonlinear Optics in Cold Rydberg Gases. *Physical Review Letters*, 107(15):153001, October 2011. doi:10.1103/PhysRevLett.107.153001.

P. W. Shor. Polynomial-Time Algorithms for Prime Factorization and Discrete Logarithms on a Quantum Computer. *SIAM Review*, 41:303–332, January 1999. doi:10.1137/S0036144598347011.

Kilian Singer, Markus Reetz-Lamour, Thomas Amthor, Luis Gustavo Marcassa, and Matthias Weidemüller. Suppression of Excitation and Spectral Broadening Induced by Interactions in a Cold Gas of Rydberg Atoms. *Phys. Rev. Lett.*, 93:163001, Oct 2004. doi:10.1103/PhysRevLett.93.163001.

Kilian Singer, Markus Reetz-Lamour, Thomas Amthor, Simon Fölling, Michaela Tscherneck, and Matthias Weidemüller. Spectroscopy of an ultracold Rydberg gas and signatures of Rydberg-Rydberg interactions. *Journal of Physics B: Atomic, Molecular and Optical Physics*, 38(2):S321, 2005a.

Kilian Singer, Jovica Stanojevic, Matthias Weidemüller, and Robin Côté. Long-range interactions between alkali Rydberg atom pairs correlated to the $ns - ns, np - np$ and $nd - nd$ asymptotes. *Journal of Physics B: Atomic, Molecular and Optical Physics*, 38(2):S295, 2005b.

D. Snoke, S. Denev, Y. Liu, L. Pfeiffer, and K. West. Long-range transport in excitonic dark states in coupled quantum wells. *Nature*, 418(6899):754–757, August 2002. ISSN 0028-0836.

H. Soller and D. Breyel. Signatures in the conductance for phase transitions in excitonic systems. *ArXiv e-prints*, August 2013.

B. Sun and F. Robicheaux. Numerical study of two-body correlation in a 1D lattice with perfect blockade. *New Journal of Physics*, 10(4):045032, 2008.

D. Tong, S. M. Farooqi, J. Stanojevic, S. Krishnan, Y. P. Zhang, R. Côté, E. E. Eyler, and P. L. Gould. Local Blockade of Rydberg Excitation in an Ultracold Gas. *Phys. Rev. Lett.*, 93(6):063001, Aug 2004. doi:10.1103/PhysRevLett.93.063001.

S. Torquato. *Random Heterogeneous Materials: Microstructure and Macroscopic Properties*. Interdisciplinary Applied Mathematics. Springer, 2002. ISBN 9780387951676.

E. Urban, T. A. Johnson, T. Henage, L. Isenhower, D. D. Yavuz, T. G. Walker, and M. Saffman. Observation of Rydberg blockade between two atoms. *Nature Physics*, 5:110 – 114, 2009. doi:10.1038/nphys1178.

R. M. W. van Bijnen, S. Smit, K. A. H. van Leeuwen, E. J. D. Vredenbregt, and S. J. J. M. F. Kokkelmans. Adiabatic formation of Rydberg crystals with chirped laser pulses. *Journal of Physics B: Atomic, Molecular and Optical Physics*, 44(18):184008, 2011.

Matthieu Viteau, Paul Huillery, Mark G. Bason, Nicola Malossi, Donatella Ciampini, Oliver Morsch, Ennio Arimondo, Daniel Comparat, and Pierre Pillet. Cooperative Excitation and Many-Body Interactions in a Cold Rydberg Gas. *Phys. Rev. Lett.*, 109:053002, Jul 2012. doi:10.1103/PhysRevLett.109.053002.

Matthias Vojta. Quantum phase transitions. *Reports on Progress in Physics*, 66(12):2069, 2003.

Thomas Vojta. Quantum phase transitions in electronic systems. *Annalen der Physik*, 9(6):403–440, 2000. ISSN 1521-3889. doi:10.1002/1521-3889(200006)9:6<403::AID-ANDP403>3.0.CO;2-R.

Z. Vörös, R. Balili, D. W. Snoke, L. Pfeiffer, and K. West. Long-Distance Diffusion of Excitons in Double Quantum Well Structures. *Phys. Rev. Lett.*, 94:226401, 2005. doi:10.1103/PhysRevLett.94.226401.

D. F. Walls and G. J. Milburn. *Quantum Optics*. SpringerLink: Springer e-Books. Springer, 2008. ISBN 9783540285731.

A. Walz-Flannigan, J. R. Guest, J.-H. Choi, and G. Raithel. Cold-Rydberg-gas dynamics. *Phys. Rev. A*, 69:063405, Jun 2004. doi:10.1103/PhysRevA.69.063405.

Matthias Weidemüller. Rydberg atoms: There can be only one. *Nature Physics*, 5:91–92, 2009. doi:10.1038/nphys1193.

H. Weimer. *Quantum many-body physics with strongly interacting Rydberg atoms*. PhD thesis, Universität Stuttgart, 2010.

H. Weimer, R. Löw, T. Pfau, and H. P. Büchler. Quantum Critical Behavior in Strongly Interacting Rydberg Gases. *Phys. Rev. Lett.*, 101(25):250601, Dec 2008. doi:10.1103/PhysRevLett.101.250601.

Christof Weitenberg, Manuel Endres, Jacob F. Sherson, Marc Cheneau, Peter Schausz, Takeshi Fukuhara, Immanuel Bloch, and Stefan Kuhr. Single-spin addressing in an atomic Mott insulator. *Nature*, 471(7338):319–324, March 2011. ISSN 0028-0836.

B. Widom. Surface Tension and Molecular Correlations near the Critical Point. *J. Chem. Phys.*, 43:3892, 1965.

E. Wigner. On the Interaction of Electrons in Metals. *Phys. Rev.*, 46:1002–1011, Dec 1934. doi:10.1103/PhysRev.46.1002.

Kenneth G. Wilson. Renormalization Group and Critical Phenomena. I. Renormalization Group and the Kadanoff Scaling Picture. *Phys. Rev. B*, 4:3174–3183, Nov 1971a. doi:10.1103/PhysRevB.4.3174.

Kenneth G. Wilson. Renormalization Group and Critical Phenomena. II. Phase-Space Cell Analysis of Critical Behavior. *Phys. Rev. B*, 4:3184–3205, Nov 1971b. doi:10.1103/PhysRevB.4.3184.

Joseph Ladislas Wiza. Microchannel plate detectors. *Nuclear Instruments and Methods*, 162(1-3): 587–601, 1979. ISSN 0029-554X. doi:10.1016/0029-554X(79)90734-1.

W. A. Woyczyński. *A First Course in Statistics for Signal Analysis*. SpringerLink : Bücher. Springer, 2010. ISBN 9780817681012.

S. Wüster, J. Stanojevic, C. Ates, T. Pohl, P. Deuar, J. F. Corney, and J. M. Rost. Correlations of Rydberg excitations in an ultracold gas after an echo sequence. *Phys. Rev. A*, 81(2):023406, Feb 2010. doi:10.1103/PhysRevA.81.023406.

Wolfgang Zeller, Michael Mayle, Thorsten Bonato, Gerhard Reinelt, and Peter Schmelcher. Spectra and ground states of one- and two-dimensional laser-driven lattices of ultracold Rydberg atoms. *Phys. Rev. A*, 85:063603, Jun 2012. doi:10.1103/PhysRevA.85.063603.

F. Zernike and J. A. Prins. Die Beugung von Röntgenstrahlen in Flüssigkeiten als Effekt der Molekülanordnung. *Zeitschrift für Physik*, 41(6-7):184–194, 1927. ISSN 0044-3328. doi:10.1007/BF01391926.

X. T. Zou and L. Mandel. Photon-antibunching and sub-Poissonian photon statistics. *Phys. Rev. A*, 41:475–476, Jan 1990. doi:10.1103/PhysRevA.41.475.

Acknowledgement

With this manuscript I not only present the results of my work in the last three years but also I complete a phase of my life. After having moved to Heidelberg more than eight years ago and studying physics since I now face an ocean full of opportunities which I should be well-prepared for by now. As any major task in life this work could not have been accomplished by one person alone. Here I would like to thank everybody who accompanied me in the last couple of years.

First of all I have to thank Andreas Komnik who supervised me on both my diploma thesis as well as this work. Not only did he share his knowledge about physics but he also always encouraged me in my ideas. In a seemingly uncountable number of discussions he motivated and challenged me with new projects. Also I am much obliged to my doctoral examination committee which included Andrey Surzhykov, Werner Aeschbach-Hertig and Rüdiger Klingeler.

Certainly I have to thank my family who always were very supportive. Besides providing me with financial rear cover they were very understanding in the fact that I did not travel home a lot of times for the sake of my work and gave a lot of moral support when needed. Also I would like to thank Bine who was always there for the last couple of month and has become a very important part of my life. She never fails to bring a smile on my face and supported me with her endless source of energy.

A special thanks also is devoted to Frithjof Düsel whom I know for all my life. We had great times when he visited me Heidelberg or I visited him. I have to mention that I also see him as a kind of role model who always pursued his dreams and always makes the best out of any opportunity.

A great support was also given by my friends and colleagues in the Philosophenweg 19. They are Frank Hantschel, whom I shared a room with, and Kambis Veschgini, who did a great job increasing both quality and difficulty of my problems, and always were there for a good laugh. With Henning Soller I not only worked on the exciton bilayer systems but also went to numerous conferences where we had good times and together with Stefan Maier and Karsten Joho helped each other with anything that that arises in a discussion about physics. All of the above together with Giulio Schober and Kay Giering joined for lunch, which was usually quite informative both on news on physics as well as any other current event.

Also I thank Shannon Whitlock, Georg Günter, Hanna Schempp, Martin Robert-de-Saint-Vincent, Christoph Hofmann, and Matthias Weidemüller with whom I collaborated on the topic of exper-

imental data analysis. Our almost weekly discussion brought up new ideas and helped me get a deeper insight into the experimental point of view of the Rydberg physics. In addition they supplied me with the data used in the main text.

Last but not least I have to thank my Friday “Mensa-club” which included Adrian Vollmer, Oliver Matula, Svea Proft, Alexander Kononov, Thomas Pfeil, Thomas Gerner, Kolja Szillat and Alexandra Kampkötter. The topics we discussed here included basically anything one might think of and kept a good balance between physics and everything else.